INFORMATION TO USERS

This manuscript has been reproduced from the microfilm master. UMI films the text directly from the original or copy submitted. Thus, some thesis and dissertation copies are in typewriter face, while others may be from any type of computer printer.

The quality of this reproduction is dependent upon the quality of the copy submitted. Broken or indistinct print, colored or poor quality illustrations and photographs, print bleedthrough, substandard margins, and improper alignment can adversely affect reproduction.

In the unlikely event that the author did not send UMI a complete manuscript and there are missing pages, these will be noted. Also, if unauthorized copyright material had to be removed, a note will indicate the deletion.

Oversize materials (e.g., maps, drawings, charts) are reproduced by sectioning the original, beginning at the upper left-hand corner and continuing from left to right in equal sections with small overlaps.

Photographs included in the original manuscript have been reproduced xerographically in this copy. Higher quality 6" x 9" black and white photographic prints are available for any photographs or illustrations appearing in this copy for an additional charge. Contact UMI directly to order.

ProQuest Information and Learning
300 North Zeeb Road, Ann Arbor, MI 48106-1346 USA
800-521-0600

Université d'Ottawa • University of Ottawa

Modeling and Design of a Traveling Wave Photodetector on InP for Use at 1550nm

by

Luan Nguyen, B.A.Sc.

A thesis submitted to the
School of Graduated Studies and Research
in partial fulfillment of the requirements for the degree of

Master of Applied Science
in Electrical Engineering

Ottawa-Carleton Institute of Electrical and Computer Engineering
School of Information Technology and Engineering
Faculty of Engineering
University of Ottawa

January 2001

Abstract

The last ten years have seen an explosion in the demand for bandwidth as a result of the convergence of radio, television, voice, video and data over a single optical network. As a result of this sensational appetite for bandwidth, current optoelectronic components are being pressed to their limit. Thus researchers and design engineers alike must conduct core research into novel optoelectronic architectures. A photodetector is an optical to electrical transducer that is present in all modern non-coherent optical networks. Current conventional vertically illuminated detectors used in these networks have a bandwidth-efficiency trade off. That is, it is not possible to simultaneously achieve high bandwidth and high efficiency.

The traveling wave photodetector is one architecture that has shown promise in being able to achieve both high bandwidth and efficiency. The optical signal that generates the microwave photocurrent is perpendicular to the collection field, thus two waves will co-propagate down this device in their respective guides. In a classical traveling wave device it is the interaction of these two waves that dictates the response of the device; in a traveling wave photodetector this is not the case.

The main purpose of this work is to design a high speed, high efficiency traveling wave photodetector at 1550 nm. The design begins with the choice of diode architecture followed by the material choice. Once these two parameters have been chosen the traveling wave design is broken down into three sub-designs, the semiconductor design, the optical design and the microwave design. The semiconductor design is done on an InGaAs/InGaAsP/InP material system design, with the absorbing layer optimized for detection around 1550 nm optical wavelength.

The optical waveguide design for the traveling wave photodetector was done using the Method of Lines (MoL). This numerical method was chosen to analyze the optical waveguide because of its unique ability to accurately characterize the metal and generate all six field components. A MoL formulation was derived for non-anisotropic lossy inhomogeneous material, the results of which were coded in Matlab. To ensure

that the derivation and program were formulated and coded correctly several structures were analyzed and compared against results published in the scientific literature.

The microwave design was accomplished using a commercially available CAD package based on the Method of moments. The optical design and theory suggest that velocity matching is secondary in determining the frequency response of these detectors. Thus using a commercial simulator two designs were undertaken, one in which the device was optimized for velocity matching while the other was not. In doing this the hope was to generate empirical results that would confirm or deny the effects of velocity matching on device bandwidth.

The devices were fabricated and DC, optical and microwave measurements performed. A very high responsivity was obtained for both designs for electrically short devices. However, it was not possible to definitely determine the frequency response of the device as a result of the probe footprint. Thus a conclusion based on the effects of velocity matching was not possible, hence a recommendation to redesign the mask and re-measure the designs presented here is made.

Acknowledgements

Over the years the list of acknowledgements has grown significantly. I am deeply grateful for this opportunity to express my gratitude publicly to the large number of individuals who have assisted me during my Master's studies at the University of Ottawa.

First and foremost I wish to thank Dr. Pierre Berini for his guidance, knowledge and support throughout the years. Special thanks goes out to Dr. Ezio Berolo for sharing his 30 years of expertise in the areas of device physics and fabrication with me. Other professional thanks goes out to Dr. Hamid Khazaei for our many discussions on traveling wave devices. Dr. Andreas Stöhr for confirming my original findings. Robert James, Heng Hua, Ewa Lisicka-Shrzek and Shaochun Cao at the Communications Research Center for their invaluable assistance in the design, fabrication and measurements of these devices.

Many thanks to Dr. Dave Roscoe for allowing me to continue my studies while pursuing full time employment.

Kudos goes out to my colleagues Shilpa Vidyarthi, Sue Kolloru, Truong Nguyen, Ramsey Hage, Billy Lee as well as Phil, Julie and Daryl Lafleur for their good humor, support and encouragement along the way.

Finally I wish to thank my family who have supported and loved me throughout it all.

Dedicated to my mother Hoang Thi Cuong (Rosemary),

my brother Lampson Nguyen

and my sister Janet Nguyen.

"Far better to dare mighty things,

to win glorious triumphs, even though checkered by failure,

than to take rank with those poor spirits who neither enjoy much nor suffer much,

because they live in the gray twilight that knows not victory nor defeat"

Former U.S President Theodore Roosevelt.

For years, I have dwelled in the hours between the dusk and the dawn.

You will find me there when the noise of the world is hushed,

You will find me there when the birds have risen and the sun has not,

You will find me there when God speaks his silent volumes,

I will be there...

Walking...pondering...wondering...listening.

For years, I have dwelled in the clouds of light,

For their quarky nature has defined my soul and shaped my heart.

It is only now that I realize as I approach the end of one question and the beginning of the next,

that no question, no matter how simply defined can truly and completely be answered.

I only seek to find some level of truth, and accept that I can go on no further.

I guess, I'm the lucky one as I am allowed to spend my life pondering such questions.

Luan Nguyen

Table of Contents

Chapter 1.0 Introduction....1

1.1 Background....1

1.2 Thesis Objective and Motivation....3

1.3 Thesis Contribution....5

1.4 Thesis Organization....5

Chapter 2.0 Photodetectors....8

2.1 Introduction to Optical Materials and Optical Detection....8

2.2 p-i-n Photodetectors....12

2.3 Avalanche Photodetectors....13

2.4 Schottky Barrier Diodes....15

2.5 Summary of Photodiode Architectures....17

2.6 Factors Affecting the Bandwidth-Efficiency Product of VPDs....18

2.7 Optimizing the Frequency Response of Detectors....22

2.8 Waveguide Photodetectors (WGPDs)....23

2.9 Traveling Wave Photodetectors (TWPDs)....24

2.10 Theory of Traveling Wave Detectors....26

2.11 Photodetector Electrical Waveguide....27

2.12 Electrical Waveguide: Waveguide Model....29

2.13 Electrical Waveguide: Equivalent Circuit Model....32

2.14 Electrical Waveguide: Velocity Mismatch Bandwidth Model....37

2.15 Velocity Mismatch Bandwidth Limitation....42

Chapter 3.0 Numerical Analysis Using the Method of Lines (MoL)....48

3.1 Introduction to the Method of Lines....48

3.1.1 Heuristic Description of the Method of Lines....49

3.1.2 Method of Lines Analysis Algorithm....51

3.2 Formulation for Isotropic Inhomogeneous Lossy Structures....53
3.2.1 Formulation of Uncoupled Wave Equations....53
3.2.2 Expressions for Field Components....55
3.2.3 Discretization of the Computational Domain....56
3.2.4 Replacing Differential Operators with Finite Difference Operators....59
3.2.5 Applying the Transformation Matrices....63
3.2.6 Analytical Solution to Telegrapher's Equation....65
3.2.7 Formulation of Impedance and Admittance Relationships....66
3.2.8 Formulation of the Modal Matrix $G_{e,h}(\gamma)$....71
3.2.9 Indirect Eigenvalue Problem....73
3.2.10 Generating Field Distributions....75
3.3 Validation of the Method of Lines....78
3.3.1 Validation of MoL for Lossless Structures....78
3.3.2 Validation of MoL for Lossy Structure....88
Chapter 4.0 Design and Simulation....91
4.1 Photodiode Architecture....91
4.2 Semiconductor Layer Parameters....92
4.2.1 Heterostructure Material Choice....92
4.2.2 Increasing Efficiency via Bandgap Engineering....94
4.2.3 Optimizing Layer Designs....95
4.2.4 Tradeoffs and Design Limitations....100
4.3 Optical Modeling and Design....103
4.3.1 Modeling of Semiconductor Losses....104
4.3.2 Modeling of the Electrode....105
4.3.3 Poynting Vector and Confinement Factor....106
4.3.3.1 Poynting Vector....106
4.3.3.2 Confinement Factor....107
4.3.4 Equivalent Slab Structures and Initial Guess....108

4.3.5 Field Distributions Using the Poynting Vector....109
4.3.6 Optical Rib Waveguide for TWPD....111
4.3.7 Higher Order Modes....120
4.4 TWPD: Microwave Modeling and Design....121
4.4.1 Semiconductor Simplifications to Microwave Design....122
4.4.2 Microwave Waveguide Design....123
4.5 Mask Design and Layout....131
Chapter 5.0 Measurements and Analysis....136
5.1 DC Measurements....137
5.1.1 Responsivity....137
5.1.2 Linearity and Saturation Current....140
5.1.3 Ideality Factor and Extrapolated Leakage Current....140
5.1.4 Threshold Voltage and Breakdown Voltage....142
5.1.5 Leakage Current....142
5.2 Optical Measurements....144
5.2.1 Polarization Dependency....144
5.2.2 Electroluminescence....146
5.3 Microwave Measurement....148
5.3.1 S-Parameters....149
5.3.2 Microwave Bandwidth....151
Chapter 6 Conclusion and Future Work....158
6.1 Summary....158
6.2 Future Work and Improvements....164
6.2.1 Future Work and Improvements Involving the MoL....164
6.2.2 Future Work and Improvements Involving the TWPD....167
References....171

List of Figures

Figure 2.1 Optical absorption for a direct bandgap semiconductor....9

Figure 2.2 Equivalent circuit for a photodiode in photovoltaic and photoconductive mode....10

Figure 2.3 p-i-n photodetector....12

Figure 2.4 The process of avalanche multiplication....14

Figure 2.5 Schottky diode band profile....15

Figure 2.6 Equivalent circuit for a photodetector....19

Figure 2.7 Conceptual view of a vertically illuminated photodetector....21

Figure 2.8 p-i-n waveguide photodetector....23

Figure 2.9 Equivalent circuit for a WGPD....24

Figure 2.10 Equivalent circuit for a traveling wave photodetector (TWPD)....25

Figure 2.11 p-i-n traveling wave photodetector....28

Figure 2.12 Cross section view of TWPD and the charge distribution....29

Figure 2.13 Half the TWPD cut about the plane of symmetry....30

Figure 2.14 Equivalent transmission line circuit for TWPD....33

Figure 2.15 Equivalent circuit for TWPD in the midband frequency range....35

Figure 2.16 Conceptual view of photodetection process....39

Figure 2.17 Velocity mismatched frequency response....44

Figure 2.18 Normalized microwave bandwidth vs. velocity mismatch ratio....45

Figure 3.1 Numerical method classification....49

Figure 3.2 Arbitrary waveguide structure....53

Figure 3.3 Line discretization for electrical wall electric wall boundary conditions....58

Figure 3.4 Multi-layer structure having arbitrary top and bottom boundary conditions....65

Figure 3.5 First lossless optical rib waveguide....79

Figure 3.6 Effective index η_{eff} vs. number of lines....80

Figure 3.7a E_x Field distribution for first lossless rib structure in E_x^{11} mode....83

Figure 3.7b E_y Field distribution for first lossless rib structure in E_x^{11} mode....83

Figure 3.7c E_z Field distribution for first lossless rib structure in E_x^{11} mode....84

Figure 3.7d H_x Field distribution for first lossless rib structure in E_x^{11} mode....84

Figure 3.7e H_y Field distribution for first lossless rib structure in E_x^{11} mode....85

Figure 3.7f H_z Field distribution for first lossless rib structure in E_x^{11} mode....85

Figure 3.8 Second lossless optical rib structure....86

Figure 3.9 n_{eff} vs. $k_o t_f$ for second lossless rib structure....87

Figure 3.10 Schottky contact TWPD....88

Figure 4.1 Lattice constants and bandgap of semiconductor materials....93

Figure 4.2 Structure A....97

Figure 4.3 Bandgap profile for structure A....97

Figure 4.4 Structure B....99

Figure 4.5 Bandgap profile for structure B....100

Figure 4.6 Interaction of wave function in structure B....101

Figure 4.7 TE_o slab mode profile for structure A....110

Figure 4.8 TE_o slab mode profile for structure B....110

Figure 4.9 Definition of computational domain....112

Figure 4.10a Power density distribution for structure A with electrode in E_x^{11} mode....113

Figure 4.10b Power density distribution for structure A with no electrode in E_x^{11} mode....113

Figure 4.10c Power density distribution for structure A with electrode in E_y^{11} mode....114

Figure 4.10d Power density distribution for structure A with no electrode in E_y^{11} mode....114

Figure 4.10e Power density distribution for structure B with electrode in E_x^{11} mode....115

Figure 4.10f Power density distribution for structure B with no electrode in E_x^{11} mode....115

Figure 4.10g Power density distribution for structure B with electrode in E_y^{11} mode....116

Figure 4.10h Power density distribution for structure B with no electrode in E_y^{11} mode....116

Figure 4.11 Optical absorption vs. device length....119

Figure 4.12 E_x^{21} mode for structure B with electrode present....120

Figure 4.13 CPW electric fields....125

Figure 4.14 TWPD electric fields....126

Figure 4.15 Microstrip electric fields....127
Figure 4.16 Characteristic impedance vs. frequency for structure A and B....127
Figure 4.17 Microwave effective index vs. frequency....128
Figure 4.18 Microwave loss vs. frequency for structure A and B....129
Figure 4.19 Microwave bandwidth vs. microwave effective index for structure A....130
Figure 4.20 Microwave bandwidth vs. microwave effective index for structure B....130
Figure 4.21 Examples of fabrication issues....132
Figure 4.22 Layout of mask design....134
Figure 4.23 Fabricated wafer and array of TWPD....135
Figure 5.1 Responsivity measurement setup....137
Figure 5.2 Photocurrent vs. optical input power for structure A....138
Figure 5.3 Photocurrent vs. optical input power for structure B....139
Figure 5.4 Ideality factor measurement setup....140
Figure 5.5 I-V curves for structure A and B....141
Figure 5.6 Polarization measurement setup....145
Figure 5.7 Electroluminescence measurement setup....147
Figure 5.8 Electroluminescence spectra....148
Figure 5.9 Measured S_{11} for structure A and B....150
Figure 5.10 Measured S_{21} for structure A and B....150
Figure 5.11 Microwave bandwidth measurement setup....152
Figure 5.12 Frequency response for structure A....153
Figure 5.13 Frequency response for structure B....154
Figure 5.14 Probe footprint....155
Figure 5.15 Equivalent circuit for TWPD including probe footprint....156
Figure 6.1 Procedure for determining root....165
Figure 6.2 Microwave bandwidth vs. effective index using transit time limitation....168

List of Tables

Table 2.1 Photodiode architecture and characteristics....17

Table 3.1 Modal matrix formulations....74

Table 3.2 n_{eff} for different line discretizations....79

Table 3.3 Richardson's extrapolation values for n_{eff}....81

Table 3.4 Computed n_{eff} compared with results in literature....81

Table 3.5 Computed propagation constant for Schottky contact TWPD....89

Table 4.1 Layer parameters for structure A....96

Table 4.2 Layer parameters for structure B....98

Table 4.3 Propagation constants for equivalent slab guide....109

Table 4.4 Propagation constants for structure A....117

Table 4.5 Propagation constants for structure B....117

Table 4.6 Microwave values....124

Table 5.1 Leakage current vs. device length....143

Table 5.2 Dark current at different bias voltages for structure A and B....144

Table 5.3 Polarization measurement results....146

Table 5.4 Calculation of RC bandwidth for probe footprint....157

List of Acronyms

APD	avalanche photodiodes
a.u	arbitrary unit
CAD	computer aided design
c_f	confinement factor
CPW	coplanar waveguide
DFB	distributed feedback
EDFA	erbium doped fiber amplifier
e-h	electron-hole
ew	electric wall
FDM	finite difference method
FEM	finite element method
MIS	metal insulator semiconductor
MoL	method of lines
MoM	method of moments
MQW	multiple quantum wells
MTBF	mean time between failures
mw	magnetic wall
NiD	non-intentionally doped
ODE	ordinary differential equation
PDE	partial differential equation
PSTN	public switched telephone network
QW	quantum well
RIE	reactive ion etch
SI	semi-insulating
TE	transverse electric
TEM	transverse electromagnetic
TM	transverse magnetic
TWPD	traveling wave photodetector
VPD	vertically illuminated detector
WGPD	waveguide photodetectors
WLAN	wireless area network

Chapter 1 Introduction

This chapter will begin with a historical overview of the developments in the optic industry over the last 30 years. Following this historical overview the chapter will then proceed with a presentation of the objectives and motivations driving this thesis, moving onto the contribution associated with the work. Chapter 1 will end with an outline of what will be presented in other chapters in this thesis.

1.1 Background

The sensational demand for more bandwidth in recent years and the convergence of television, radio, video, voice and data over a single network has led to the proliferation of optical communication networks across North American as well as around the world. Conventional networks such as the phone (PSTN), cable and various wireless area networks (WLAN) cannot meet the bandwidth requirements needed for this convergence. Fiber optic communication systems are light wave systems that employ optical fibers for the transmission of information. Presently, only with fiber optics and its inherently large bandwidth can a single high speed data network covering North America and connecting the world be realized.

Optical communication components have historically been designed in one of three optical wavelength transmission windows:

- 800-900 nm transmission window
- 1210–1310 nm transmission window
- 1550–1600 nm transmission window

These transmission windows have come about as a result of technology, as well as the desire to work where a signal experiences minimum fiber attenuation and dispersion. The first window occurs at 800 nm

to 900 nm. Here the optical signal experiences a loss of approximately 2.0-2.5 dB/km. Systems were deployed in this windows in and around 1978 and operated at bit rates of 50 to 100 Mbps[1].

This was immediately followed by single mode systems operating at 1300 nm. It was favorable to operate around this wavelength due to the low loss, 0.50 dB/km, and the minimal dispersion characteristic of the fiber at this wavelength. These second-generation systems reached their peak of maturity around 1987 and achieved a bit rate of approximately 1.7 Gbps with a repeater spacer of 50 km [2].

The third transmission window occurring at 1550 nm has an interesting history. Although attenuation of 0.20 dB/km has been known and demonstrated in the laboratory since the late 1970s[3], the optics industry generally shied away from this wavelength because the fiber had a large dispersion characteristic at 1550 nm. The push to operate at this wavelength came not from the advantage of lower signal attenuation, but as a result of optical amplifiers. Prior to the development of optical amplifiers, electronic repeaters were used to amplify the information. That is, the optical signal would be demodulated, the information amplified vis-a-vis conventional electronic amplifiers, and then the information re-modulated. With the development of erbium-doped fiber amplifiers (EDFAs) this conversion back to the electrical domain was eliminated.

The development of EDFAs sparked a revolution in the fiber optics telecommunication industry. At the time EDFAs exhibited gain from 1525 nm to 1565 nm. This window has since been expanded to 1605 nm, which happens to be the third transmission window. The development of EDFAs pushed scientists and design engineers alike to solve the dispersion problem associated with the fiber at 1550 nm.

This problem of large dispersion at 1550 nm was finally resolved in the 1980s by using a dispersion-shifted fiber[4]. As a result of this there was a shift both in academia and industry away from optoelectronic components that operated around 1300 nm. Currently any new research or optoelectronic product used for industrial applications usually targets the 1550 nm transmission window. By the early 1990s

commercially available optical networks operating around 1550 nm with bit rates of 600 Mbps (OC-12), 2.5 Gbps (OC-48), 10 Gbps (OC-192) became widely deployed. Presently there are field trials on going for OC-768, which has a maximum bit rate of 40 Gbps.

Optoelectronic devices such as modulators, photodetectors, multiplexer etc. must keep a step ahead of the communications industry's need for higher bandwidth. Hence, as the bandwidth exceeds 40 Gbps conventional optoelectronic devices will become obsolete and novel designs will need to be considered.

The photodetector is the component of interest in this thesis, it resides on the receiver end of an optical communication network. These transducers which convert optical energy to electrical energy are present in all modern non-coherent optical communication systems. Currently most optical networks will employ some form of vertically illuminated detector. These conventional vertically illuminated photodetectors are being pressed to their limits in terms of bandwidth-efficiency product. The traveling wave geometry has been presented in the literature[5-6] and represents a possible architecture for increasing the bandwidth-efficiency product of photodetectors. Since the early 1990s there have been several publications in the literature that routinely demonstrate that these devices have bandwidths in excess of 100 GHz, which makes them ideally suited for next generation optical networks[7].

1.2 Thesis Objective and Motivation

Conventional vertically illuminated photodetectors (VPD) suffer from an inherent bandwidth-efficiency limit. That is, the microwave bandwidth and the quantum efficiency product is a constant and in designing a high frequency detector an increase in bandwidth results in a degradation in quantum efficiency, or vice versa. The traveling wave architecture offers a novel approach in solving the bandwidth efficiency limit that VPDs suffer from. Normally in a detector the bandwidth is determined by the load resistance and the depletion capacitance whose product results in a RC time constant, it is this RC time constant that limits the bandwidth of VPD. A designer generally has no control over the load

resistance, usually taken to be 50Ω for most microwave systems. Hence, one degree of freedom remains to increase the bandwidth, or decreasing the depletion or junction capacitance. In attempting to increase the bandwidth a designer must minimize the RC time constant. Since the load resistance is fixed a designer is forced to minimize the depletion capacitance in order to increase the bandwidth of the detector. This results in a degradation in quantum efficiency since the intrinsic depleted region is where light is absorbed and ultimately carriers are generated to produce photocurrent.

The traveling-wave photodetector (TWPD) possesses a distributed capacitance instead of lumped element capacitance and hence decouples the bandwidth and efficiency products seen with the VPDs. Since the capacitance is distributed, the determining factor in bandwidth is not the RC limitation seen with VPDs. As a result the capacitance is distributed hence the devices can be made optically long to obtain relatively high quantum efficiency.

The objective of this project is the design of a high efficiency, high frequency traveling wave photodetector for operation around 1550 nm. The motivation for this work is a result of growing interest in this area from industry as well as academia. That is, the telecommunications industry is in a frenzy to deliver more bandwidth to the end user end and as a result designers are pushed to provide faster and cheaper optoelectronic components to the network. In order for commercial products to become available for next generation systems both industry and universities must conduct core research into novel architectures such as the TWPD to determine their suitability in higher bit rate systems.

1.3 Thesis Contribution

If a successful design is achieved, contributions will reside in the areas of modeling, design and development of a high speed, high efficiency detector at a relevant transmission window. To the author's knowledge there has only been a small amount of work done in modeling such a structure numerically. Most designs presented in the literature have made use of first order approximations in describing the TWPD[8-10] and hence do not accurately characterize the optical and microwave guides using a full wave vectorial approach as has been done in this project. The microwave guide is often taken as a quasi-TEM structure and such a first order approximation may generate discrepancies between the simulated and measured results.

The project will generate a considerable amount of data both from a numerical modeling perspective as well as device design perspective. The work presented here will hopefully contribute significantly to any future designs using this architecture from an empirical as well as an analytical standpoint.

1.4 Thesis Organization

Chapter 2 Photodetectors, will review optical detection and the selection of materials for optical absorption at a specified wavelength. A basic equivalent circuit for a photodetector is presented and the trade off between various parameters such as sensitivity and gain, or bandwidth and efficiency is discussed. The chapter will also review different types of photodetectors such as APDs, Schottkys, p-i-n's, listing their advantages and disadvantages. This is followed by a description of the theory behind traveling wave photodetectors (TWPDs) and the parameters that a designer must consider when implementing this type of detector. The theoretical treatment of TWPDs will discuss the relationship between the optical and microwave modes of propagation, the importance of phase velocity matching; several electrical models will be presented discussing the limitation of each. The limitations to the models

presented here lead to a logical conclusion that a full wave analysis must be undertaken to characterize this device. It is this full wave approach that is discussed in Chapter 3.

Chapter 3 Numerical Analysis Using the Method of Lines (MoL) will present an overview of the Method of Lines listing the advantages and disadvantages of this method over other numerical schemes. An algorithm is presented on how to generate the indirect eigenvalue problem and a derivation is formulated for a non-anisotropic inhomogeneous lossy medium. Since the method is used in the optical waveguide design of the TWPD, a thorough validation of the code and derivation associated with the formulation is done. This validation is done using three separate structures, all of which have previously been analyzed and published in the scientific literature. Monotonic convergence is demonstrated, a dispersion curve is generated and the fields are illustrated. This was done for two lossless rib waveguide structures. The validation of the losses is done and compared via a Schottky contact TWPD.

Chapter 4 Design and Simulation will begin with the choice of diode architecture used for photodetection. In will then describe the material choice discussing the importance of lattice matching, and why quantum well(s) (QWs) were introduced in the design. The chapter will present two designs, discussing the design philosophies for each structure. The layer design will be presented for each structure and the simulated microwave and optical results illustrated. Any assumptions made for the semiconductor, microwave and optical designs will be presented and discussed thoroughly. The mask design is discussed and the foundry limitation pointed out.

Chapter 5 Measurements and Analysis will present the DC measurement results along with the optical and microwave results. The chapter will focus on the original objective for this work, which is the design of a high efficiency, high bandwidth detector at 1550 nm. Although other measurements are given for completeness, emphasis is placed on the bandwidth and responsivity. The results will be compared against theory and, where appropriate, deviations highlighted.

Chapter 6 Conclusion will discuss the successes and shortcomings of the designs. The work done is summarized and conclusions are presented. The thesis ends with a list of recommendations and refinements to this work as well as a list of possible future activities in this area. This list is quite general and applies to students, researchers and designers alike.

Chapter 2 Photodetectors

In order to understand the design criteria needed to fabricate a traveling wave photodetector, one must first have a full comprehension of conventional detectors. This chapter will present the theory behind optical detection including the different semiconductor materials that are available for the detection of optical energy. Following this discussion an overview of the various diode architectures is presented, listing the advantages and disadvantages for each device.

Bandwidth and efficiency are two key design parameters, which must be optimized when designing any detector. These parameters are presented in this chapter and a quantitative discussion of the trade off seen between these two competing criteria is demonstrated rigorously.

With a full overview of the current diode architectures, the traveling wave configuration is presented to the reader, listing the advantages over conventional detectors. The theory behind traveling wave photodetectors is shown both heuristically and mathematically via various closed form models that have been presented in the literature[28].

2.1 Introduction to Optical Materials and Optical Detection

In order for a semiconductor device to be useful as a detector, a material property of the device should be affected by optical radiation. The most commonly used property is the conversion of light into electron-hole (e-h) pairs which can be collected via a properly chosen electrical circuit. When light impinges on a semiconductor, it has a finite probability of scattering an electron in the valence band to the conduction band, provided that the light has more energy than the bandgap energy of the semiconductor. This process is called optical absorption. Figure 2.1 depicts this process of optical absorption of a photon for a direct bandgap semiconductor material.

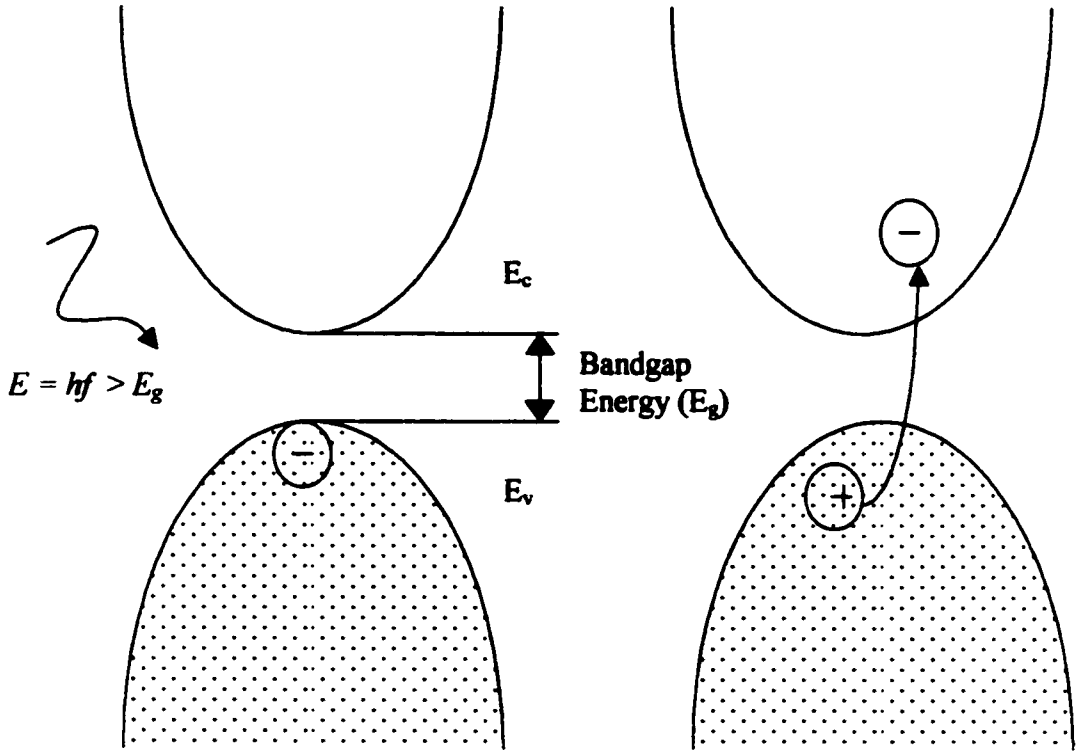

Figure 2.1 Optical absorption for a direct bandgap semiconductor

This process is strongest for direct bandgap semiconductors because the photon can eject an electron from the valence band to the conduction band without the aid of a phonon. Phonons are vibrations in the crystal lattice of the semiconductor. Materials such as GaAs, InP, InGaAs and InGaAsP are all direct bandgap semiconductor materials. These materials all have strong optical absorption coefficients due to the absorption without phonon participation. The work presented in this thesis only involves direct bandgap semiconductors. Although light can be detected via indirect bandgap semiconductors (i.e. detection with phonon participation), these devices are generally less efficient than their direct bandgap cousins and hence are not well suited for high efficiency applications.

Material choice is an extremely important design consideration. Without careful thought and review of this issue optical energy at the design wavelength will not be absorbed; hence, no microwave signal can be

detected. The charge carriers can only be produced if the wavelength is above the cutoff wavelength of the bandgap or, equivalently, if the photon of light has more energy than the bandgap energy of the material. If the photon has less energy than the bandgap energy of the material, it will have insufficient energy to eject an electron from the valence band to the conduction and thus no e-h pair will be generated. Instead the energy of the photon will be absorbed by the material and released in the form of heat. As a designer, one must choose materials having a bandgap energy less than the photon energy of interest. In the case of this thesis the wavelength of interest is 1550 nm which is in the third transmission window of fibers as discussed in Chapter 1.

Once a photon has been absorbed an e-h pair is generated and it is these photo-carriers that form the basis of photocurrent. To collect the e-h pairs generated by light, one requires an electric field. In the absence of an electric field the electron and hole will recombine before being collected at their respective ohmic contacts. Thus one must either apply an external bias or use the intrinsic electric field, if one is present. The diode is widely used because it exploits the built in electric fields present in all p-n junctions.

Shown in Figure 2.2 are two modes of operations for any photodiode: photovoltaic and photoconductive. The photovoltaic mode, which is mainly used in solar cells, does not require the use of an external bias and relies on optical energy to generate the current and voltage. This mode is not used in optical communications circuits and hence is of no interest in this thesis.

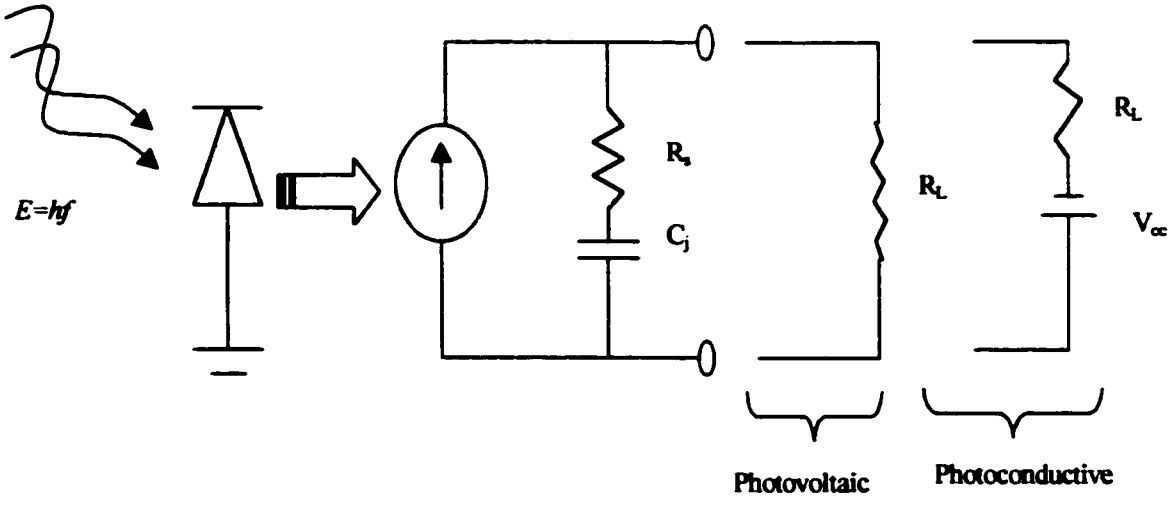

Figure 2.2 Equivalent circuit for a photodiode in photovoltaic and photoconductive mode

The photoconductive mode of operation is used for detectors in optical communication systems and as shown in Figure 2.2 makes use of an external bias to completely deplete the detection layer of charge carriers.

While photovoltaic operation can be used in communication diodes this is generally not done since the collection of e-h pairs is very slow in this mode. The purpose of applying an external bias in photoconductive mode is that the electric field generated completely depletes the intrinsic layer of charge carriers. Thus, any e-h pairs generated would very quickly be swept to their contacts at their saturation velocity, hence increasing the bandwidth of the device.

Another very important benefit of operating the detectors in photoconductive mode is the possibility of internal gain in the device. That is, it is possible to collect more than one electron (or hole) for each photon absorbed. If each photon contributed to the formation of one e-h pair being collected at the contact, then there is no internal gain in the system. If the photogenerated electron impacts another electron in the valence band and ejects it into the conduction band, another carrier pair is formed which can be collected by the contacts. This process is called multiplication and is the basis for internal gain in avalanche detectors.

The next section shall discuss three distinct diode architectures:

- the p-i-n diode
- the avalanche diode
- the Schottky diode

Each configuration has its advantages and disadvantages, which shall be outlined in Section 2.5.

2.2 p-i-n Photodetectors

Figure 2.3 depicts a p-i-n detector which is very common in optical communication networks. It operates under a strong reverse bias condition, it has no internal gain, very low dark or leakage current and a very fast frequency response. The bias is applied such that the intrinsic region is completely depleted of charge carriers. Any e-h pair generated in this region will be very quickly swept, at their saturation velocity, to their p^{++} and n^{++} contacts. However, the bias is not so strong as to cause material breakdown as is the case with avalanche photodiodes (APDs).

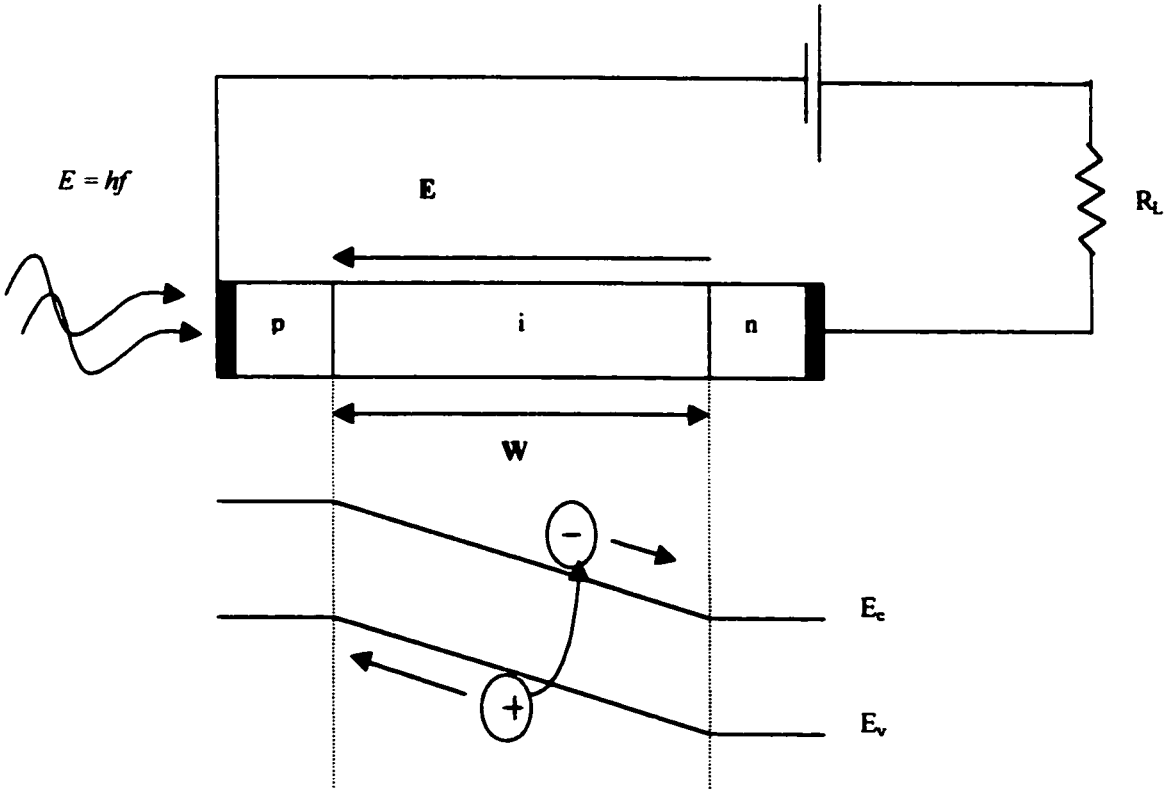

Figure 2.3 p-i-n photodetector

The dark current is inherently low in p-i-n diodes which means that these types of detectors are generally much quieter than other diode architectures. One reason for the low dark current is the lack of internal gain. This is due to the fact that p-i-n devices operate in a non-breakdown mode and as a result no carrier multiplication takes place.

Ideally the diode dark current is independent of the applied bias. In practice there is often a small slope present under reverse bias. Thus, the dark current may vary slightly with bias, but the change is quite small and can be considered a constant.

Having inherently low dark current translates into the device having low noise characteristics and high sensitivity. These devices are also inherently fast, require a low bias voltage and are highly reliable. This makes them ideally suited for long haul applications and they have been the principal detector chosen by designers faced with this scenario.

2.3 Avalanche Photodetectors

Avalanche photodetectors (APDs) form another important class of detectors. Unlike the p-i-n configuration where the gain can at most be unity, the avalanche diode can possess a very large gain due to the multiplication process, which is initiated when the device is in breakdown.

In most electronic devices the breakdown voltage limits their operation, but in APDs it is used to generate gain. This is due to the fact that the drift velocity is directly proportional to the electric field (i.e. $v_d \propto E$). Thus, when a very strong bias is applied this creates a very strong electric field. The result is an increase in drift velocity, or equivalently the kinetic energy of the electron. At some critical value of electric field, the electron has a kinetic energy greater than the band gap energy of the semiconductor. At this point when the electron collides with the crystal lattice it can eject another electron from the valence band to the conduction band, creating an e-h pair. These carriers may themselves have sufficient kinetic energy such that when they collide with other electrons in the crystal they in turn create more e-h pairs. This process of avalanche multiplication is conceptually illustrated in Figure 2.4.

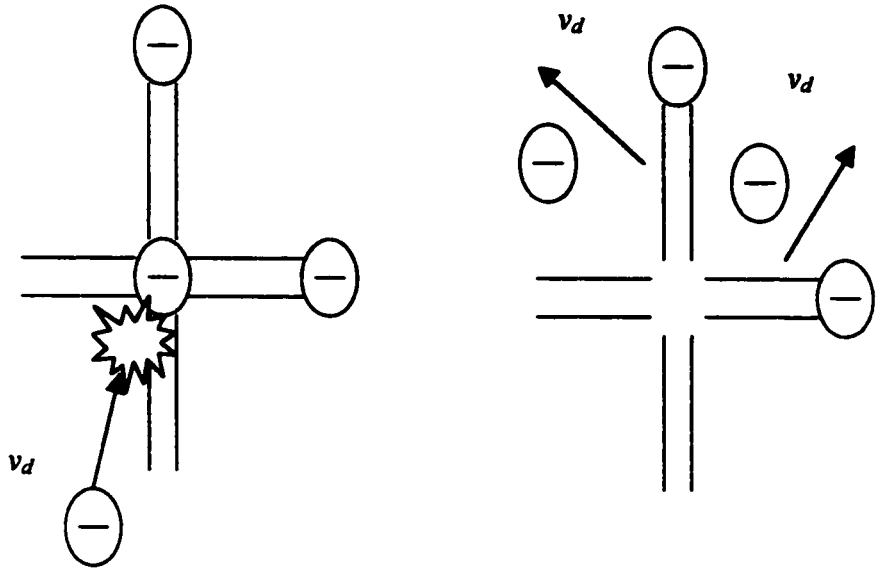

Figure 2.4 The process of avalanche multiplication

The key attraction for APDs is their gain and sensitivity. However, the price to be paid for the increased sensitivity and internal gain is a reduction in bandwidth and an increased level of noise. The multiplication process responsible for the internal gain in APDs is a random phenomenon and hence makes these diodes quite noisy. Unlike p-i-n detectors where the reverse bias photocurrent is essentially a constant, the APD's photocurrent is a function of the applied bias as well as a function of the thermal gradient.

APDs are not well suited for long haul application because they require a highly stable voltage supply to apply the reverse bias. They also require thermal stabilization circuitry since the current gain is a function of thermal parameters. In terms of reliability, they are generally considered to have a poorer performance than p-i-n structures. Thus, their use is presently limited to applications where high gain takes precedence over all other design parameters.

2.4 Schottky Barrier Diodes

An extremely important class of photodetectors involves the use of a Schottky barrier diode. This diode is produced between a metal and a lightly doped semiconductor material. The key advantage of the Schottky barrier devices is that they are a majority carrier device and therefore do not suffer from the speed degradation arising from minority carrier lifetime and recombination. Another advantage is that these devices have, in general, a lower overall series resistance than their p-i-n counterpart. Both of these parameters help to increase the overall bandwidth of the diode when compared with their p-i-n counterpart. The Schottky diode is able to achieve this because of the low resistance of the metal. Shown in Figure 2.5 is the energy band profile of a Schottky barrier diode at thermal equilibrium.

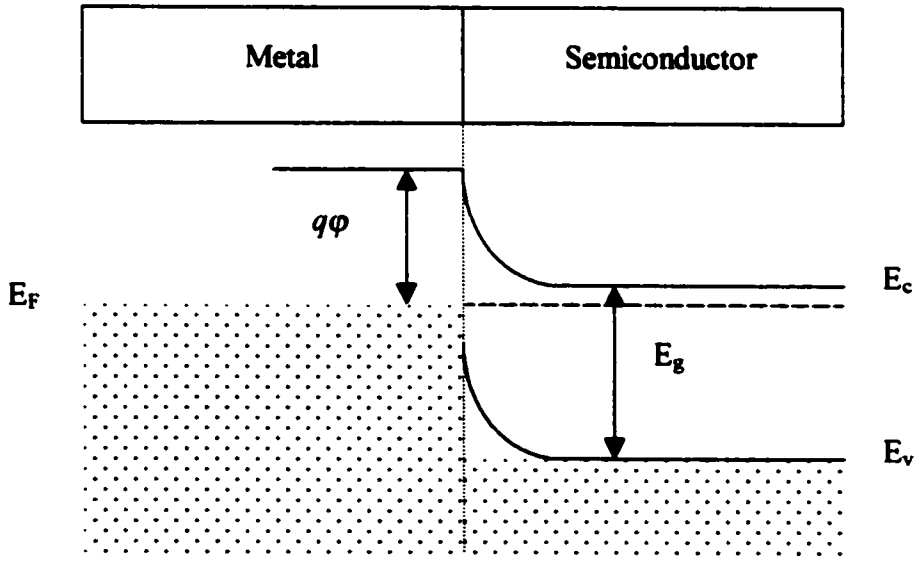

Figure 2.5 Schottky diode band profile

There are two important regions of operation for this detector:

- $hf > q\varphi$: In this case, electrons can be excited in the metal barrier to overcome the Schottky barrier height and as a result, a photocurrent will flow in the device. This current will add to the dark current in the reverse biased diode.
- $hf > E_g$ in this case, e-h pairs will be created in the semiconductor. As in the case of the other photodiodes, the carriers generated in the depletion region will be swept out to produce photocurrent.

Since these devices are majority carrier device they are not limited by recombination or minority carrier lifetime, hence can be made extremely fast. These devices are the ideal configuration for the design of a high speed traveling wave photodetector. For high speed applications the Schottky barrier diode is the photodiode of choice; however, this architecture was not chosen for reasons which shall be discussed in Chapter 4.

2.5 Summary of Photodiode Architectures

In the previous sections we have discussed three common architectures for photodiodes. Table 2.1 summarizes them.

Photodiodes Type	Key Characteristics
p-i-n diode	• Low dark current • High speed of operation • No internal gain present • Low noise • Reliable i.e. low mean time between failures (MTBF) • Low voltage requirements • No thermal stability issues
avalanche diode	• High internal gain is possible • Random nature of multiplication process is responsible for gain. The same process makes these devices noisier than other photodiode architectures. • Photocurrent varies as a function of temperature hence, thermal stabilization circuitry may be required. • MTBF higher than other architecture. • high dark current • Highly stable voltage source is required.
Schottky diode	• No minority carrier lifetime issues or recombination issues lead to devices with exceptionally high speeds. • Low dark current. • Low series resistance. • Simplicity of fabrication.

Table 2.1 Photodiode architecture and characteristics

Each detector has its own attributes, which may make its use advantageous in specific situations. Using the above information a diode architecture was chosen. The reasons for the selection will be given in the design chapter.

2.6 Factors Affecting the Bandwidth-Efficiency Product of VPDs

The previous section discussed the different photodetector architectures. This section will discuss the factors limiting the bandwidth-efficiency product of conventional detectors. The term "***conventional detectors***" refers to all detectors that are vertically illuminated, which accounts for the vast majority of commercially available photodiodes. Most conventional detectors have the incident optical field vertically illuminated and parallel to the applied electric field. This type of design configuration causes two design parameters, the bandwidth and efficiency to be coupled via a common electrical parameter: the depletion layer capacitance. This result is an inability for conventional detectors to achieve both high efficiency and high bandwidth.

Photodetectors that are used in optical communication systems are essentially optical to electrical transducers. They are used to convert optical energy to electrical energy and are present in all modern noncoherent optical communication networks. They are capable of converting optical signals modulated at high frequency into electrical signals. Generally photodetectors can be characterized by two key figures of merit:

- microwave or electrical bandwidth,
- quantum efficiency, or an equally effective measure, the responsivity

Bandwidth is generally taken to be the lowest frequency at which the magnitude response is 3 dB down from the DC (zero frequency) response. External quantum efficiency is the ratio of charges collected per unit time to incident photons per unit time. The bandwidth efficiency product is an important figure of merit for all photodetectors. In traditional VPDs this product is a constant and as a result a designer would not be able to indefinitely increase the bandwidth of a detector without degrading the efficiency or vice versa.

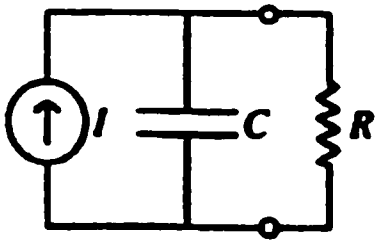

Figure 2.6 Equivalent circuit for a photodetector.

A simplified equivalent circuit diagram of a photodetector is drawn in Figure 2.6. The bandwidth of such a device is limited by the response of the current source (i.e. transit time) and the response of the overall lumped element receiver circuit.

The ultimate speed of all photodetectors is determined by the velocities of the carriers generated in the depletion region and the distances these carriers must travel before being collected by their respective ohmic contacts. In p-i-n and APD detectors the speed is ultimately limited by the slower carriers which are the holes at their saturation velocity.

In conventional VPDs if one assumes a uniform carrier generation across the depletion layer and the carrier velocities are equal and constant, then the time it takes the carriers to travel to their respective contact is called the transit time. This is given by the following first order expression:

$$t_{tr} = \frac{W}{v_s} \tag{2-1}$$

where t_{tr} is the transit time, v_s is the saturation velocity and W is the width of the intrinsic region. Hence, from (2-1) the thinner the depletion region the faster the detector. Thus, the speed of all photodetectors is ultimately dictated by the speed that the carriers can travel to their contacts. In reality there are other factors that will limit the bandwidth of a photodetector before the transit time limitation is approached.

These other factors include such parameters as the detector-receiver RC time constant, microwave loss, carrier recombination and parasitic capacitance.

Of all the factors limiting bandwidth in a conventional photodiode, the RC time constant is the one of key concern. That is, the product of the junction capacitance and load resistance determines the 3 dB bandwidth of the device. This expression is given by:

$$f_{RC} = \frac{1}{2\pi RC} \tag{2-2}$$

where R is the load resistance and C is the depletion layer capacitance or junction capacitance given by

$$C_{junction} = \frac{\varepsilon A}{W} \tag{2-3}$$

where ε is the permittivity of the material, A is the cross sectional area of the diode and W is the thickness of the intrinsic layer.

As can be seen from the above expression the junction or depletion layer capacitance is determined by the physical geometry of the device. This physical geometry also determines another very important design parameter, the quantum efficiency or equivalently the responsivity. These two terms are very closely related and will at times be used interchangeably.

Quantum efficiency is defined as the probability that a single photon incident on the device generates an electron-hole pair that contributes to photocurrent and is directly related to the area of the intrinsic region in VPDs. In order to achieve a fast device, one must minimize the depletion layer capacitance; however, the trade off is a degradation in quantum efficiency. The external quantum efficiency is defined as:

$$\eta_{external} = \frac{\#\text{ of e - h pairs contributing to photocurrent/s}}{\#\text{ of photons incident on the detector/s}} = (1-R)\left[1-e^{-\alpha W}\right] \qquad (2\text{-}4)$$

where R is the optical power reflected at the surface and α represents the optical attenuation constant or the fraction of photons absorbed, W is the width of the intrinsic region.

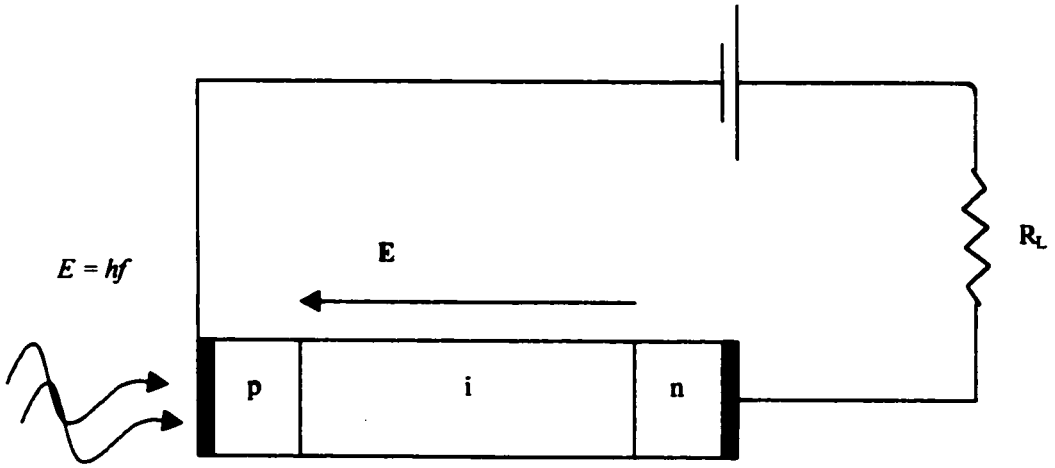

Figure 2.7 Conceptual view of a vertically illuminated photodetector

The external quantum efficiency is also very closely related to the responsivity which is defined as:

$$R = \frac{\text{Photocurrent flowing in the device}}{\text{Incident optical power}} = \frac{\eta_{external} q}{hf} \qquad (2\text{-}4a)$$

Where q is the fundamental charge given as 1.602×10^{-19} C, h is Planck's constant given as 6.6262×10^{-34} J·s and f is the frequency. The units of responsivity are given in ampere per watt (i.e. A/W).

Shown in Figure 2.7 is a conceptual view of a vertically illuminated detector. In this type of architecture light is incident perpendicularly to the device layers. The light is coupled directly into the absorbing layer where it creates charge carriers. From equation (2-1) we can see that a thin depletion layer is required for a large bandwidth, however this results in a reduction in quantum efficiency. As the depletion layer becomes

very thin, equation (2-4) becomes $\eta \cong (1-R)\alpha W$. A fundamental limit to the bandwidth efficiency product for VPDs can be derived from (2-1) and (2-4) by assuming that the device is not limited by the RC time constant imposed by (2-2). The bandwidth efficiency product then takes on the following first order expression:

$$(Bandwidth)(efficiency) = \alpha v_s \tag{2-5}$$

where zero optical reflection is assumed. For conventional detectors the maximum possible theoretical bandwidth efficiency product using this relationship is approximately 40 GHz.

2.7 Optimizing the Frequency Response of Detectors

Once the material choice is selected and the diode architecture is chosen, the important issues in detector design that remain are:

- *Minimizing surface reflections*: This is usually done by applying an anti-reflective coating which reduces the reflection losses. We see from equation (2-4) that reducing the reflection will increase the external quantum efficiency.
- *Minimizing carrier recombination*: Since we are dealing with a diode that has both electrons and holes, minimizing recombination becomes a key design issue. That is, there is a finite probability the electrons traveling to their n^{++} contact and holes traveling to their p^{++} contact will recombine before being collected. To increase efficiency it is desirable to minimize recombinations in the depletion region. This can be achieved by using a material of high purity so as to minimize the number of traps in this region.
- *Minimize the transit time*: As stated earlier the device is ultimately limited by the speed at which the electrons and holes can travel to their respective contacts. For high speed of operation the depletion region should be made as thin as possible.

In all detectors a designer must try to maximize optical absorption α to increase quantum efficiency. In a conventional detector this is done by making the depletion region larger however, this results in a degradation in bandwidth. The use of other devices architectures such as the TWPD may alleviate this issue.

The above points give a set of general design parameters for any detector. Specific detectors will have specific criteria that are unique however, these details will only add to the general list presented above.

2.8 Waveguide Photodetectors (WGPDs)

One way of increasing the bandwidth efficiency product is to try to decouple the depletion layer thickness from either the bandwidth or quantum efficiency expressions. A waveguide photodetector (WGPD) which is illustrated in Figure 2.8[11-18] can partially mitigate the interdependence of bandwidth and efficiency.

The WGPD is a planar photodetector in which optically transparent dielectric cladding layers are about the absorbing core forming a dielectric optical waveguide[19-23]. The optical propagation is guided perpendicularly to the carrier electric drift field. This allows a long absorption path while keeping the junction area small, thus partially decoupling the relationship of bandwidth and quantum efficiency.

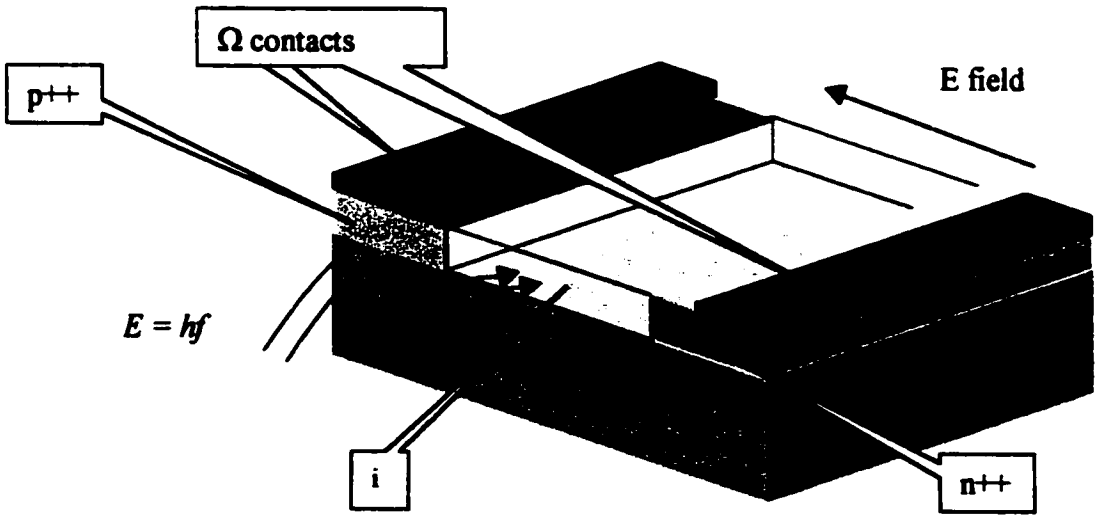

Figure 2.8 p-i-n waveguide photodetector

Due to the fact that WGPDs are generally designed without regard for the propagation of electrical waves this results in a large impedance mismatch between the detector and the load. Figure 2.9 illustrates the equivalent electrical circuit for a WGPD.

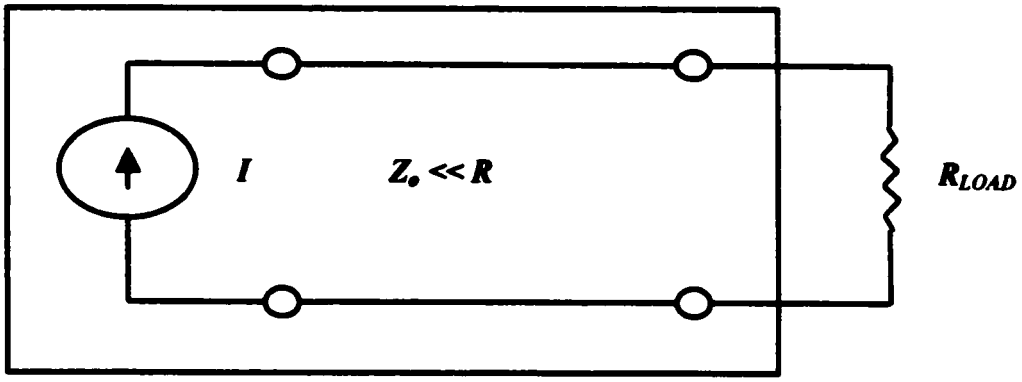

Figure 2.9 Equivalent circuit for a WGPD

Multiple electrical reflections due to a small capacitance cause the entire junction area to participate in the response, thus these detectors suffer from the same RC bandwidth limitation as earlier. Due to the participation of the entire junction area in the response of the device the WGPD can be viewed electrically as a lumped element device. Despite this, waveguide detectors have offered superior bandwidth-efficiency products when compared directly to their VPD counterpart. This is a result of the partial decoupling of the depletion layer thickness from the bandwidth and efficiency terms. The scientific literature has reported WGPD's on GaAs/InP that have bandwidth-efficiency products of 55 GHz[24]. This is inherently larger than their vertically illuminated counterparts. This type of structure is ideally suited for integration with other optical components[25] such as low noise or transimpedance preamplifiers.

2.9 Traveling Wave Photodetectors (TWPDs)

The traveling wave photodetector (TWPD) is a fully distributed structure that overcomes the RC bandwidth limitation of the lumped element WGPD, while retaining certain key advantages of this architecture. Based

on the WGPD architecture the TWPD differs in the sense that it has an electrode arrangement designed to support travelling electrical waves and its characteristic impedance is matched to that of the external circuits. This is shown in the simplified equivalent circuit diagram in Figure 2.10 [26].

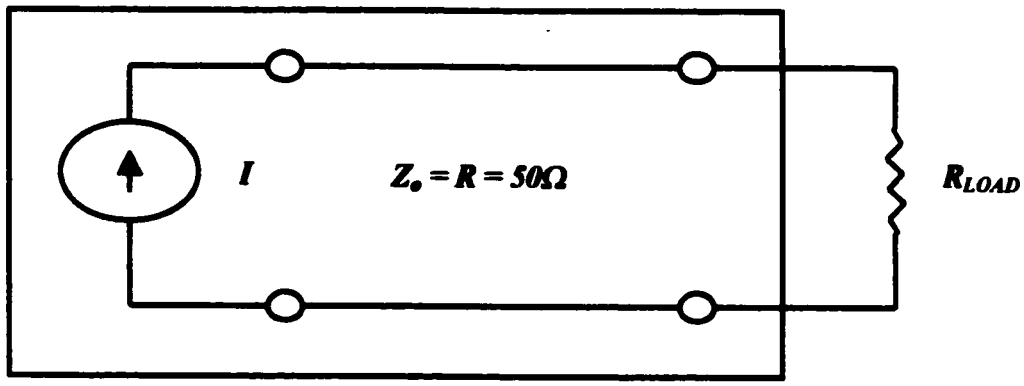

Figure 2.10 Equivalent circuit for a traveling wave photodetector (TWPD)

The TWPD is modeled by a terminated section of transmission line with a current source which is exponentially decaying as it propagates down the optical guide. We expect the TWPD bandwidth to be limited by the velocity mismatch between the optical group velocity and the electrical phase velocity, as opposed to the RC limitations seen with conventional detectors. This architecture is not subject to the same bandwidth limitation as seen with other lumped element detectors. They have been reported to exhibit simultaneously large bandwidth and efficiency[27].

2.10 Theory of Traveling Wave Photodetectors

A traveling wave detector is obtained when two distinct waves interact as they propagate down their respective waveguides. It is the interaction of the optical and electrical waves that justifies the term traveling wave. If the interaction of the waves occurs in a coherent fashion as they propagate down their respective waveguides, then the waves are said to be velocity matched. The length of interest in this case is determined by the optical absorption distance. A typical TWPD structure is shown in Figure 2.11.

There are generally three analytical models that exist and are used to describe the microwave guiding as well as the bandwidth limitation of any TWPD. They are:

- Waveguide Model
- Equivalent Circuit Model
- Velocity Mismatch Bandwidth Model

The waveguide model makes the simplification that the device is equivalent to a dielectric slab guide and the microwaves will propagate in TM mode in this guide[28]. The method of images is then applied to the p-i-n structure and the transverse resonance technique is used to solve the dispersion relationship. This yields the longitudinal propagation constant k_z, which can be used to determine the magnitude of the fields, microwave losses, characteristic impedances and phase velocity for the TWPD in the geometry of interest.

The equivalent circuit model further simplifies the microwave guide by defining a distributed capacitance, inductance, resistance and conductance. From these circuit parameters, a transmission line model is generated[29]. This model is generally less accurate than the waveguide model but does not require us to know the propagation constant of the guide, only the physical parameters and dimensions.

The velocity mismatch bandwidth model takes a slightly different approach in allowing us to understand the device characteristics. The previous two models do not tell us anything about whether velocity

matching is important in this device. That is, we know that there will be some interaction between the microwave and optical signals but is it necessary for that interaction to be coherent (i.e. velocity matched)? Looking at the TWPD from this perspective will allow us to formulate a closed form analytical expression which will give us some indication as to what factors may affect the microwave bandwidth of TWPDs.

All three models give closed form mathematical models of how the TWPD operates electrically. However, to model this type of device accurately, a full wave vectorial analysis of the mode profile is necessary. Such an analysis was done using the Method of Lines (MoL) which is a full wave vectorial technique. This full wave analysis was used to design and optimize the optical waveguide for the TWPD. It shall be presented in detail in Chapter 3.

2.11 Photodetector Electrical Waveguide

Most designs presented in the literature have generally shown the TWPD to be electrically very short but optically long[30-33]. The interaction of the optical and electrical waves, defined as the photodetection length occurs over a short optical distance. It is this length, along with the electrical and optical wave velocities, that defines the device's response. Thus, one requires a distributed, rather than lumped element model to characterize this type of device.

As stated in Section 2.9 the TWPD is based on a WGPD. The two key characteristics that differentiate TWPD from WGPD are:

- A microwave waveguide that is concomitant with the optical dielectric waveguide
- A microwave characteristic impedance of the electrical guide that is matched to the load impedance.

These features provide for the controlled transmission of the microwave signal as it propagates down the device parallel to the optical signal. The fully distributed TWPD structure drawn in Figure 2.11 allows us to formulate analytical expressions that may offer insight into the electrical propagation characteristics.

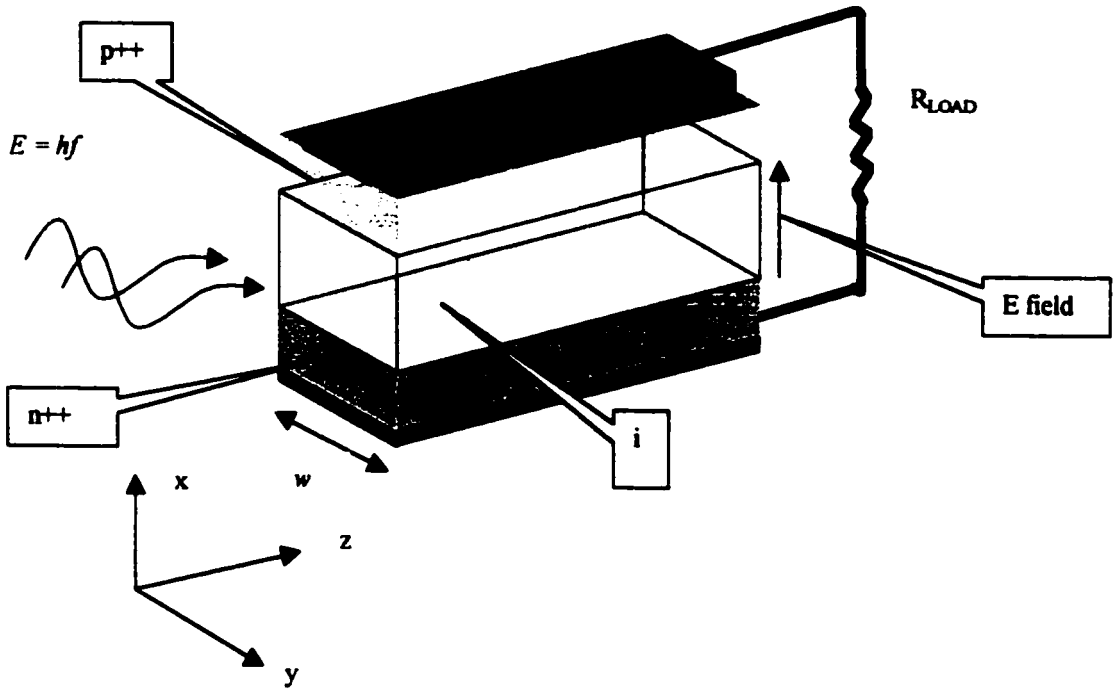

Figure 2.11 p-i-n traveling wave photodetector

In addition to forming the photodiode, the metal clad p-i-n structure is a parallel plate microwave waveguide and the double heterostructure semiconductor layers form a dielectric optical waveguide. Observing the layer structure of the TWPD presented in Figure 2.11, we note that it is similar to metal insulator semiconductor (MIS) structures that have been extensively studied[34-50]. The MIS is formed when one places a metal on a doped semiconductor substrate. This type of structure forms the basis for a wide range of integrated circuits and devices. The microwave propagation on this structure will propagate in what is known as a "slow wave" mode. The name is used to describe the fact that the microwave phase velocity on this structure is much slower than one would normally expect given the permittivities of the material. This slowing of the microwave velocity allows a designer to control the velocity of the electrical wave to achieve velocity matching.

2.12 Electrical Waveguide: Waveguide Model

Figure 2.12 is the cross sectional area of the TWPD structure shown in Figure 2.11. Making the assumption that there is no variation in the *y* direction (i.e. $\partial/\partial y=0$), electromagnetic waves will propagate as TM modes along the *z* direction and resonate transversely in the *x* direction.

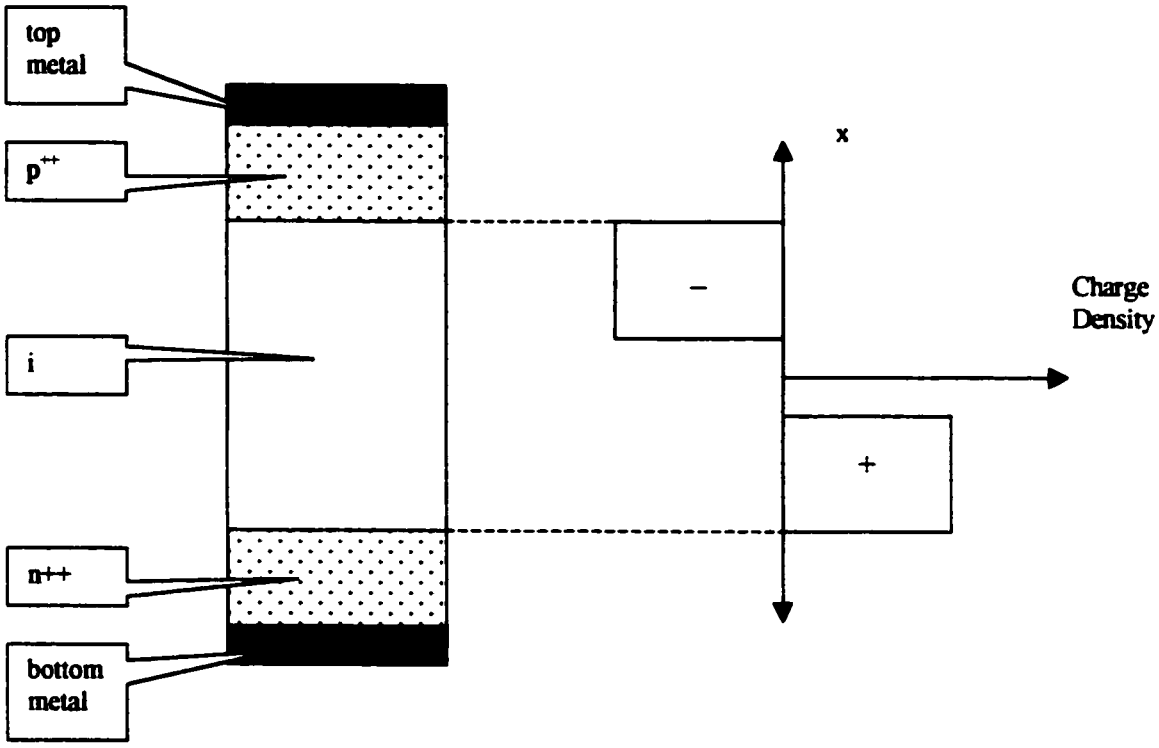

Figure 2.12 Cross sectional view of TWPD and the charge distribution

As a first approximation, the assumption is made that the p^{++} and n^{++} layers of the TWPD have equal conductivity, which in reality is generally not true. Since the p^{++} and n^{++} layers have equal thickness, we now proceed by placing an electric wall about the plane of symmetry, in accordance with image theory. Figure 2.13 shows the result, which looks very similar to an MIS type of structure.

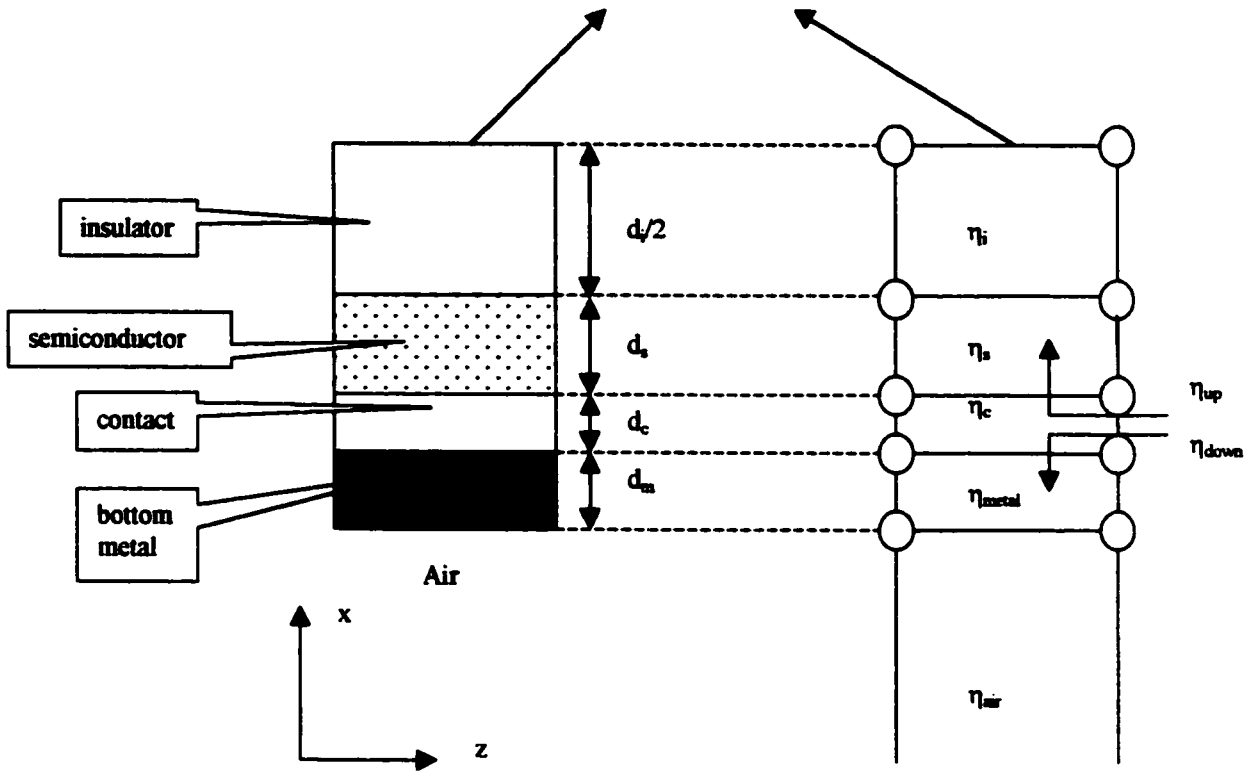

Figure 2.13 Half the TWPD cut about the plane of symmetry

Where d_i, d_s, d_c, and d_m represent the thickness of the insulator or intrinsic layer, semiconductor layer, contact layer and metal layer respectively. The wave impedance of the intrinsic layer, semiconductor layer, contact layer and metal layer is represented by η_i, η_s, η_c and η_m. Thus, the TWPD now looks like a MIS structure with a perfect conductor as the top metal. A thin contact layer is included in the model to simulate the metal semiconductor junction however, it can be eliminated by making $d_c \rightarrow 0$.

We know that the solution to Maxwell's equations in a guided medium will have a propagation constant β of the form:

$$\beta = \sqrt{k^2 - k_c^2} \tag{2-6}$$

where k_c is the cutoff wave number of the guide for a given mode. Thus, if we know k_c we can determine the propagation constant of the guide. The transverse resonance procedure is based on the fact that in a

waveguide, at cutoff, the fields form a standing wave in the transverse plane of the guide[51]. This situation can be modeled with an equivalent transmission line circuit operating at resonance. Thus at resonance along any point on the transmission line the input impedance looking up and down must be zero. Referring to Figure 2.13 we must have the following mathematical condition at resonance, $\eta^{down}_{in} + \eta^{up}_{in} = 0$. The solution to this equation will yield the propagation constant which fully characterizes the mode.

One can characterize the dielectric losses by using a complex dielectric constant (i.e. $\varepsilon = \varepsilon' - j\varepsilon'' - j\sigma/\omega$). The net impedance of the metal air layer can be simplified by observing that the wave impedance of the metal is much smaller than the wave impedance in air. That is, $\eta_{metal} << 120\pi$ where $\eta_{metal} = (j\omega\mu_o/\sigma_{metal})^{1/2}$, thus using the familiar transmission line equation[51] we have:

$$\eta_{mo} \approx \eta_{metal} \coth\left[(1+j)\frac{d_m}{\delta_{sm}}\right] \tag{2-7}$$

where δ_{sm} is the skin depth of the metal given by:

$$\delta_{sm} = \sqrt{\frac{1}{\pi f \mu_o \sigma_m}} \tag{2-8}$$

Referring to Figure 2.13 at resonance we have the following expression:

$$\eta_c\left[\frac{\eta_{mo} + j\eta_c \tan(k_{xc}d_c)}{\eta_c + j\eta_{mo}\tan(k_{xc}d_c)}\right] + j\eta_s\left[\frac{\eta_i \tan\left(\frac{k_{xi}d_i}{2}\right) + j\eta_s \tan(k_{xs}d_s)}{\eta_s - \eta_i \tan\left(\frac{k_{xi}d_i}{2}\right)\tan(k_{xs}d_s)}\right] = 0 \tag{2-9}$$

The above equation is solved numerically for k_z using the dispersion relationship:

$$k_z = \sqrt{\omega^2 \mu_o \varepsilon_t - k_x^2} \tag{2-10}$$

where the t index represents the semiconductor, metal or contact layer permittivity respectively. The solution to (2-9) yields the longitudinal propagation constant.

2.13 Electrical Waveguide: Equivalent Circuit Model

Despite not knowing the exact nature of the field we can still make several observations about the fields in this structure. We expect most of the voltage drop to occur in the x direction, across the intrinsic region, thus the E_x field component is much larger than the E_z field component. Hence, what we have is a top and bottom metallization and a dielectric material in between, which is very similar to the architecture of a microstrip line. It is reasonable to assume that the TWPD exhibits a quasi-TEM mode of propagation. The transmission line equivalent circuit model is thus another closed form analytical model that can be used to understand the microwave waveguiding behavior of TWPDs.

Such a circuit for a TWPD is shown in Figure 2.14, and the element values for parallel plate TWPD are listed in the formulas below[28].

$$\begin{aligned} Z_c &= \frac{\rho_c}{1 + j\omega\rho_c\varepsilon_c}\frac{2d_c}{w} & Z_m &= \eta_{mo}\frac{2}{w} \\ Z_s &= \frac{\rho_s}{1 + j\omega\rho_s\varepsilon_s}\frac{2d_s}{w} & G_s &= \frac{\sigma_s}{3}\frac{wd_s}{2} \\ C_i &= \frac{\varepsilon_i w}{d_i} & L_m &= \frac{\mu_o D}{w} \end{aligned} \tag{2-11}$$

where ρ_i, ρ_c, ρ_s represent the resistivity of the intrinsic layer, contact layer, semiconductor layer and w represents the width of the waveguide as shown in Figure 2.11. Conduction and displacement currents in the contact and the semiconductor layers are accounted for by resistances in parallel with capacitance as shown in Figure 2.14, which models the device as presented in Figure 2.13. At frequencies far below the

dielectric relaxation frequencies of the contact and semiconductor layers ($\omega\rho_c\varepsilon_c \ll 1$ and $\omega\rho_s\varepsilon_s \ll 1$), the i-layer capacitance dominates the overall transmission line capacitance.

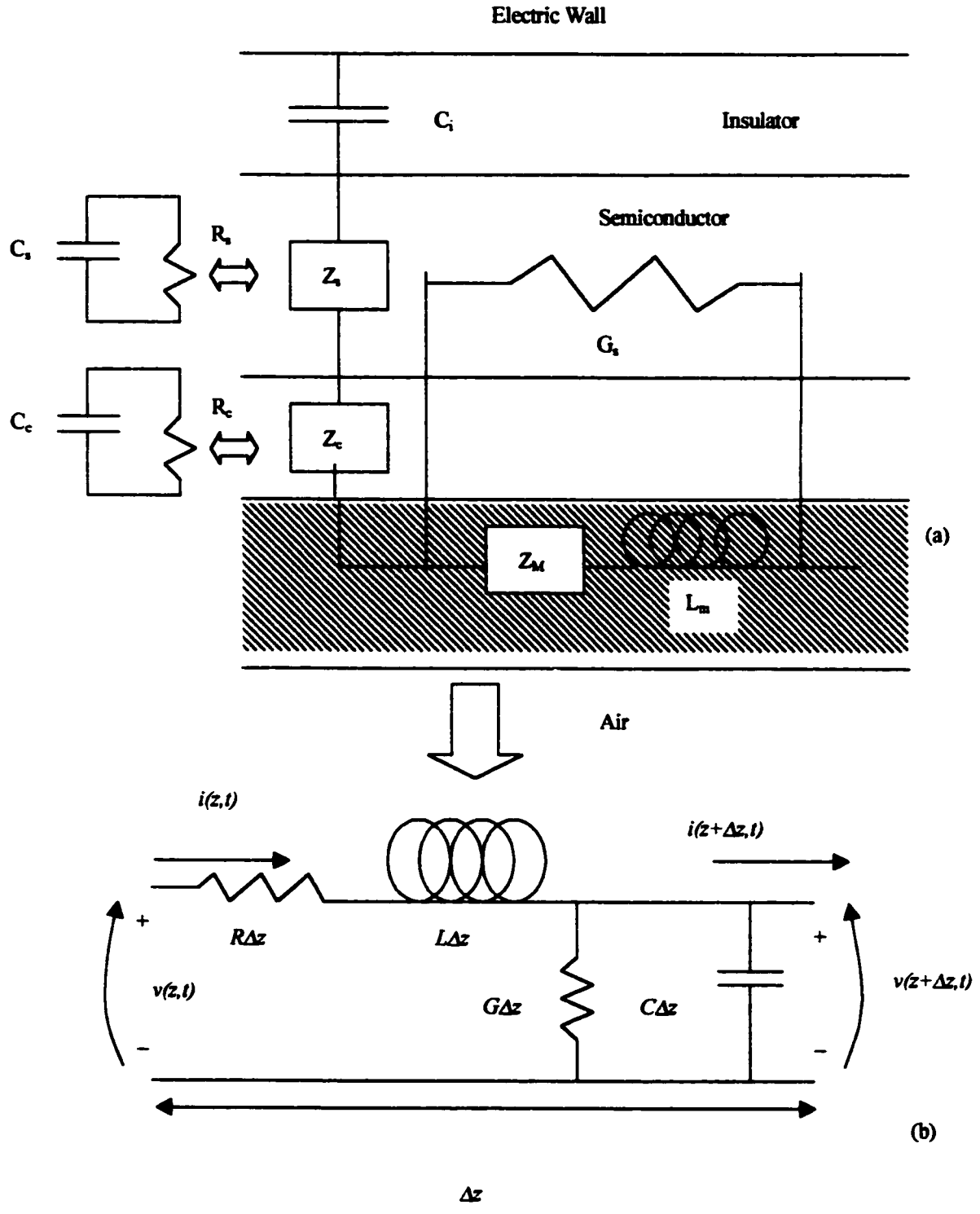

Figure 2.14 Equivalent transmission line circuit for TWPD

While the i layer capacitance is inversely proportional to the i layer thickness, d_i, the inductance per unit length is proportional to the overall thickness, $D = 2d_i + d_s + d_c$. These dependencies on different thickness reflect the spatial separation of the voltage and current, which results in a slow wave effect.

The transverse wave impedance η_{mo} of the metal air layer expressed in (2-7) is also the metal impedance Z_m listed in (2-11) for the waveguide equivalent circuit.

The transmission line propagation characteristics may be found by comparing the equivalent circuit model for the TWPD in Figure 2.14a to the general transmission line model in Figure 2.14b. The microwave losses and propagation velocity are found directly from the attenuation constant α and the phase constant β. The voltage and current waves propagating on the transmission line are related by the characteristic impedance. All of these parameters are found through the standard transmission line formulas given below:

$$Z_o = \sqrt{\frac{V}{I}} = \sqrt{\frac{R + j\omega L}{G + j\omega C}} \qquad \text{(2-12)}$$
$$\gamma = \alpha + j\beta = \sqrt{(R + j\omega L)(G + j\omega C)}$$

Using complex impedances for the contact and semiconductor layers in the above model increases the accuracy of the propagation constant and characteristic impedance.

Assuming the metal conductivity is large compared to the parallel conductance of the semiconductor layers, $GZ_m << 1$ and some simple expressions for the propagation characteristics can be written.

At frequencies below 1 GHz, ($\omega RC << 1$, and $\omega L/Z_m << 1$), the complex propagation constant and characteristic impedance are given by:

$$\gamma \approx \sqrt{\frac{\omega Z_m C}{2}}(1+j) \tag{2-13}$$

$$Z_o \approx \sqrt{\frac{\omega Z_m C}{2}}(1-j) \tag{2-14}$$

This domain of TWPD operation is characterized by a highly dispersive propagation constant and a characteristic impedance that is dominated by the metal impedance given in (2-7). From a waveguiding perspective, the literature often refers to this as the skin effect mode or surface mode. This domain in general is of no interest in the design of TWPD.

The characterization of the bandwidth usually takes place in the mid frequency range (i.e. $\omega RC \ll 1$, $\omega GL \ll 1$, and $\omega L/Z_m \gg 1$) as a result this domain is of greatest interest to the designer of a TWPD. In this frequency range, the transmission line equivalent circuit shown in Figure 2.14 reduces to that in Figure 2.15

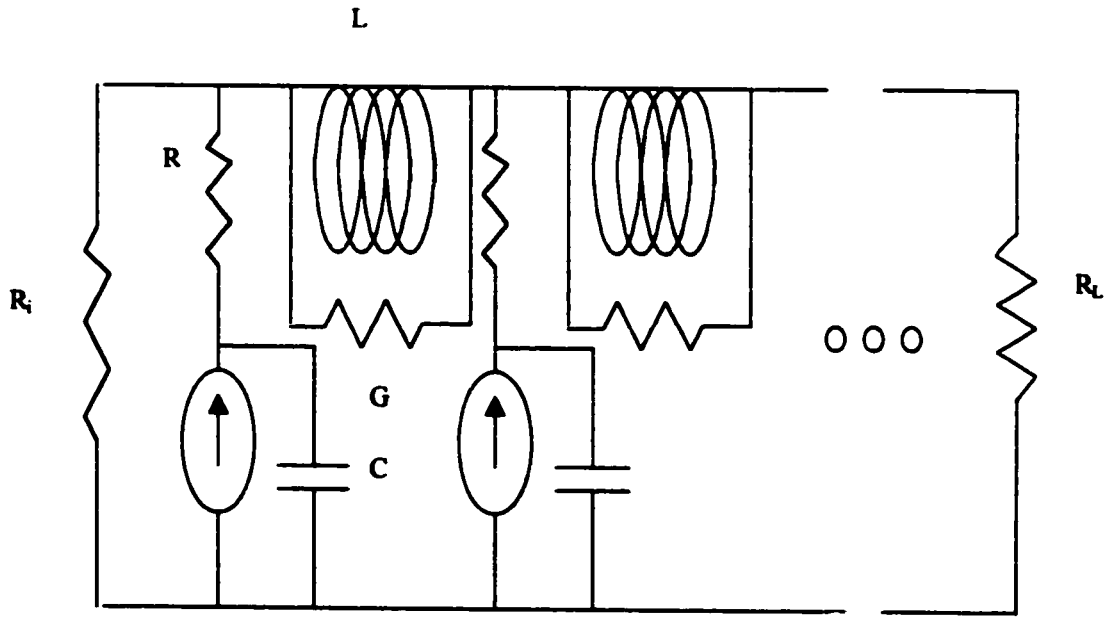

Figure 2.15 Equivalent circuit for TWPD in the midband frequency range

where R_i and R_L are the input impedance and the load impedance and the current sources have been introduced to model the absorption of light. The propagation in this domain is expressed as:

$$\gamma \approx \frac{\omega^2}{2v_e}(RC+GL)+j\frac{\omega}{v_e} \tag{2-15}$$

where $v_e \equiv \omega/\beta = 1/(LC)^{1/2}$ which is the phase velocity of the electrical wave. From (2-15) we see that the microwave loss is directly proportional to the square of the frequency and is also proportional to the *RC* and *GL* terms. We also observe that in the mid-band frequency range the microwave loss cannot be reduced to zero. It is clear from (2-15) that this line may not be considered lossless but instead low loss.

Thus, we expect from the propagation constant that the characteristic impedance will contain an imaginary component.

$$Z_o \approx R_o\left[1+j\frac{\omega}{2}(RC-GL)\right] \tag{2-16}$$

We observe from (2-16) that the imaginary term vanishes when $RC = GL$, where $R_o = (L/C)^{1/2}$ is generally made to be 50Ω. The effect of *RC* and *GL* is to add some reactance to the characteristic impedance. Note that unlike in the low frequency operation the metal impedance does not significantly affect the propagation characteristics. Hence, the operation of the TWPD in this domain is not dispersive.

The expressions in the mid-frequency range are valid from 10 GHz to several hundred of gigahertz. While it is clear from (2-15) that electrically this is a low-loss transmission line this does not prevent us from using the lossless equation seen in the literature, provided that the condition $RC = GL$ is met. Hence,

$$Z_o = \sqrt{\frac{L}{C}} \tag{2-17}$$

$$v_e = \frac{1}{\sqrt{LC}} \tag{2-18}$$

The last domain of operation occurs at very high frequencies. Here the doped semiconductor layer is much thinner that the skin depth. As a result the overall transmission line capacitance is given by $C_m = (1/C_i + 1/C_s + 1/C_c)^{-1}$ where C_i, C_s, and C_c represent the capacitance of the intrinsic layer, semiconductor layer and contact layer respectively. This C_i capacitance now dominates over the semiconductor and contact resistance terms.

In this frequency range the complex propagation constant and characteristic impedance are expressed as:

$$\gamma \approx \frac{\omega^2}{2v_e} G_s L_m + j\frac{\omega}{v_e} \tag{2-19}$$

$$Z_o \approx R_o\left(1 - j\frac{\omega}{2} G_s L_m\right) \tag{2-20}$$

The voltage and current are not spatially separated in this domain, hence no slow wave effect is observed. From a waveguide perspective, the characteristics of this mode are very similar to TEM wave propagating in a lossy dielectric medium. This high frequency domain is also of no interest in the design of TWPD.

2.14 Electrical Waveguide: Velocity Mismatch Bandwidth Model

In an unoptimized TWPD the microwave and optical signals are not velocity matched as they propagate down their respective guides. Since the microwave signal propagates down this guide in slow wave mode, the phase velocity is in general much slower than the optical signal generating it. This results in an incoherent interaction between the microwave and optical signal and may limit the bandwidth of TWPDs.

The velocity mismatch bandwidth model allows a first order approximation of the photodetector bandwidth. Unlike a WGPD where no consideration is given to the characteristic impedance, in a TWPD the characteristic impedance is matched to 50 Ω. It can be shown that this matched transmission line gives a frequency response that is nearly independent of device length. Since this microwave signal propagates in the slow wave mode, it is possible for the microwave phase velocity to be much slower or faster than the optical phase velocity. To generate an expression relating microwave bandwidth to velocity mismatch we must consider two situations. First, when the electrical phase velocity is slower than the optical phase velocity and second when the electrical phase velocity is faster than the optical phase velocity.

Figure 2.16 shows the absorption of optical power and the generation of electrical power versus device length. If we consider a finite number of photons traveling through the device, or mathematically, an impulse packet of photons, the density of these photons as a function of distance is given by:

$$n_{ph}(z,t) = N_{ph}(z)\delta(z - v_o t) \qquad \textbf{(2-21)}$$

Where $N_{ph}(z)$ is the number of photons and v_o is the optical phase velocity. The rate of change of photons per unit length must be directly proportional to optical absorption coefficient and confinement factor, assuming the absorption mechanism is linear and independent of distance (i.e. $\alpha \neq \alpha(z)$).

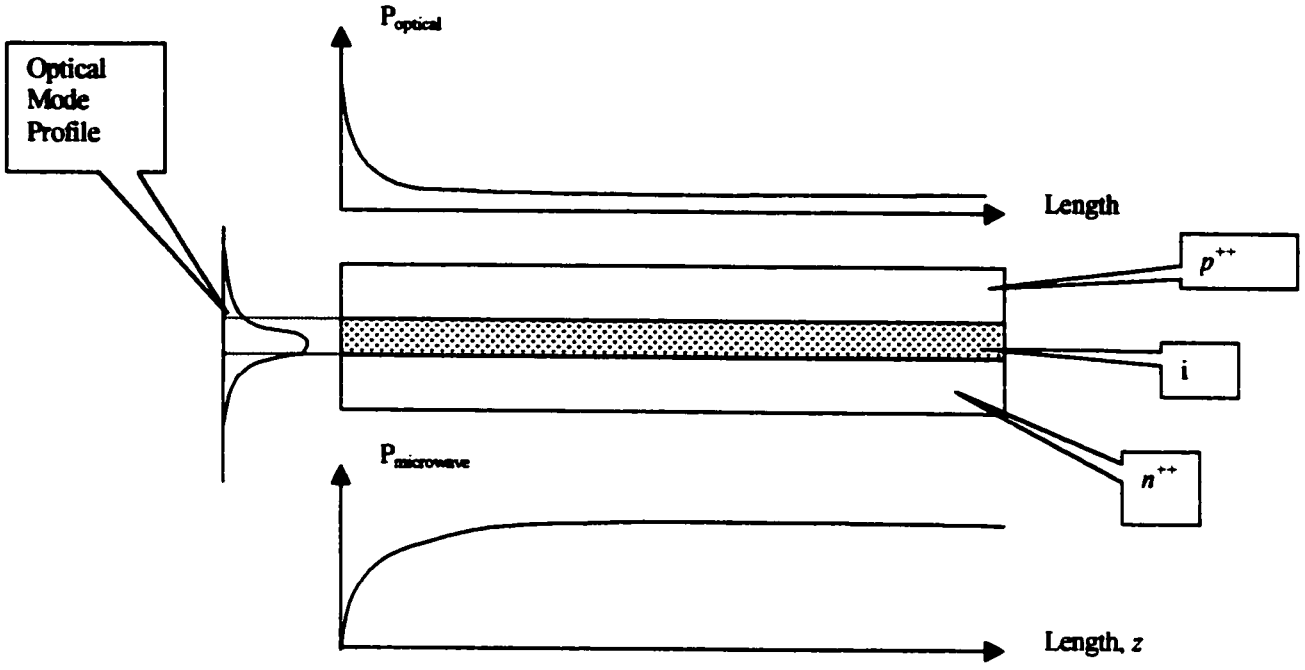

Figure 2.16 Conceptual view of photodetection process

Thus, the number of photons absorbed per unit length must be

$$\frac{dN_{ph}(z)}{dz} = -c_f \alpha N_{ph}(z) \tag{2-22}$$

where α is the absorption coefficient and c_f is the optical confinement factor.

The solution to equation (2-22) yields an exponential decay of optical power as an observer moves away from the impulsive source.

$$N_{ph}(z) = N_{ph}(0)e^{-c_f \alpha z}u(z) \tag{2-23}$$

As discussed earlier the number of e-h pairs being generated is related to the quantum efficiency of the device. Therefore we have an e-h pair density of:

$$n_{e-h}(z) = \eta c_f \alpha N_{ph}(0) e^{-c_f \alpha z} u(z) \tag{2-24}$$

where $u(z)$ is the unit step function. From our previous analysis we know that the microwave signal will propagate in the slow wave mode therefore, the microwave velocity v_e can be faster or slower than the optical phase velocity v_o. If we first consider the situation where $v_e \ll v_o$, the optical signal will pass entirely through the device several times before the microwave signal moves significantly with distance.

The charge density distribution is given by the number of e-h pairs generated multiplied by the elementary charge (i.e. $q = 1.602 \times 10^{-19}$ C). Hence multiplying (2-24) by the elementary charge yields:

$$\rho(z) = \underbrace{N_{ph}(0)\eta q}_{Q} c_f \alpha e^{-c_f \alpha z} u(z) \tag{2-25}$$

The total charge density wave is composed of the forward travelling and the reverse traveling charge density wave that is reflected at the device input end due to refractive index difference between the material and the air:

$$\rho(z,t) = \frac{Q}{2}\left[c_f \alpha e^{-c_f \alpha (z - v_e t)} u(z - v_e t) + \Gamma c_f \alpha e^{c_f \alpha (z - v_e t)} u(v_e t - z)\right] \tag{2-26}$$

where Γ is the microwave reflection coefficient at the detector's input end. Current, defined as coulombs per second is the product of the microwave phase velocity and the charge density wave distribution ρ. The current at the device output is the total forward charge density multiplied by the electrical velocity:

$$i\left(t + \frac{\ell}{t}\right) = \rho\left(z, t + \frac{z}{v_e}\right) v_e \tag{2-27}$$

where ℓ is the length of the device. Substituting (2-26) into (2-27) yields (2-28) which is the microwave current due to an optical impulse response, for the condition when $v_e << v_o$.

$$i\left(t+\frac{\ell}{v_e}\right)=\frac{Q}{2}\left[c_f\alpha v_e e^{c_f\alpha v_e t}u(-t)+\Gamma c_f\alpha v_e e^{-c_f\alpha v_e t}u(t)\right] \tag{2-28}$$

Now we must consider the situation when the microwave velocity is faster than the optical velocity. If we view the total charge density wave from an inertial frame of reference of the forward traveling wave we will generate an expression for the condition when $v_e >> v_o$. This expression is the same as (2-26) if viewed from this inertial frame of reference:

$$\rho(z',t)=\frac{Q}{2}\left[c_f\alpha' e^{-c_f\alpha' z'}u(z')+\Gamma c_f\alpha'' e^{c_f\alpha'' z'}u(-z')\right] \tag{2-29}$$

where $z' = z - v_e t$, $\alpha' = \alpha / \ell - v_e/v_o)$, and $\alpha'' = \alpha / \ell + v_e/v_o)$. Converting back to the detector's frame of reference gives the forward traveling charge density wave:

$$\rho(z,t)=\frac{Q}{2}\left[\frac{c_f\alpha}{1-\frac{v_e}{v_o}}e^{-\left[\frac{c_f\alpha}{1-\frac{v_e}{v_o}}\right](z-v_e t)}u(z-v_e t)+\Gamma\frac{c_f\alpha}{1+\frac{v_e}{v_o}}e^{\left[\frac{c_f\alpha}{1+\frac{v_e}{v_o}}\right](z-v_e t)}u(v_e t-z)\right] \tag{2-30}$$

Inserting (2-30) into (2-27) yields the microwave current when $v_e >> v_o$.

$$i_{rm}(t+\frac{\ell}{v_e})=\frac{Q}{2}\left[\omega_f\left|e^{\omega_f t}u(-\omega_f t)+\Gamma\omega_r e^{-\omega_r t}u(t)\right]\right. \tag{2-31}$$

for $\min(\ell/v_o, \ell/v_e) \le t \le \ell/v_o + 2\ell/v_e$ and zero elsewhere. In the above, ω_f and ω_r are the characteristic frequencies of the forward and reverse waves given as:

$$\omega_f = \frac{c_f \alpha v_e}{1 - \frac{v_e}{v_o}} \tag{2-32}$$

$$\omega_r = \frac{c_f \alpha v_e}{1 + \frac{v_e}{v_o}} \tag{2-33}$$

In spite of the fact that equation (2-31) is derived for the specific case $v_e >> v_o$, careful observation reveals that this is in fact a general description of the current response of a TWPD when an optical impulse response is applied to its input considering only velocity mismatch. This can be deduced by considering the case when $v_e << v_o$ and observing that (2-31) reduces to (2-28).

2.15 Velocity Mismatch Bandwidth Limitation

From the temporal current response (2-31) we can obtain an expression relating the 3 dB microwave bandwidth to the velocity mismatch. This can be done by taking the Fourier transform of (2-31), which yields:

$$\frac{i_{vm}(\omega)}{Q} = \frac{1}{2}\left[\frac{\omega_f}{\omega_f - j\omega} + \Gamma(\omega)\frac{\omega_r}{\omega_r + j\omega}\right] e^{-j\omega\frac{\ell}{v_e}} \tag{2-34}$$

The frequency response of the fractional photocurrent magnitude for real values of input reflection coefficient Γ is given by:

$$\left|\frac{i(\omega)}{Q}\right|^2 = \frac{1}{4}\frac{(\omega_f - \Gamma\omega_r)^2\omega^2 + (1+\Gamma)^2\omega_f{}^2\omega^2_r}{(\omega^2+\omega^2_f)(\omega^2+\omega^2_r)} \qquad \text{(2-35)}$$

We now consider the unusual case when a matched termination is placed at the input of the photodetector. In this scenario the forward traveling microwave will contribute to the frequency response while the reverse traveling wave is absorbed by the input termination (i.e. $\Gamma = 0$). Therefore, (2-35) reduces to a single pole response given by (2-36) for a matched input termination.

$$\left|\frac{i_{vmo}(\omega)}{Q}\right|^2 = \frac{1}{4}\frac{1}{1+\left(\frac{\omega}{\omega_f}\right)^2} \qquad \text{(2-36)}$$

It is observed from equation (2-36) that the 3 dB bandwidth occurs at ω_f.

Using equation (2-35) we have graphed the fractional photocurrent magnitude in dB vs. normalized frequency defined as $\omega/(c_f\alpha v_o)$. This was done for a family of velocity mismatch ratios ranging from $0.10 < v_o/v_o < 1.2$. It was also done for both open ($\Gamma = 1$) and matched input ($\Gamma = 0$) terminations. The graph is shown in Figure 2.17.

It is obvious from both equation (2-35) and Figure 2.17 that by placing a matched termination at the input of the detector the efficiency is reduced by 50%. This is because half the photocurrent is sunk by the input termination.

We also observe from Figure 2.17, that a velocity matched TWPD with matched input termination has no bandwidth limitation.

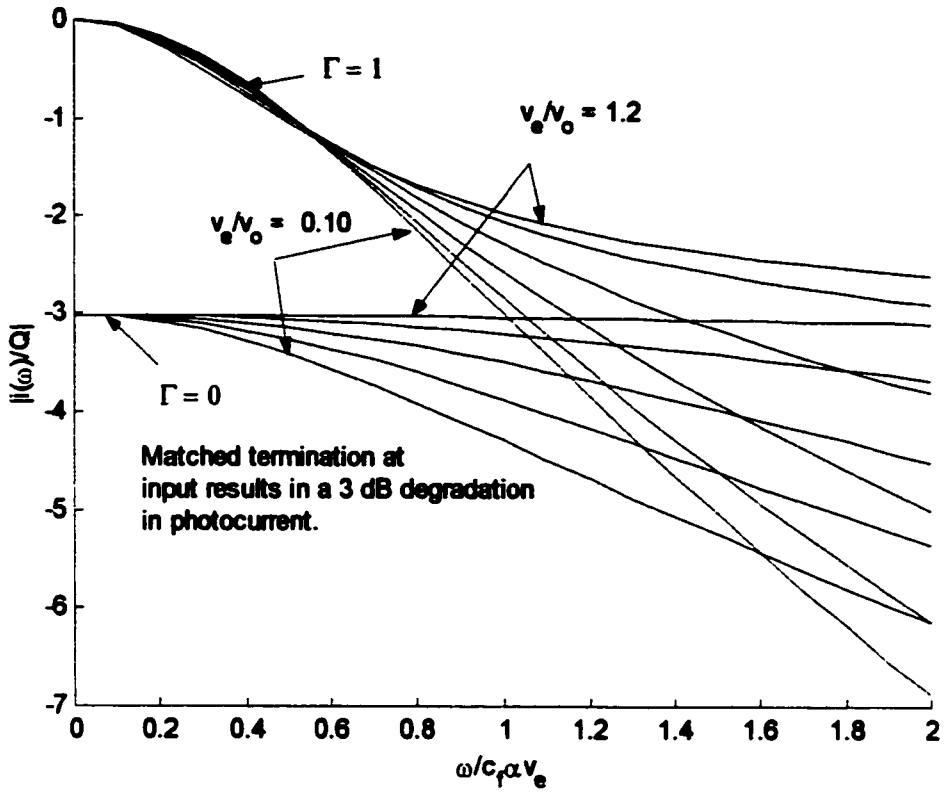

Figure 2.17 Velocity mismatched frequency response

Figure 2.18 is a graph of the normalized bandwidth defined as $2\pi B/(c_f \alpha v_o)$ versus the velocity mismatch ratio v_e/v_o. Figure 2.18 confirms the observations made in Figure 2.17. The velocity mismatch has very little effect on the 3dB bandwidth for an open circuit input termination. In fact, a velocity mismatch of ratio of 1.2 may be desirable when designing a TWPD without an input termination.

We observe that the matched input termination is very much dependent on velocity matching. Despite this, it is interesting to note that a matched TWPD can tolerate up to 50% error in the matching of the velocities and still achieve an infinite bandwidth.

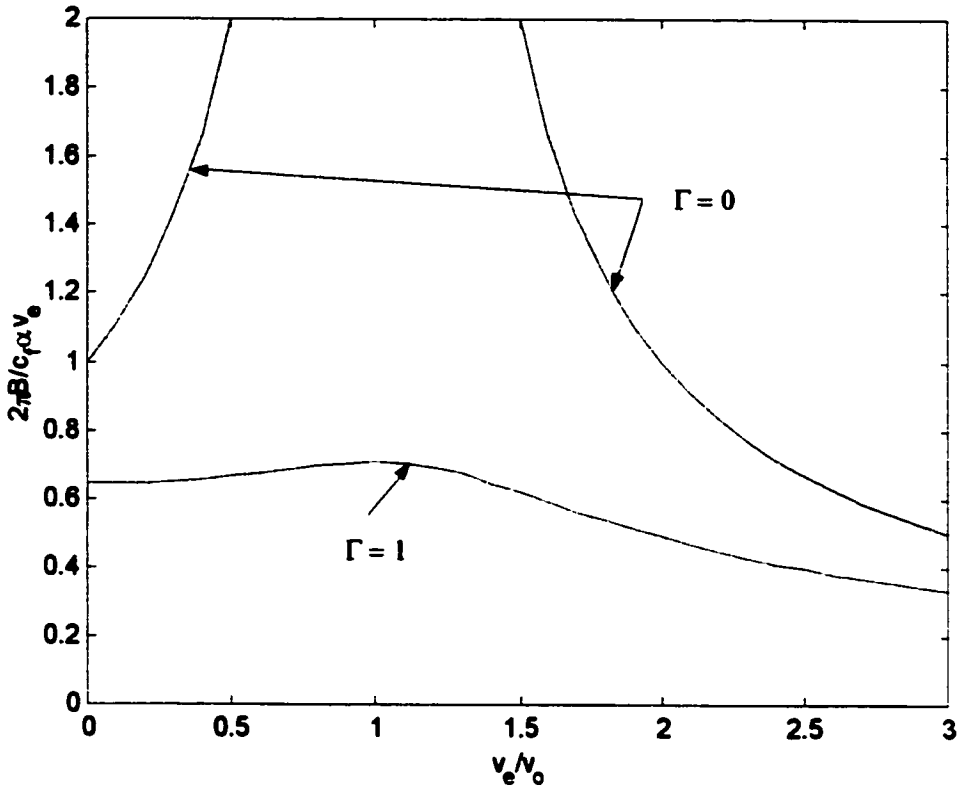

Figure 2.18 Normalized microwave bandwidth vs. velocity mismatch ratio

We can justify the relative independence of velocity matching in an open circuit TWPD by considering the microwave signal generated via an optical impulse response. We observed in this derivation that the total photocurrent is the sum of the forward and backward traveling waves. The forward photocurrent undergoes a temporal compression while the reverse wave reflected wave undergoes a rarefaction as a result the TWPD frequency response for an open circuit termination changes little with velocity mismatch.

From (2-35) we can make the following approximation to the velocity mismatch bandwidth expression provided that $c_f \alpha >> 1$.

$$BW_{VM1} \approx \frac{c_f \alpha v_e}{3\pi} \tag{2-37}$$

We observe that this expression contains no dependence on optical phase velocity. In fact, to increase microwave bandwidth it seems that a designer only need be concerned with increasing optical absorption, microwave phase velocity or confinement factor.

Equation (2-37) can be expressed in a more convenient form by relating characteristic impedance and distributed capacitance to microwave bandwidth.

$$BW \approx \frac{1}{2\pi Z_0 C} \underbrace{\frac{c_f \alpha}{1.5}}_{wA^{-1}_{vm1}} \tag{2-38}$$

From (2-38) we see that the velocity mismatch bandwidth limitation is analogous to the RC bandwidth limitation for a WGPD with a fixed area:

$$A_{vm1} = \frac{1.5w}{c_f \alpha} \tag{2-39}$$

We observe that this effective area associated with the velocity mismatch is independent of device length. Thus, in a WGPD the effective length $\ell = 1.5/(c_f \alpha)$ would only provide a 78% quantum efficiency while a TWPD device can be made physically longer to obtain a 100% quantum efficiency without sacrificing any electrical bandwidth.

A similar expression of effective area can be derived for a matched input termination (i.e. $\Gamma = 0$):

$$A_{vmo} = w \frac{1 - \frac{v_e}{v_o}}{c_f \alpha} \tag{2-40}$$

As expected, since there is no upper limit on bandwidth in the matched termination case the area goes to zero when the velocities are matched, resulting in an infinite bandwidth.

We now have observed three separate closed form analytical models for TWPD devices. We have derived a relationship relating microwave bandwidth to velocity mismatch between the microwave and optical signals. This first order relationship suggests that velocity matching will have very little effect on the device bandwidth. In fact, the approximate expression given by (2-37) suggests that there is no relationship between bandwidth and velocity matching. The velocity mismatch bandwidth expression is used to estimate the bandwidth in Chapter 4. However, the accuracy of all these models is questionable, since there have been several simplifications made to obtain the expressions presented above.

Chapter 3 Numerical Analysis Using Method of Lines (MoL)

Chapter 2 illustrated several analytical models for the TWPD. However, in order to accurately and realistically describe the TWPD a full wave vectorial analysis of the optical fields, propagation constants and phase velocities is required. This can be achieved by using the Method of Lines (MoL). This chapter will introduce the Method of Lines (MoL) to the work on TWPDs. It will start with an introduction to the MoL outlining its previous uses and its similarities with other numerical methods (i.e. Finite-Difference Method FDM and Moment Method MoM). The advantages and drawbacks of using the MoL will be presented, as well as the reason for using the MoL over other numerical methods and over commercially available CAD tools. This is followed by a MoL formulation for isotropic inhomogeneous lossy waveguiding structures inspired by Berini et al[83]. The validation to the MoL derivation is compared against two lossless rib structures and a lossy Schottky contact TWPD whose results are reported in the scientific literature.

3.1 Introduction to the Method of Lines

The method of lines was originally developed by mathematicians in order to solve partial differential equations (PDEs)[52-53]. In the early 1980s it was introduced into the microwave numerical community by Pregla[54] et al to solve microwave waveguiding problems. It has since been expanded to solve a host of microwave and optical structures[55-83]. It is considered a semi-analytical or semi-numerical approach in solving PDEs. This is due to the use of a finite difference operator (i.e. numerical approximation to differential operator) to convert a PDE into an ODE. Unlike the Finite difference method (FDM) where all the differential operators are replaced with a finite difference operators, the MoL stops at the N-1 dimension. That is, if there are four differential operators in the PDE, three of them will be replaced with a finite difference operator, thus converting the PDE into an ODE. The solution to this ODE is then found

analytically by matching the fields at some interface layer. The method generates a complex analytic function whose roots are the propagation constants ($\gamma = \alpha + j\beta$) of the mode supported by the structure.

3.1.1 Heuristic Description of the Method of Lines

All numerical methods can be classified under three domains: finite difference method (FDM), finite element method (FEM) or moment methods (MoM). Figure 3.1 shows the numerical triangle classifying the three main methods of numerical modeling. Hybrid methods, such as the MoL, fall between the numerical triangular, in this case, between the FDM and MoM. The MoL has certain similarities with the FDM due to its use of the difference operator in replacing the differential operator in the PDE. However, it differs from FDM in that not all differential operators are replaced with finite difference operators. By doing this an analytical expression can be derived and solved. Due to this property this makes the solution to the PDE intrinsically more accurate than FDM or FEM techniques. It also possesses certain similarities with the Moment Method (MoM) or mode matching methods since transformations are applied to the finite difference matrix and the fields are matched to satisfy the continuity condition. Unlike the MoM, no global approximation to the fields using basis function expansion is done, hence, convergence issues that may arise as a result of truncation of the summation of the basis functions is avoided.

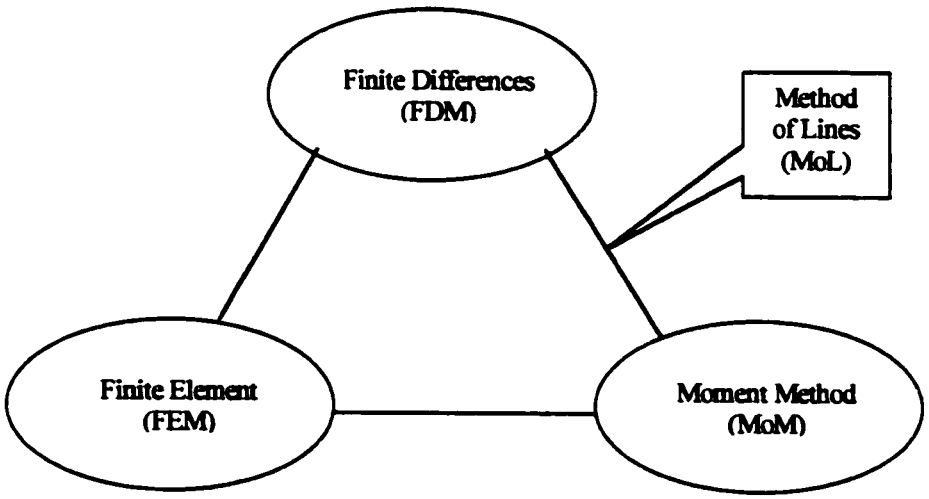

Figure 3.1 Numerical method classification

The advantages of using the MoL over other numerical methods such as FDM and MoM are:

- Increased accuracy due to a reduction in discretization error. The difference operator is only applied to N-1 dimensions instead of N dimensions as in the FDM case.
- Less computation time but more preprocessing in the form of analytical formulation is required.
- Convergence is always assured. Unlike MoM or other orthogonal basis function expansion methods where truncation of the series may lead to convergence problems, the MoL possesses no convergence problems since the fields are not approximated by basis functions.
- It is a full wave vectorial method and does not use any approximation to reduce the fields to equivalent scalar components.
- All six field components can be determined.
- Monotonic convergence of the propagation constant with decreasing line spacing allows extrapolation to more accurate values.

The disadvantages of using the MoL over other methods are:

- The resulting equation in the complex domain may be difficult to solve for roots.
- Often the propagation constant found must be compared directly against the field distribution to ensure the correct and desired mode has been calculated.
- The modal matrix $G_{e,h}$ which generates the indirect eigenvalue problem (i.e. $det[G_{e,h}(\gamma)]$) may become numerically unstable (i.e. singular) as the $det[G_{e,h}(\gamma)]$ converges to the eigenvalue.
- The analytical preprocessing causes the formulation to be tailored to specific classes of structures.

The MoL holds certain key advantages in being able to accurately, quickly, and fully describe the modes propagating in the waveguide. This method has the ability to accurately model the metallization, something that is required when designing a TWPD. To the author's knowledge accurate characterization of the metal at optical frequencies has not been done in commercially available CAD tools. All six field components can be generated which gives a designer a complete and accurate picture of the mode(s). This too is an ability that seems to be lacking in commercial CAD tools. Thus, due to the above advantages the MoL was chosen over other numerical routines and commercially available CAD tools.

3.1.2 Method of Lines Formulation Algorithm

The previous section argued that the MoL was chosen because it is a rigorous, accurate full wave vectorial approach for determining the propagation constant (i.e $\gamma=\alpha+j\beta$) of a waveguide. The algorithm described below is followed to formulate the MoL.

I. Using Maxwell's equations one formulates two uncoupled wave equations.

II. Using the uncoupled wave equations along with Maxwell's equations, one derives expressions for the other four field components.

III. Partition the 2-D computational domain along the x axis as shown in Figure 3.2 using two shifted lines system for the E and H fields respectively.

IV. Replace the first and second order partial differential operators $\partial/\partial x$ and $\partial^2/\partial x^2$ in wave equation formulated in step I, with D and P, the first and second order finite difference operators. Include the appropriate lateral boundary conditions in the difference operators. (i.e. ew–ew, ew-mw, mw-mw, mw–ew). ew-electrical wall and mw-magnetic wall.

V. The discretized wave equations are diagonalized using appropriate transformations matrices $U_{e,h}$ such that $U^{-1}_{e,h} P_{e,h} U_{e,h} = [\gamma_{e,h}^2]$, where $[\gamma_{e,h}^2]$, $U_{e,h}$ represents the eigenvalues and eigenvectors respectively for the tri-diagonal second order finite difference matrix $P_{e,h}$.

VI. The diagonalization procedure now yields two systems of uncoupled 1-D second order ordinary differential equations (telegrapher's equations) along the remaining dimension.

VII. The second order ordinary differential telegrapher's equations are solved analytically.

VIII. Impedance or admittance type relationships are generated.

IX. Using the impedance or admittance relationships the matching of tangential field components is enforced at each interface between layers starting from the top and bottom boundary.

X. The last field matching conditions are applied near the center of the structure. This yields the modal function $G(\gamma)e_{a,b}$ or $G(\gamma)h_{a,b} = 0$ which operate on the transformed tangential fields.

XI. The complex propagation constant γ is then extracted from $G_{eh}(\gamma)$ by searching for values that satisfy $det[G_{eh}(\gamma)] = 0$. This is known as the indirect eigenvalue problem.

XII. Once the propagation constant has been determined, the field distribution can be obtained at the matching interface via singular value decomposition to the modal function $G_{eh}(\gamma)$.

XIII. The distribution of all six field components over the entire computational domain is found by applying the analytical solution.

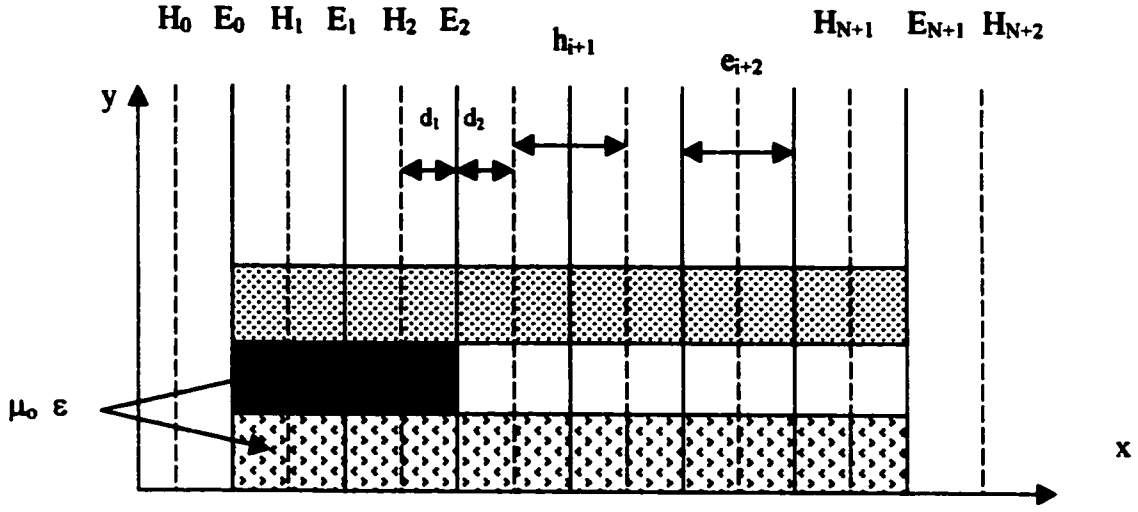

Figure 3.2 Arbitrary waveguide structure

3.2 Formulation for Isotropic Inhomogeneous Lossy Structures

The formulation presented here will follow the algorithm presented in the last section. This will be done for an inhomogeneous lossy isotropic waveguiding structure. The waveguiding structures of interest in this thesis are uniform in the propagation direction $\pm z$. The computational domain is discretized along one dimension only, the x axis, and the analytical solution is applied along y. The method is kept quite general and once the formulation is complete the method will have the ability to characterize most microwave and optical waveguiding structures.

3.2.1 Formulation of Uncoupled Wave Equations

We start with the formulation of two uncoupled wave equations for E^{TE} and H^{TM} from Maxwell's equations. The structures that shall be considered in this thesis are inhomogeneous lossy isotropic waveguiding structures such as dielectric waveguides, rib waveguides, microstrip and coplanar waveguides. These problems can be rigorously described mathematically by the vector wave equations.

The formulation begins with Maxwell's equations written in the frequency domain for a source free lossy isotropic media.

$$\nabla \times H = j\omega\varepsilon E \tag{3-1a}$$

$$\nabla \times E = -j\omega\mu H \tag{3-1b}$$

$$\nabla \cdot \varepsilon E = 0 \tag{3-1c}$$

$$\nabla \cdot \mu H = 0 \tag{3-1d}$$

Where ε, μ is the permittivity and permeability of the material respectively. The material structure considered here is a non-magnetic material hence, $\mu = \mu_o$, which is the permeability of free space given as $4\pi \times 10^{-7}$ F/m. Both the dielectric and ohmic losses can be included in the permittivity by using the following relationship: $\varepsilon = \varepsilon' - j(\varepsilon'' - \sigma/\omega)$. Where the ε'' represents losses due to the dielectric and σ represent the conductivity of the system.

Figure 3.2 shows line discretization for an arbitrary inhomogeneous structure applied along the x direction. With this discretization in mind, the permittivity is redefined as a complex function of x expressed as $\varepsilon(x) = \varepsilon'(x) - j[\varepsilon''(x) + \sigma(x)/\omega]$. The complex refractive index is related to the permittivity via the following well known relationship: $n^2(x) = \varepsilon_r(x)$ where $\varepsilon_r(x) = \varepsilon(x)/\varepsilon_o$. Unlike the FDM method where the refractive index would also contain a y dependence term, this has been removed in the MoL since the inhomogeneous structure is divided into a number of homogeneous layers with boundary conditions applied between them.

Maxwell's equation (3-1a)–(3-1d) represents first order coupled PDEs, which become uncoupled second order PDEs by applying the curl operator ($\nabla\times$) to (3-1a) and (3-1b) and performing the appropriate algebraic manipulation:

$$\nabla \times \nabla \times E - \omega^2 \mu\varepsilon E = 0 \tag{3-2a}$$

$$\nabla \times \varepsilon^{-1} \nabla \times H - \omega^2 \mu H = 0 \tag{3-2b}$$

The two vectorial wave equations (3-2a) and (3-2b) are expanded into six scalar wave equations, some of which are coupled by inhomogeneity in the permittivity, $\varepsilon(x)$. By writing these equations for TE^z ($E_x^{TE} = 0$) and TM^z ($H_x^{TM} = 0$) modes and making use of $\nabla \cdot (\varepsilon E) = 0$ and $\nabla \cdot H = 0$ accordingly, we obtain six uncoupled scalar wave equations. The TE^z modes must satisfy the following Helmholtz wave equation for the E_y^{TE} field component:

$$\frac{\partial^2}{\partial x^2} E_y^{TE} + \frac{\partial^2}{\partial y^2} E_y^{TE} + (\gamma^2 + \omega^2 \mu \varepsilon) E_y^{TE} = 0 \tag{3-3}$$

and similarly, the TM^z modes must satisfy the following Sturm-Liouville wave equation for the H_y^{TM} field component:

$$\varepsilon \frac{\partial}{\partial x}\left[\frac{1}{\varepsilon}\frac{\partial}{\partial x} H_y^{TM}\right] + \frac{\partial^2}{\partial y^2} H_y^{TM} + (\gamma^2 + \omega^2 \mu \varepsilon) H_y^{TM} = 0 \tag{3-4}$$

3.2.2 Expression for Field Components

The next step in the algorithm is to formulate an expression for the other field components. This is done by expanding equations (3-1a) and (3-1b). The propagation direction is taken to be in the $+z$ direction, thus we can infer the following, $\partial/\partial z = -\gamma$ and $\gamma = \alpha + j\beta$. We know that in a linear medium the superposition of the TE^z and TM^z modes fully characterizes all modes propagating in the structure, including hybrid and higher order modes. The electric and magnetic field components of the mode fields propagating in the structure are related to the TE^z and TM^z mode fields via the following relationships:

$$E_x = \frac{-1}{j\omega\gamma}\left[\frac{\partial}{\partial x}\left(\frac{1}{\varepsilon}\frac{\partial}{\partial x} H_y^{TM}\right) + \omega^2 \mu H_y^{TM}\right] \tag{3-5a}$$

$$E_y = E_y^{TE} - \frac{1}{j\omega\gamma\varepsilon}\frac{\partial^2}{\partial x \partial y} H_y^{TM} \tag{3-5b}$$

$$E_z = \frac{1}{\gamma}\frac{\partial}{\partial y} E_y^{TE} + \frac{1}{j\omega\varepsilon}\frac{\partial}{\partial x} H_y^{TM} \tag{3-5c}$$

$$H_x = \frac{1}{j\omega\gamma}\left[\frac{1}{\mu}\frac{\partial^2}{\partial x^2} E_y^{TE} + \omega^2 \varepsilon E_y^{TE}\right] \tag{3-5d}$$

$$H_y = \frac{1}{j\omega\gamma\mu}\frac{\partial}{\partial x \partial y} E_y^{TE} + H_y^{TM} \tag{3-5e}$$

$$H_z = \frac{-1}{j\omega\mu}\frac{\partial}{\partial x} E_y^{TE} + \frac{1}{\gamma}\frac{\partial}{\partial y} H_y^{TM} \tag{3-5f}$$

Thus, the Helmholtz and Sturm-Liouville wave equations (3-3) and (3-4) along with equations (3-5a)-(3-5f) completely characterize all modes that propagate in a lossy isotropic inhomogeneous 2-D waveguide where no structural variation exists in the propagation direction z. These equations can be solved consistently for the propagation constant γ using the appropriate Dirichlet and Neumann boundary conditions applied to both the vertical and horizontal limits.

3.2.3 Discretization of the Computational Domain

Following the algorithm presented in Section 3.1.2 the computational domain is discretized only along one dimension for a 2-D problem. Figure 3.2 illustrates an arbitrary waveguide structure composed of a sequence of layers that are homogeneous or inhomogeneous in the x direction. Shown are the two shifted E and H line systems where the E_y^{TE} and H_y^{TM} field components are solved respectively. The structures that are presented and analyzed in this thesis are all considered to be open structures, hence the enclosing boundary conditions, which are applied in the difference operators, must be placed sufficiently far away

from the fields, such that they do not perturb the mode(s). However, at the same time we must ensure that the line discretization is fine enough to accurately characterize the modes in the region of interest. While this can be done with an equidistant line discretization, the result is a significant increase in the number of lines required to model the structure. This translates directly into an increase in computational time. Another approach is use a non-equidistant line discretization, but one must be sure that the discretization is fine enough to model the fields, in the region of interest, where they may vary quickly with position.

The solution to this trade off is to use both the equidistant and non-equidistant line discretizations. In order to accurately model the fields in the region of interest an equidistant line discretization is adopted. This will satisfy the condition that any rapidly changing field components are accurately and fully characterized. In order to meet the second criteria of placing the lateral enclosing boundary conditions far enough away as to not affect the mode profile, a non-equidistant line discretization is implemented. This hybrid discretization scheme will ensure that the structure is characterized fully and accurately without affecting the mode profile or significantly increasing the computational time.

A geometric progression is used to generate the non-equidistant discretization between successive E and H line systems in the computational domain. A constant expansion ratio is kept between successive lines such that the line systems do not become too coarse, too quickly. These conditions will cause the non-equidistant MoL to converge with h_{min} in essentially the same way as in the equidistant case. Using the following well-known relationship for geometric progression, the non-equidistant line discretization is implemented in half of the computational domain.

$$d = \frac{h_{min}(1-r^N)}{(1-r)} \tag{3-6}$$

where r is called the expansion parameter and is between $1 < r \leq 1.5$

N is the number of lines entered by the user

h_{min} is the minimum discretization interval

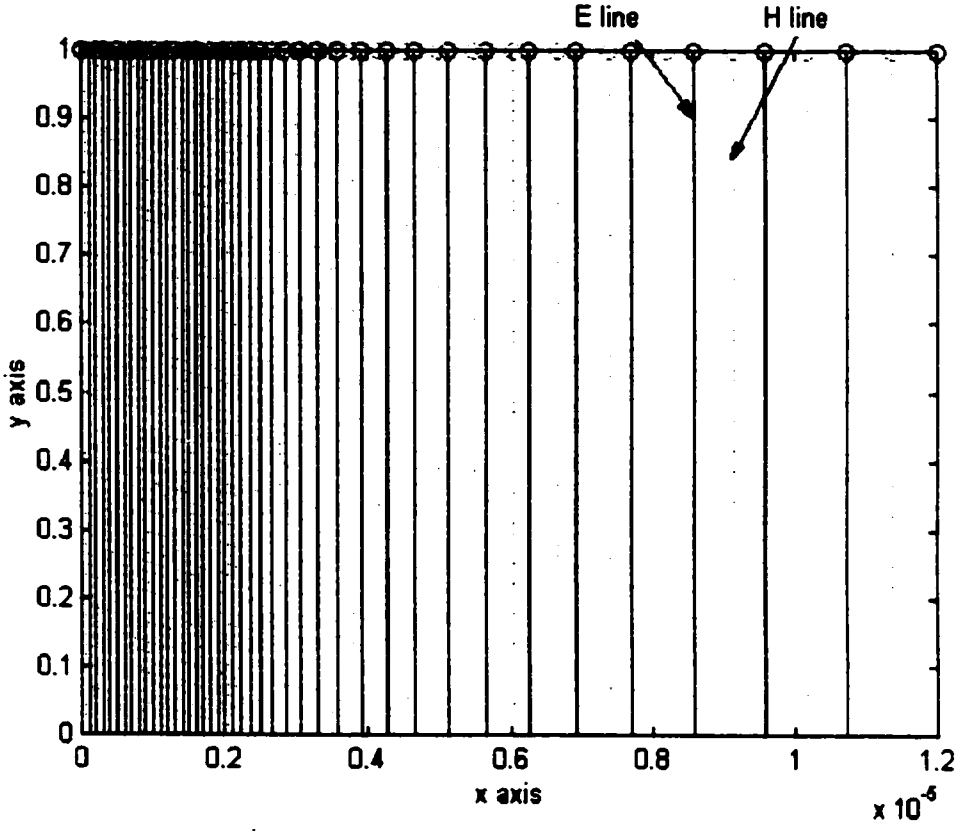

Figure 3.3 Line discretization for electric wall electric wall boundary conditions.

Figure 3.3 shows the results of using the hybrid discretization for two shifted *E* and *H* line systems. The discretization program generates the *E* and *H* lines systems given the number of lines entered by the user, and the width of the inhomogeneous section *w*. The program generates an equidistant mesh $2w$ away from the rib and a non-equidistant line meshing $10w$ away from the equidistant section, therefore the entire computational domain is $12w$. The case shown in Figure 3.3 is for an optical rib waveguide shown in Figure 3.5 presented in the validation section. The width of the rib is $w = 2.0\mu m$. Symmetry is employed thus only half the structure is analyzed. Hence $w = w/2 = 1.0\mu m$, therefore the uniform meshing has a total

spacing in the computational domain of $2.0\mu m$, while the non-uniform meshing has a spacing of $10\mu m$. The result is a total computational domain of 12 μm.

In the validation section it will be shown that by placing the enclosing lateral boundary condition $10w$ away from the computational area of interest, in this case the optical rib, the lateral boundary conditions do not affect the mode profile. With this method one does not require the use of absorbing boundary conditions to accurately model an open waveguiding structure.

3.2.4 Replacing Differential Operators with Finite Difference Operators

We must now replace the differential operators in (3-3), (3-4) and (3-5a) – (3-5f) with finite difference operators. The following relationships given below are first and second order finite difference operators for all combinations of lateral boundary conditions. The upper notation is for ew-ew or ew-mw lateral boundary conditions, while the lower notation represents mw-mw or mw-ew lateral boundary conditions.

First order finite differences operator are given by:

$$\frac{\partial}{\partial x}E_y^{n,TE} = \begin{Bmatrix} \frac{1}{h_{min}}D_x = \frac{1}{h_{min}}r_h Dr_e \\ -\frac{1}{h_{min}}D'_x = -\frac{1}{h_{min}}r_h Dr_e \end{Bmatrix} E_y^{n,TE} \qquad \textbf{(3-7a)}$$

$$\frac{\partial}{\partial x}H_y^{n,TM} = \begin{Bmatrix} -\frac{1}{h_{min}}D'_x = \frac{1}{h_{min}}r_e Dr_h \\ \frac{1}{h_{min}}D_x = -\frac{1}{h_{min}}r_e Dr_h \end{Bmatrix} H_y^{n,TM} \qquad \textbf{(3-7b)}$$

While the second order finite difference operators are given by the following relationships:

$$\frac{\partial^2}{\partial x^2} E_y^{n,TE} = -\frac{1}{h^2_{\min}} P_e = \left\{ \begin{matrix} -\frac{1}{h^2_{\min}} D^t{}_x D_x \\ -\frac{1}{h^2_{\min}} D_x D^t{}_x \end{matrix} \right\} E_y^{n,TE} \qquad \textbf{(3-7c)}$$

$$\frac{\partial}{\partial x}\left(\varepsilon^{-1} \frac{\partial}{\partial x} H_y^{n,TM} \right) = -\frac{1}{h^2_{\min}} P_{sh} = \left\{ \begin{matrix} -\frac{1}{h^2_{\min}} D_x [\varepsilon]^{-1}_e D^t{}_x \\ -\frac{1}{h^2_{\min}} D^t{}_x [\varepsilon]^{-1}_e D^t{}_x \end{matrix} \right\} H_y^{n,TM} \qquad \textbf{(3-7d)}$$

Where D is the finite difference matrix given by

$$D = \begin{bmatrix} 1 & & & & & \\ -1 & 1 & & & & \\ & -1 & 1 & & & \\ & & \cdot & \cdot & & \\ & & & \cdot & \cdot & \\ & & & & \cdot & \cdot \\ & & & & -1 & 1 \end{bmatrix}_{(N+1)(N)} \qquad \textbf{(3-8a)}$$

or

$$D=\begin{bmatrix} 1 & -1 & & & & \\ & 1 & -1 & & \mathbf{0} & \\ & & 1 & \ddots & & \\ & & & \ddots & \ddots & \\ & \mathbf{0} & & & \ddots & -1 \\ & & & & & 1 \end{bmatrix}_{(N)(N)} \qquad \textbf{(3-8b)}$$

The D matrix given in (3-8a) is the finite difference operator for the ew-ew or mw-mw boundary condition, while the D matrix given in (3-8b) is the difference operator for ew-mw or mw-ew boundary condition. The dimension of the matrix represents the number of E and H lines discretized in the computational domain.

The normalized fields $E_y^{n,TE}$ and $H_y^{n,TM}$ are defined such that the second order finite difference operators $P_{e,h}$ and P_{sh} are real tri-diagonal matrices. The normalized fields $E_y^{n,TE}$ and $H_y^{n,TM}$ quantities are related to the discretized fields E_y^{TE} and H_y^{TM} via the following matrix relationships:

$$\begin{aligned} E_y^{TE} &= r_e E_y^{n,TE} \\ \frac{\partial}{\partial x} E_y^{TE} &= r_h \frac{\partial}{\partial x} E_y^{n,TE} \\ \frac{\partial^2}{\partial x^2} E_y^{TE} &= r_e \frac{\partial^2}{\partial x} E_y^{n,TE} \end{aligned} \qquad \textbf{(3-9)}$$

and

$$
\begin{aligned}
H_y^{TM} &= r_h H_y^{n,TM} \\
\frac{\partial}{\partial x} H_y^{TM} &= r_e \frac{\partial}{\partial x} H_y^{n,TM} \\
\frac{\partial^2}{\partial x^2} H_y^{TM} &= r_e \frac{\partial^2}{\partial x} H_y^{n,TM}
\end{aligned}
\tag{3-10}
$$

where the normalization matrices r_e and r_h are given by:

$$
r_e = \left[\sqrt{\frac{h_{\min}}{e_i}} \right] \qquad r_h = \left[\sqrt{\frac{h_{\min}}{h_i}} \right] \tag{3-11}
$$

The spacing h_{min} represents the minimum spacing between the equidistant lines and e_i and h_i are the spacing between non-equidistant lines.

Substituting the difference operators given in (3-7a)-(3-7d) and the normalized fields given in (3-9) and (3-10) into the Helmholtz and Sturm-Liouville equations (3-3) and (3-4), we obtain the following expressions:

$$
\frac{d^2 E_y^{n,TE}}{dy^2} (\gamma^2 + \omega^2 \mu [\varepsilon]_e - \frac{1}{h^2_{\min}} P_e) E_y^{n,TE} = 0 \tag{3-12}
$$

$$
\frac{d^2 H_y^{n,TM}}{dy^2} + (\gamma^2 + \omega^2 \mu [\varepsilon]_h - \frac{1}{h^2_{\min}} [\varepsilon_h] P_{sh_h}) H_y^{n,TM} = 0 \tag{3-13}
$$

Our wave equations are now ordinary differential wave equations that are discretized within each layer. The diagonal matrices $[\varepsilon]_e$, $[\varepsilon]_h$ are created from the function $\varepsilon(x)$ sampled on the E and H line systems

respectively. The discontinuities in permittivity can be rigorously accounted for if they are placed on an E line that satisfies the edge condition. This is because the tangential electric E_y field components are continuous across the interface. Referring to Figure 3.2 we observe the value of the permittivity at the discontinuity can be accounted for by using the following relationship:

$$\varepsilon_r = \frac{\varepsilon_{r1} d_1 + \varepsilon_{r2} d_2}{d_1 + d_2} \tag{3-14}$$

where ε_{r1} and ε_{r2} are the relative permittivities in the respective media and d_1 and d_2 are the line spacing values. We observed that the permittivity at the discontinuity is modeled as a weighted average for non-equidistant line spacing. If the spacing is equidistant (i.e. $d_1 = d_2$) the weighted average becomes a true average and equation (3-14) becomes

$$\varepsilon_r = \frac{\varepsilon_{r1} + \varepsilon_{r2}}{2} \tag{3-15}$$

This is the average of the permittivities of the two medium. It should be noted that while this was considered in the MoL program and coded for this thesis, it is not necessary for determining the propagation constant, gamma (γ) of the mode.

3.2.5 Applying the Transformation Matrices

From the discretized Helmholtz (3-12) and Sturm-Liouville (3-13) wave equations we introduce the following transformations matrices:

$$\begin{aligned} E_y^{n,TE} &= U_e \Phi_y^{TE} \\ H_y^{n,TM} &= U_h \Phi_y^{TM} \end{aligned} \tag{3-16}$$

where U_e and U_h are nonsingular matrices. These transformations in (3-16) are applied to the discretized wave equations and then multiplied by $U^{-1}{}_e$ and $U^{-1}{}_h$, respectively which yield:

$$\frac{d^2\Phi_y^{TE}}{dy^2} - \underbrace{U^{-1}{}_e(\overbrace{\frac{1}{h^2{}_{min}}P_e - \gamma^2 - \omega^2\mu[\varepsilon]_e}^{M})U_e}_{\gamma^2{}_e}\Phi_y^{TE} = 0 \qquad (3\text{-}17)$$

$$\frac{d^2\Phi_y^{TM}}{dy^2} - \underbrace{U^{-1}{}_h(\overbrace{\frac{1}{h^2{}_{min}}[\varepsilon]_h P_{sh} - \gamma^2 - \omega^2\mu[\varepsilon]_h}^{N})U_h}_{\gamma^2{}_h}\Phi_y^{TM} = 0 \qquad (3\text{-}18)$$

Equation (3-17) represents the transformed Helmholtz equation and (3-18) represents the transformed Sturm-Liouville equation. The transformation matrices U_e and U_h are selected such that the tridiagonal matrices M and N are diagonalized. This is accomplished numerically via eigenvalue decomposition where the transformation matrices U_e ,U_h and the diagonal matrices $[\gamma^2{}_e]$, $[\gamma^2{}_h]$ represent the orthonormal eigenvectors and eigenvalues of M and N respectively.

From (3-17) and (3-18) a few observations can be made. First, if a layer is homogeneous, then the transformation matrices U_e and U_h become identical to the orthonormal transformation matrices T_e and T_h given in the homogeneous case[84]. Therefore, γ can be factored out of the transform equations (3-17) and (3-18) and as a result the transformation matrices T_e and T_h do not need to be recomputed for each homogeneous layer. In the inhomogeneous isotropic layer however, this cannot be done and the transformation matrices U_e, U_h and the eigenvalues $[\gamma^2{}_e]$, $[\gamma^2{}_h]$ must be recomputed for each new layer in this scenario. Lastly, if the structure is lossless then the second order tri-diagonal finite difference matrix is real and sign-symmetric hence the eigenvalues and eigenvectors generated will be real.

Following the algorithm presented in section 3.1.2 we have now completed steps V and VI. In summary, we have just applied the transformation matrix to the discretized wave equation. This yields two uncoupled second order differential equations (3-17)-(3-18). The solution of these is described in the next section.

3.2.6 Analytical Solution to Telegrapher's Equation

The transformation matrix used to diagonalized the discretized Helmholtz and Sturm-Liouville equations yields the telegrapher's equations (3-17) and (3-18) for which the solution is well known and expressed vectorially below as:

$$\begin{bmatrix} \dfrac{d\Phi_y^{TE,TM}(y_a)}{dy} \\ \dfrac{d\Phi_y^{TE,TM}(y_b)}{dy} \end{bmatrix} = \gamma_{e,h} \begin{bmatrix} -[\tanh(\gamma_{e,h}d)]^{-1} & [\sinh(\gamma_{e,h}d)]^{-1} \\ -[\sinh(\gamma_{e,h}d)]^{-1} & [\tanh(\gamma_{e,h}d)]^{-1} \end{bmatrix} \begin{bmatrix} \Phi_y^{TE,TM}(y_a) \\ \Phi_y^{TE,TM}(y_b) \end{bmatrix} \qquad (3\text{-}19)$$

Electric wall or magnetic wall boundary conditions for layer N (superstrate)

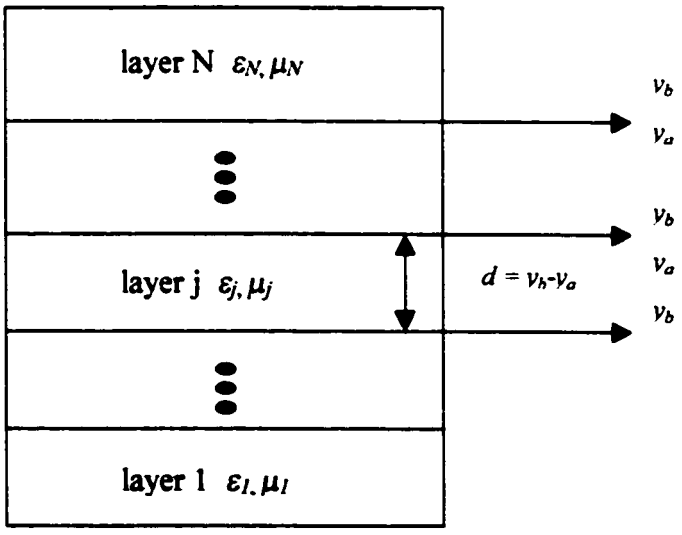

Electric wall or magnetic wall boundary conditions for layer 1 (substrate)

Figure 3.4 Multi-layer structure having arbitrary top and bottom boundary conditions

Equation (3-19) holds for any layer in the structure of interest. The parameter d represents the thickness of a layer as illustrated in Figure 3.4 and given by $d = y_a - y_b$. Where y_b refers to the position just under the top interface and y_a the position slightly above the bottom interface, hence all quantities are within layer j. Since the eigenvalues $[\gamma_e^2]$ and $[\gamma_h^2]$ obtained through the diagonalization process are diagonal matrices, this implies that the submatrices $[cosh(\gamma_{e,h}d)]$, $[sinh(\gamma_{e,h}d)]$ and $[tanh(\gamma_{e,h}d)]$ are also diagonal matrices.

3.2.7 Formulation of Impedance and Admittance Relationships

Using the other four field components, E_x, E_z, H_x, and H_z, given by (3-5a), (3-5c), (3-5d), (3-5f) respectively, we generate impedance or admittance type relationships. We start this process by introducing the following transformations:

$$\begin{aligned}
\tilde{e}_x &= T_h^t r^{-1}{}_h E_x = T_h^t E_x^n \\
\tilde{e}_z &= T_e^t r^{-1}{}_e E_z = T_e^t E_z^n \\
\tilde{h}_x &= T_e^t r^{-1}{}_e H_x = T_e^t H_x^n \\
\tilde{h}_z &= T_h^t r^{-1}{}_h H_z = T_h^t H_z^n
\end{aligned} \tag{3-20}$$

Substituting the appropriate finite difference operators defined in equations (3-7a)-(3-7d), the above relationship (3-20), and the transformation matrix (3-16) into (3-5a)-(3-5c) and (3-5d)-(3-5f), yields a matrix relationship between the transformed tangential fields, $\Phi_y^{TE,TM}$, and $d\Phi_y^{TE,TM}/dy$:

$$\begin{bmatrix} \tilde{e}_z \\ \tilde{e}_x \\ \tilde{h}_x \\ \tilde{h}_z \end{bmatrix} = \begin{bmatrix} \frac{1}{j}Q_{11} & \frac{1}{\gamma}Q_{12} & 0 & 0 \\ \frac{1}{j\gamma}Q_{21} & 0 & 0 & 0 \\ 0 & 0 & 0 & \frac{1}{j\gamma}Q_{34} \\ 0 & 0 & \frac{1}{\gamma}Q_{43} & \frac{1}{j}Q_{44} \end{bmatrix} \begin{bmatrix} \Phi_y^{TM} \\ \frac{d\Phi_y^{TE}}{dy} \\ \frac{d\Phi_y^{TM}}{dy} \\ \Phi_y^{TE} \end{bmatrix} \tag{3-21}$$

The submatrices Q_{ij} are given below for all combinations of lateral boundary conditions. With the top notation representing ew-ew or ew-mw lateral boundary conditions and the bottom notation representing mw-mw or mw-ew lateral boundary conditions.

$$Q_{11} = \begin{cases} \dfrac{-1}{\omega h_{\min}} T'_e [\varepsilon_e]^{-1} D'_x U_h \\ \dfrac{1}{\omega h_{\min}} T'_e [\varepsilon_e]^{-1} D_x U_h \end{cases} \tag{3-22}$$

$$Q_{12} = T'_e U_e \tag{3-23}$$

$$Q_{21} = \begin{cases} \dfrac{1}{\omega h^2_{\min}} T_h' D_x [\varepsilon_e]^{-1} D'_x U_h - \omega\mu T_h' U_h \\ \dfrac{1}{\omega h^2_{\min}} T_h' D'_x [\varepsilon_e]^{-1} D_x U_h - \omega\mu T_h' U_h \end{cases} \tag{3-24}$$

$$Q_{34} = \begin{cases} -\dfrac{1}{\omega\mu_o h^2_{\min}} T_e' D_x D'_x U_e + \omega T_e' [\varepsilon]_z U_e \\ -\dfrac{1}{\omega\mu_o h^2_{\min}} T_e' D_x D'_x U_e + \omega T_e' [\varepsilon]_z U_e \end{cases} \tag{3-25}$$

$$Q_{43} = T'_h U_h \tag{3-26}$$

$$Q_{44} = \begin{cases} \dfrac{-1}{\omega h_{\min}} T'_h D_x U_e \\ \dfrac{1}{\omega h_{\min}} T'_h D'_x U_e \end{cases} \tag{3-27}$$

If the layer is homogeneous the submatrices Q_{ij} simplify to the following relationships:

$$Q_{11} = \begin{cases} \dfrac{-1}{\omega\varepsilon h_{\min}} T'_e D'_x T_h = -\dfrac{1}{\omega\varepsilon h_{\min}} \delta' \\ \dfrac{1}{\omega\varepsilon h_{\min}} T'_e D_x T_h = \dfrac{1}{\omega\varepsilon h_{\min}} \delta \end{cases} \tag{3-28}$$

$$Q_{12} = T'_e T_e = I \tag{3-29}$$

$$Q_{21} = \frac{1}{\omega\varepsilon h^2_{\min}}\left[\lambda^2{}_h\right] - \omega\mu I \tag{3-30}$$

$$Q_{34} = -\frac{1}{\omega\varepsilon h^2_{\min}}\left[\lambda^2{}_e\right] - \omega\mu I \tag{3-31}$$

$$Q_{11} = \begin{cases} \dfrac{-1}{\omega\mu h_{\min}} T^t{}_h D_x T_e = -\dfrac{1}{\omega\mu h_{\min}}\delta \\ \dfrac{1}{\omega\mu h_{\min}} T^t{}_h D^t{}_x T_e = \dfrac{1}{\omega\mu h_{\min}}\delta^t \end{cases} \tag{3-32}$$

The matrix δ is given by:

$$\delta = T^t{}_h D_x T_e = \begin{bmatrix} 0 & & & & \\ \lambda_{e,1} & 0 & & & \\ & \lambda_{e,1} & & 0 & \\ & & & & \\ & 0 & & & \\ & & & \lambda_{e,N} & 0 \end{bmatrix}_{(N+1)(N)} \tag{3-33}$$

for ew-ew or mw-mw lateral boundary conditions and is given by:

$$\delta = T^t{}_h D_x T_e = \begin{bmatrix} \lambda_{e,1} & & & \\ & \lambda_{e,1} & & 0 \\ & & \ddots & \\ & 0 & & \\ & & & \lambda_{e,N} \end{bmatrix}_{(N)(N)} \tag{3-34}$$

for the ew-mw or mw-ew boundary conditions. The first order finite difference operator D_x changes depending on the lateral boundary condition as given by (3-8a) and (3-8b) and I represents the identity matrix. The values of $\lambda_{x,i}$ are given by [84].

Equation (3-21) holds for any vertical position within a layer. We can eliminate $\Phi_y^{TE,TM}$ and $d\Phi_y^{TE,TM}/dy$ by combining equation (3-21) with equation (3-19). Thus, we obtain the following matrix relationships between the transformed tangential fields at the top and bottom of layer j.

$$\begin{bmatrix} \tilde{e}_z(y_a) \\ \tilde{e}_z(y_b) \end{bmatrix} = \gamma Q_{11} Q^{-1}{}_{21} \begin{bmatrix} \tilde{e}_z(y_a) \\ \tilde{e}_z(y_b) \end{bmatrix} + jQ_{12}[\gamma_e] \begin{bmatrix} -[\tanh(\gamma_e d)]^{-1} & [\sinh(\gamma_e d)]^{-1} \\ -[\sinh(\gamma_e d)]^{-1} & [\tanh(\gamma_e d)]^{-1} \end{bmatrix} Q^{-1}{}_{34} \begin{bmatrix} \tilde{h}_x(y_a) \\ \tilde{h}_x(y_b) \end{bmatrix} \quad \textbf{(3-35)}$$

$$\begin{bmatrix} \tilde{h}_z(y_a) \\ \tilde{h}_z(y_b) \end{bmatrix} = jQ_{43}[\gamma_h] \begin{bmatrix} -[\tanh(\gamma_e d)]^{-1} & [\sinh(\gamma_e d)]^{-1} \\ -[\sinh(\gamma_e d)]^{-1} & [\tanh(\gamma_e d)]^{-1} \end{bmatrix} Q_{21}{}^{-1} \begin{bmatrix} \tilde{e}_x(y_a) \\ \tilde{e}_x(y_b) \end{bmatrix} + \gamma Q_{44} Q_{34}{}^{-1} \begin{bmatrix} \tilde{h}_x(y_a) \\ \tilde{h}_x(y_b) \end{bmatrix} \quad \textbf{(3-36)}$$

Equations (3-35) and (3-36) can be combined into an admittance relationship as shown below:

$$\begin{bmatrix} \tilde{h}_a \\ \tilde{h}_b \end{bmatrix} = \begin{bmatrix} y_1 & y_2 \\ y_2 & -y_1 \end{bmatrix} \begin{bmatrix} \tilde{e}_a \\ \tilde{e}_b \end{bmatrix} \quad \textbf{(3-37)}$$

where

$$\tilde{h}_{a,b} = \begin{bmatrix} \tilde{h}_z(y_{a,b}) \\ \tilde{h}_x(y_{a,b}) \end{bmatrix} \quad \textbf{(3-37a)}$$

$$\tilde{e}_{a,b} = \begin{bmatrix} \tilde{e}_z(y_{a,b}) \\ \tilde{e}_x(y_{a,b}) \end{bmatrix} \quad \textbf{(3-37b)}$$

and

$$y_1 = \begin{bmatrix} -y_{11} & y_{21} \\ y_{12} & -y_{22} \end{bmatrix} \qquad y_2 = \begin{bmatrix} -y_{13} & y_{14} \\ y_{23} & -y_{24} \end{bmatrix} \tag{3-38}$$

the submatricies y_{ij} are given by:

$$y_{11} = jQ_{43}[\gamma_h][\tanh(\gamma_h d)]^{-1}Q^{-1}{}_{21} + j\gamma^2 Q_{44}[\tanh(\gamma_e d)]^{-1}[\gamma_e]^{-1}Q^{-1}{}_{12}Q_{11}Q^{-1}{}_{21} \tag{3-38a}$$

$$y_{12} = j\gamma^2 Q_{44}[\tanh(\gamma_e d)]^{-1}[\gamma_e]^{-1}Q^{-1}{}_{12} \tag{3-38b}$$

$$y_{13} = jQ_{43}[\gamma_h][\sinh(\gamma_h d)]^{-1}Q^{-1}{}_{21} + j\gamma^2 Q_{44}[\sinh(\gamma_e d)]^{-1}[\gamma_e]^{-1}Q^{-1}{}_{12}Q_{11}Q^{-1}{}_{21} \tag{3-38c}$$

$$y_{14} = j\gamma Q_{44}[\sinh(\gamma_e d)]^{-1}[\gamma_e]^{-1}Q^{-1}{}_{12} \tag{3-38d}$$

$$y_{21} = \frac{\gamma}{j}Q_{34}[\tanh(\gamma_e d)]^{-1}[\gamma_e]^{-1}Q^{-1}{}_{12}Q_{11}Q^{-1}{}_{21} \tag{3-38e}$$

$$y_{22} = \frac{1}{j}Q_{34}[\tanh(\gamma_e d)]^{-1}[\gamma_e]^{-1}Q^{-1}{}_{12} \tag{3-38f}$$

$$y_{23} = \frac{\gamma}{j}Q_{34}[\sinh(\gamma_e d)]^{-1}[\gamma_e]^{-1}Q^{-1}{}_{12}Q_{11}Q^{-1}{}_{21} \tag{3-38g}$$

$$y_{24} = \frac{1}{j}Q_{34}[\sinh(\gamma_e d)]^{-1}[\gamma_e]^{-1}Q^{-1}{}_{12} \tag{3-38h}$$

Alternatively equations (3-35) and (3-36) can also be combined into an impedance relationship as shown below:

$$\begin{bmatrix} \tilde{e}_a \\ \tilde{e}_b \end{bmatrix} = \begin{bmatrix} z_1 & z_2 \\ z_2 & -z_1 \end{bmatrix} \begin{bmatrix} \tilde{h}_a \\ \tilde{h}_b \end{bmatrix} \tag{3-39}$$

where

$$\tilde{h}_{a,b} = \begin{bmatrix} \tilde{h}_z(y_{a,b}) \\ \tilde{h}_x(y_{a,b}) \end{bmatrix} \tag{3-39a}$$

and

$$\tilde{e}_{a,b} = \begin{bmatrix} \tilde{e}_z(y_{a,b}) \\ \tilde{e}_x(y_{a,b}) \end{bmatrix} \tag{3-39b}$$

$$z_1 = \begin{bmatrix} -z_{11} & z_{21} \\ z_{12} & -z_{22} \end{bmatrix} \qquad z_2 = \begin{bmatrix} -z_{13} & z_{14} \\ z_{23} & -z_{24} \end{bmatrix} \tag{3-40}$$

the submatricies z_{ij} are given by:

$$z_{11} = \frac{1}{j} Q_{21} [\tanh(\gamma_h d)]^{-1} [\gamma_h]^{-1} Q^{-1}{}_{43} \tag{3-40a}$$

$$z_{12} = \frac{\gamma}{j} Q_{21} [\tanh(\gamma_e d)]^{-1} [\gamma_h]^{-1} Q^{-1}{}_{43} Q_{44} Q^{-1}{}_{34} \tag{3-40b}$$

$$z_{13} = \frac{1}{j} Q_{21} [\sinh(\gamma_h d)]^{-1} [\gamma_h]^{-1} Q^{-1}{}_{43} \tag{3-40c}$$

$$z_{14} = \frac{\gamma}{j} Q_{21} [\sinh(\gamma_h d)]^{-1} [\gamma_h]^{-1} Q^{-1}{}_{43} Q_{44} Q^{-1}{}_{34} \tag{3-40d}$$

$$z_{21} = j\gamma Q_{11} [\tanh(\gamma_h d)]^{-1} [\gamma_h]^{-1} Q^{-1}{}_{43} \tag{3-40e}$$

$$z_{22} = jQ_{12} [\gamma_e] [\tanh(\gamma_e d)]^{-1} Q^{-1}{}_{34} + j\gamma^2 Q_{11} [\tanh(\gamma_h d)]^{-1} [\gamma_h]^{-1} Q^{-1}{}_{43} Q_{44} Q^{-1}{}_{34} \tag{3-40f}$$

$$z_{23} = j\gamma Q_{11} [\sinh(\gamma_h d)]^{-1} [\gamma_h]^{-1} Q^{-1}{}_{43} \tag{3-40g}$$

$$z_{24} = jQ_{12} [\gamma_e] [\sinh(\gamma_e d)]^{-1} Q^{-1}{}_{34} + j\gamma^2 Q_{11} [\sinh(\gamma_h d)]^{-1} [\gamma_h]^{-1} Q^{-1}{}_{43} Q_{44} Q^{-1}{}_{34} \tag{3-40h}$$

3.2.8 Formulation of the Modal Matrix $G_{e,h}(\gamma)$

Following the algorithm presented for the MoL we must now formulate the modal matrix $G_{e,h}(\gamma)$ in order to derive the indirect eigenvalue problem. Although the matching interface can be chosen to be any layer within the structure of interest, for practical reasons in determining the roots to the indirect eigenvalue problem $(det[G_{eh}(\gamma)])$ we choose to match the fields where the tangential field components are at their maximum. The solution to the indirect eigenvalue problem is often easier to find when the mode power is at its maximum. This often occurs at the center of the structure.

To derive this relationship we start by working our way from the top and bottom limits imposing the necessary continuity conditions to the transformed tangential fields at each layer interface. Starting from

the bottom limit and working our way up to layer j (referring to Figure 3.4) we obtain, using (3-37), the following admittance type relationships.

$$\tilde{h}_b^{(j)} = Y^{(j)}\tilde{e}_b \tag{3-41}$$

with $Y^{(j)}$ defined recursively

$$Y^{(j)} = y_2^{(j)}\left[y_1^{j} - Y^{(j-1)}\right]^{-1} y_2^{(j)} - y_1^{(j)} \tag{3-42}$$

and where the admittance of the first layer depends on whether the bottom limit is an electric or magnetic boundary condition.

$$Y^{(1)} = \begin{cases} -y_1^{(1)} & \text{electric wall boundary condition for substrate} \\ y_2^{(1)}[y_1^{(1)}]^{-1} y_2^{(1)} - y_1^{(1)} & \text{magnetic wall boundary condition for substrate} \end{cases} \tag{3-43}$$

Likewise, working our way down from the top limit, we obtain the following equations, which hold at position y_a within layer $j+1$.

$$\tilde{h}_a^{(j+1)} = Y^{(j+1)}\tilde{e}_a^{(j+1)} \tag{3-44}$$

$$Y^{(j+1)} = y_1^{(j+1)} - y_2^{(j+1)}[Y^{(j+2)} + y_1^{(j+1)}]^{-1} y_2^{(j+1)} \tag{3-45}$$

with:

$$Y^{(N)} = \begin{cases} y_1^{(N)} & \text{electric wall boundary condition for superstrate} \\ y_1^{(N)} - y_2^{(N)}[y_1^{(N)}]^{-1} y_2^{(N)} & \text{magnetic wall boundary condition for superstrate} \end{cases} \tag{3-46}$$

In the same way, using (3-39), we derive an impedance type relationship:

$$\tilde{e}_b^{(j)} = Z^{(j)}\tilde{h}_b^{(j)} \tag{3-47}$$

where:

$$Z^{(j)} = z_2^{(j)}\left[z_1^{j} - Z^{(j-1)}\right]^{-1} z_2^{(j)} - z_1^{(j)} \tag{3-48}$$

with:

$$Z^{(1)} = \begin{cases} z_2^{(1)}[z_1^{(1)}]^{-1} z_2^{(1)} - z_1^{(1)} & \text{electric wall boundary condition for substrate} \\ -z_1^{(1)} & \text{magnetic wall boundary condition for substrate} \end{cases} \tag{3-49}$$

For the top part:

$$\tilde{e}_a^{(j+1)} = Z^{(j+1)}\tilde{h}_a^{(j+1)} \tag{3-50}$$

where:

$$Z^{(j+1)} = z_1^{(j+1)} - z_2^{(j+1)}[Z^{(j+2)} + z_1^{(j+1)}]^{-1} z_2^{(j+1)} \tag{3-51}$$

with:

$$Z^{(N)} = \begin{cases} z_1^{(N)} - z_2^{(N)}[z_1^{(N)}]^{-1} z_2^{(N)} & \text{electric wall boundary condition for superstrate} \\ z_1^{(N)} & \text{magnetic wall boundary condition for superstrate} \end{cases} \tag{3-52}$$

3.2.9 Indirect Eigenvalue Problem

We now define our indirect eigenvalue problem by enforcing the matching condition on the tangential field one last time at the interface between layer j and layer $j+1$. This yields a modal matrix for the transformed tangential electric fields or magnetic fields given by:

$$G_e(\gamma)\tilde{e}_b^{(j)} = 0 \tag{3-53}$$

$$G_h(\gamma)\tilde{h}_b^{(j)} = 0 \tag{3-54}$$

Equation (3-53) or equation (3-54) is a homogeneous linear system of equations for which a non-trivial solution exist if and only if:

$$\det\left[G_{e,h}(\gamma)\right]=0 \tag{3-55}$$

The solution to the indirect eigenvalue problem (3-55) gives the propagation constant γ, which fully characterizes a mode.

Table 3.1 summarizes the possible formulations for the modal matrices. While all modal matrices listed in Table 3.1 are mathematically equivalent in yielding the same propagation constant γ, some formulations may be more numerically stable as well as more computationally efficient than others.

Top and Bottom Boundary Conditions	$G_e(\gamma)$	$G_h(\gamma)$
Electric wall, electric wall	$Y^{(i-1)} - Y^{(i)}$	$[Y^{(i-1)}]^{-1} - [Y^{(i)}]^{-1}$
Electric wall, magnetic wall	$Y^{(i-1)} - [Z^{(i)}]^{-1}$	$[Y^{(i-1)}]^{-1} - Z^{(i)}$
Magnetic wall, magnetic wall	$[Z^{(i-1)}]^{-1} - Y^{(i)}$	$Z^{(i-1)} - [Y^{(i)}]^{-1}$
Magnetic wall, electric wall	$[Z^{(i-1)}]^{-1} - [Z^{(i)}]^{-1}$	$Z^{(i-1)} - Z^{(i)}$

Table 3.1 Modal matrix formulations

From Table 3.1 we can make some general practical statements about the construction of the modal matrix. It is generally less computationally expensive to construct a modal matrix that avoids the use of a matrix inversion. Hence, when possible, matrix inversion in the construction of the modal matrix should be avoided. We also note that the submatrices z_1 and y_1 contain hyperbolic *tanh* functions which are numerically stable regardless of the layer thickness (i.e. $x \to \pm\infty$, $\tanh(x) \to \pm 1$). However, this is not the case for z_2 and y_2 as the hyperbolic *sinh* function approaches infinity for large arguments

(i.e. $x \rightarrow \pm\infty$, $sinh(x) \rightarrow \pm\infty$). To overcome this problem involving thick layers it may become necessary to divide a thick layer into a number of smaller layers, thus numerically stabilizing the *sinh* function.

3.2.10 Generating Field Distributions

One of the disadvantages in using the MoL is the inability to determine quickly that the solution to the indirect eigenvalue problem is correct and desirable. Often a poor initial guess will lead to convergence to higher order modes, hybrid modes or cavity modes. While the first two roots are legitimate and do exist a designer is often interested only in the fundamental mode of the guide. The third mode is a result of a close computational domain, which can be viewed as an asymmetric dielectric ridge waveguide. In general one must generate the field distribution to determine if the desired roots has been obtained. It is only through direction observations of the field distributions that additional information can be provided about the nature of the propagation constant.

The distributions can be found by inverting equation (3-21), which yields

$$\begin{bmatrix} \Phi^{TM}_{y} \\ \dfrac{d\Phi^{TE}_{y}}{dy} \\ \dfrac{d\Phi^{TM}_{y}}{dy} \\ \Phi^{TE}_{y} \end{bmatrix} = \begin{bmatrix} 0 & j\gamma Q^{-1}_{21} & 0 & 0 \\ \gamma Q^{-1}_{12} & -\gamma^2 Q^{-1}_{12} Q_{11} Q^{-1}_{21} & 0 & 0 \\ 0 & 0 & -\gamma^2 Q^{-1}_{43} Q_{44} Q^{-1}_{34} & \gamma Q^{-1}_{43} \\ 0 & 0 & j\gamma Q^{-1}_{34} & 0 \end{bmatrix} \begin{bmatrix} \tilde{e}_z \\ \tilde{e}_x \\ \tilde{h}_x \\ \tilde{h}_z \end{bmatrix} \quad \text{(3-56)}$$

Equation (3-56) is known for any vertical position within a layer. Using (3-56) along with equations (3-35) and (3-36) the following expression are obtained:

$$\Phi_y^{TE}(y_a) = j\gamma[\cosh(\gamma_e d)]Q^{-1}_{34}\tilde{h}_x(y_b) - \gamma[\gamma_e]^{-1}[\sinh(\gamma_e d)]Q^{-1}_{12}\tilde{e}_z(y_b) + \gamma^2[\gamma_e]^{-1}[\sinh(\gamma_e d)]Q^{-1}_{12}Q_{11}Q^{-1}_{21}\tilde{e}_x(y_b) \quad \textbf{(3-57a)}$$

$$\frac{d\Phi_y^{TE}(y_a)}{dy} = -j\gamma[\gamma_e][\sinh(\gamma_e d)]Q^{-1}_{34}\tilde{h}_x(y_b) + \gamma[\cosh(\gamma_e d)]Q^{-1}_{12}\tilde{e}_z(y_b) - \gamma^2[\cosh(\gamma_e d)]Q^{-1}_{12}Q_{11}Q^{-1}_{21}\tilde{e}_x(y_b) \quad \textbf{(3-57b)}$$

$$\Phi_y^{TM}(y_a) = j\gamma[\cosh(\gamma_h d)]Q^{-1}_{21}\tilde{e}_x(y_b) + \gamma^2[\gamma_h]^{-1}[\sinh(\gamma_h d)]Q^{-1}_{43}Q_{44}Q^{-1}_{34}\tilde{h}_x(y_b) - \gamma[\gamma_h]^{-1}[\sinh(\gamma_h d)]Q^{-1}_{43}\tilde{h}_z(y_b) \quad \textbf{(3-57c)}$$

$$\frac{d\Phi_y^{TM}(y_a)}{dy} = -j\gamma[\gamma_h][\sinh(\gamma_h d)]Q^{-1}_{21}\tilde{e}_x(y_b) - \gamma^2[\cosh(\gamma_h d)]Q^{-1}_{43}Q_{44}Q^{-1}_{34}\tilde{h}_x(y_b) + \gamma[\cosh(\gamma_h d)]Q^{-1}_{43}\tilde{h}_z(y_b) \quad \textbf{(3-57d)}$$

Which describe the fields below the interface. Like wise the following expressions describe the fields above the interface layer.

$$\Phi_y^{TE}(y_b) = j\gamma[\cosh(\gamma_e d)]Q^{-1}_{34}\tilde{h}_x(y_a) + \gamma[\gamma_e]^{-1}[\sinh(\gamma_e d)]Q^{-1}_{12}\tilde{e}_z(y_a) - \gamma^2[\gamma_e]^{-1}[\sinh(\gamma_e d)]Q^{-1}_{12}Q_{11}Q^{-1}_{21}\tilde{e}_x(y_a) \quad \textbf{(3-58a)}$$

$$\frac{d\Phi_y^{TE}(y_b)}{dy} = j\gamma[\gamma_e][\sinh(\gamma_e d)]Q^{-1}_{34}\tilde{h}_x(y_a) + \gamma[\cosh(\gamma_e d)]Q^{-1}_{12}\tilde{e}_z(y_z) - \gamma^2[\cosh(\gamma_e d)]Q^{-1}_{12}Q_{11}Q^{-1}_{21}\tilde{e}_x(y_z) \quad \textbf{(3-58b)}$$

$$\Phi_y^{TM}(y_b) = j\gamma[\cosh(\gamma_h d)]Q^{-1}{}_{21}\tilde{e}_x(y_a) - \gamma^2[\gamma_h]^{-1}[\sinh(\gamma_h d)]Q^{-1}{}_{43}Q_{44}Q^{-1}{}_{34}\tilde{h}_x(y_a) + \gamma[\gamma_h]^{-1}[\sinh(\gamma_h d)]Q^{-1}{}_{43}\tilde{h}_z(y_a) \quad \textbf{(3-58c)}$$

$$\frac{d\Phi_y^{TM}(y_b)}{dy} = j\gamma[\gamma_h][\sinh(\gamma_h d)]Q^{-1}{}_{21}\tilde{e}_x(y_a) - \gamma^2[\cosh(\gamma_h d)]Q^{-1}{}_{43}Q_{44}Q^{-1}{}_{34}\tilde{h}_x(y_a) + \gamma[\cosh(\gamma_h d)]Q^{-1}{}_{43}\tilde{h}_z(y_a) \quad \textbf{(3-58d)}$$

To find the E_x, H_z E_z and H_x field components we used the above relationships and equation (3-21). To find the E_y and H_y field components we must make use of (3-5b) and (3-5e). The appropriate transform and difference operators are substituted into these expressions given the layer. We then obtain

$$E^n{}_y = \begin{cases} U_e\Phi_y^{TE} + \dfrac{1}{j\omega\gamma\varepsilon_o h_{min}}[\varepsilon]^{-1}{}_e D_x{}^t U_h \dfrac{d\Phi_y^{TM}}{dy} \\ U_e\Phi_y^{TE} - \dfrac{1}{j\omega\gamma\varepsilon_o h_{min}}[\varepsilon]^{-1}{}_e D_x U_h \dfrac{d\Phi_y^{TM}}{dy} \end{cases} \quad \textbf{(3-59)}$$

$$H^n{}_y = \begin{cases} U_h\Phi_y^{TM} + \dfrac{1}{j\omega\gamma\mu_o h_{min}} D_x U_e \dfrac{d\Phi_y^{TE}}{dy} \\ U_e\Phi_y^{TM} - \dfrac{1}{j\omega\gamma\mu_o h_{min}} D_x{}^t U_h \dfrac{d\Phi_y^{TE}}{dy} \end{cases} \quad \textbf{(3-60)}$$

Where the E_y and H_y components are given by (3-16).

3.3 Validation of the Method of Lines

To thoroughly validate the above formulation and MoL program, several structures were examined in detail and compared against the results published in the scientific literature. These structures include two different lossless rib waveguides and a lossy Schottky contact TWPD. Richardson's extrapolation is discussed and used when appropriate to determine a more accurate value of γ. To model the open structure, the lateral and vertical boundary conditions were placed sufficiently far away from the mode. In order to determine if the lateral boundary conditions had any effect on the mode profile, the boundary conditions were augmented accordingly. When possible a direct comparison is made between results computed with the same method and any discrepancies are discussed.

3.3.1 Validation of the MoL for Lossless Structures

The first lossless rib structure that was analyzed is illustrated below in Figure 3.5. Full wave analysis using the MoL was done for the E_x^{11} mode to determine a single value of n_{eff} at a free space wavelength of $\lambda_o = 1.55\ \mu m$. Vertical symmetry can be observed in this structure and is used to reduce the number of lines. This results in a reduction in computational time. To accurately model this rib waveguide a hybrid discretization scheme is adopted, the exact details of which have previously been discussed. Both vertical and horizontal boundary conditions are placed sufficiently far away from the rib to characterize the structure as being open. The boundary conditions are then changed to observe if this had any effect on the normalized propagation constant (n_{eff}). Shown in Table 3.2 are the computed values of n_{eff} for different line discretizations for ew-ew lateral boundary conditions and mw-mw horizontal boundary conditions.

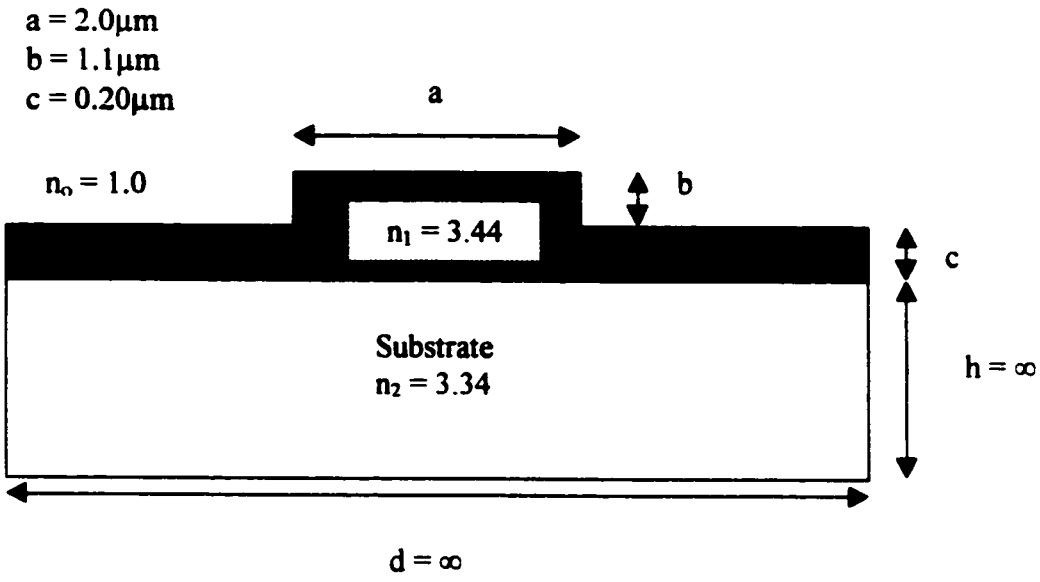

Figure 3.5 First lossless optical rib waveguide.

Number of Lines	h_{max} (μm)	n_{eff} for (ew-ew)
20	0.20	3.38918526553
40	0.10	3.38884546903
80	0.05	3.38874269558
160	0.025	3.38871289695
320	0.0125	3.38870417967

Table 3.2: n_{eff} for different line discretizations

Although not included here since the differences are too small, it should be noted that different vertical and horizontal boundary conditions were implemented. The observed effect due to changing the lateral boundary conditions from ew-ew to ew-mw is less than a 10^{-15} change in the value of n_{eff}. The effect is similar for horizontal boundary conditions.

We observe from Table 3.2 that the computed values monotonically approach a final value of n_{eff} as the number of lines increases (i.e.↑ N) or equivalently the discretization interval decreases (i.e. ↓ h_{min}). Figure 3.6 demonstrates this from 4 to 120 lines.

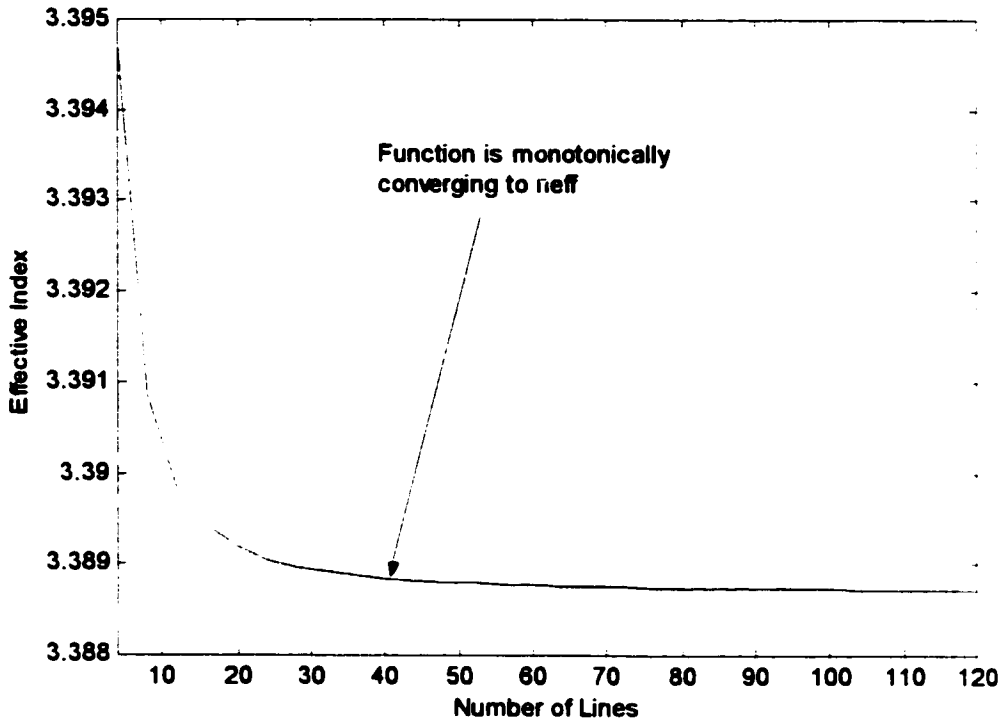

Figure 3.6 Effective index n_{eff} vs. number of lines

We observe that the function in Figure 3.6 is monotonically approaching 3.388. In the above situation where the convergence is observed to be monotonic we can make use of the convergence history. That is we can use previously computed values of n_{eff} to determine a more accurate value of n_{eff} via extrapolation.

Richardson's extrapolation is the method used to extrapolate a more accurate result of n_{eff}. This technique requires computed results where the number of lines is successively double, or equivalently the discretization interval is successively halved. The extrapolation formula is given by[84]:

$$E_n(h) = \frac{2^n E_{n-1}(h) - E_{n-1}(2h)}{2^n - 1} \tag{3-61}$$

E_o corresponds to the original computed results and h is equal to h_{min} which is the minimum discretization interval, and n corresponds to the level of the extrapolation. Therefore, if we have n computed results we have n-1 levels, where the n-1 extrapolation level is the most accurate.

Table 3.3 shows Richardson's extrapolation computed for the data given in Table 3.2.

h_{min} (μm)	E_o	E_1	E_2	E_3	E_4
0.20	3.38918526553				
0.10	3.38884546903	3.38850567253			
0.05	3.38874269558	3.38863992213	3.38868467200		
0.025	3.38871289695	3.38868309831	3.38869749037	3.38869932157	
0.0125	3.38870417967	3.38869546239	3.38869958375	3.38869988280	3.38869992022

Table 3.3 Richardson's extrapolation values for n_{eff}

The extrapolated value appears to converge to a n_{eff} = 3.38869992022. Comparing this result with those presented in the scientific literature yields Table 3.4.

Sources	n_{eff}
Computation in this Thesis (MoL)	3.388699
Berini et al[85] (MoL)	3.388698
Lusse et al[86] (Finite Difference Method)	3.388687
Rozzi et al[87]. (Transverse Resonance Diffraction Method)	3.388690

Table 3.4 Computed n_{eff} compared with results in literature

We observe from Table 3.4 that the results computed here using the MoL agree well with those published in the scientific literature. Comparing this result directly with Berini et al. who also used the MoL to determine the value of n_{eff} we observe a difference of 10^{-6} in the value of n_{eff}. This can be accounted for by considering the use of different numerical routines (i.e. numerical diagonalization, eigenvalue, root searching routines) or different computational processing architecture (RISC vs. CISC).

To ensure that this is the correct propagation constant obtained from the solution to the indirect eigenvalue problem all six field components are generated and shown in Figures 3.7a-3.7f. Since the root found corresponds to the E_x^{11} mode, we expect that the E_x field component to have one extrema in both the x and y directions. Referring to Figure 3.7a we observe that this is true and hence conclude that the correct and desired mode has been calculated.

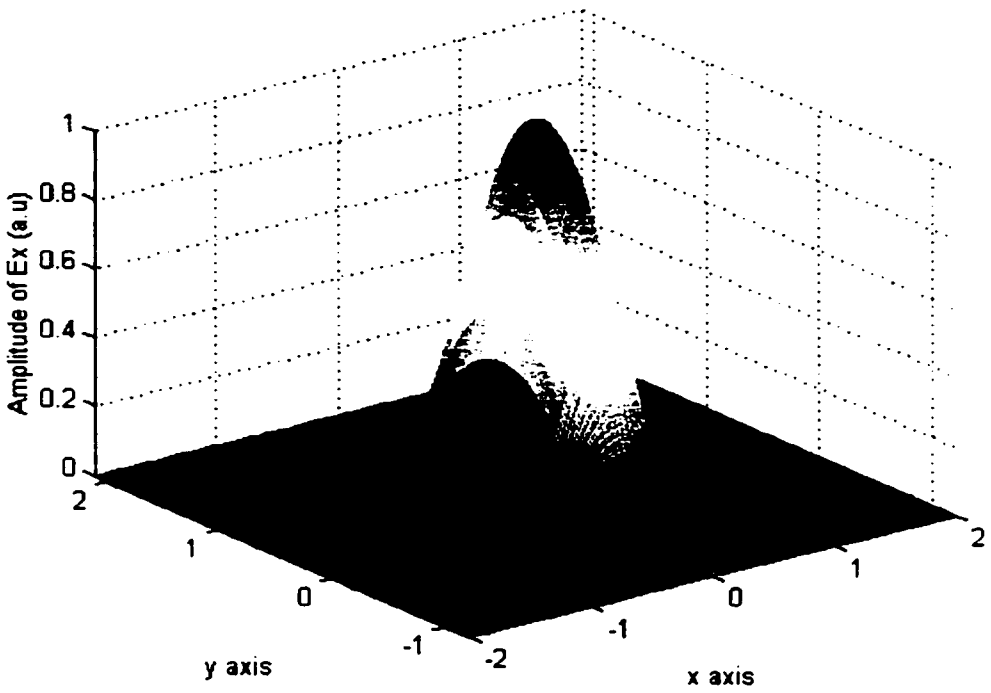

Figure 3.7a E_x field distribution for first lossless rib structure in E_x^{11} mode

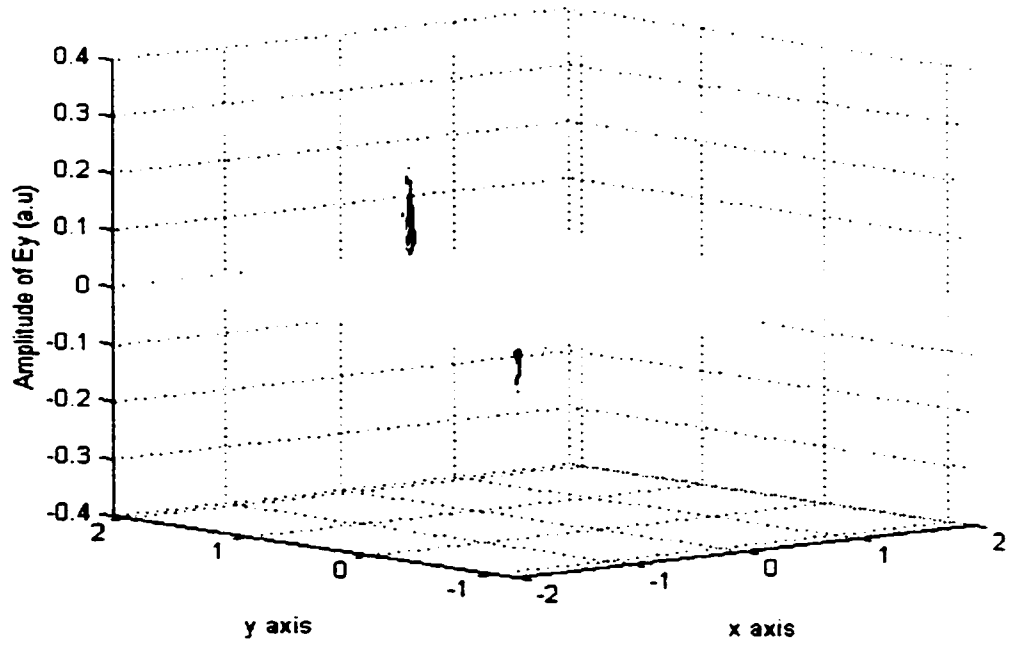

Figure 3.7b E_y field distribution for first lossless rib structure in E_x^{11} mode

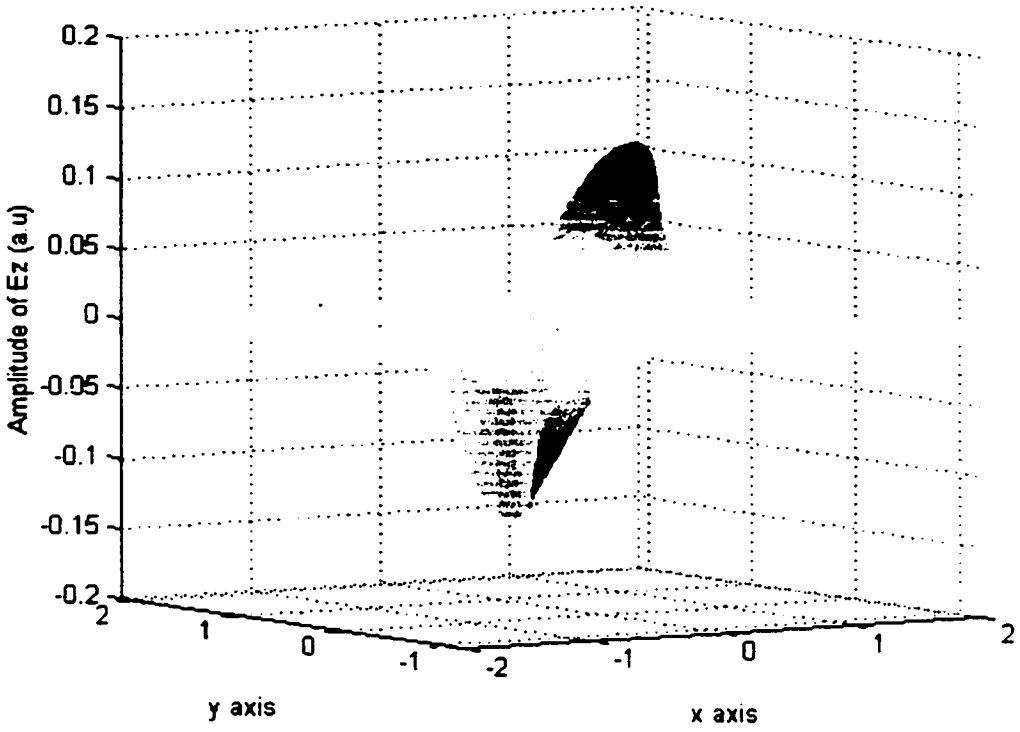

Figure 3.7c E_z field distribution for first lossless rib structure in E_x^{11} mode

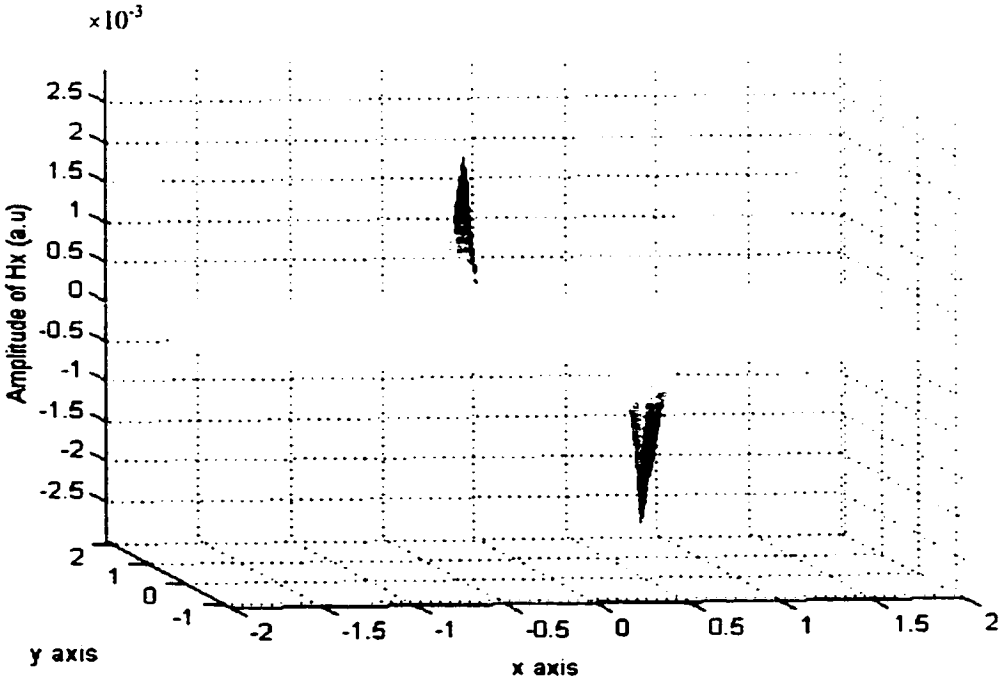

Figure 3.7d H_x field distribution for first lossless rib structure in E_x^{11} mode

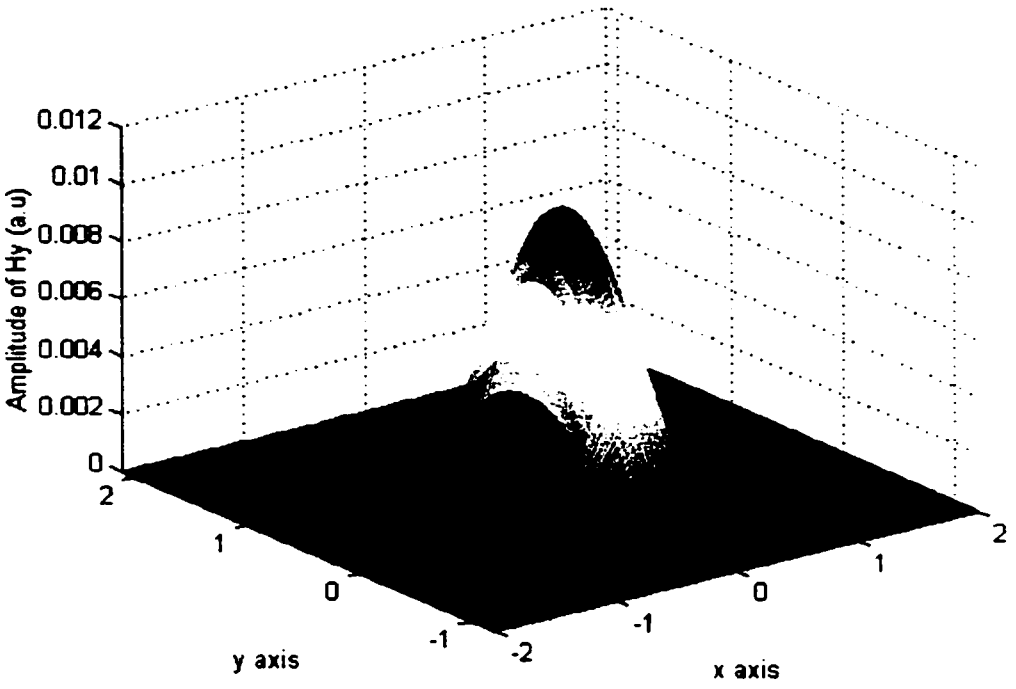

Figure 3.7e H_y field distribution for first lossless rib structure in E_x^{11} mode

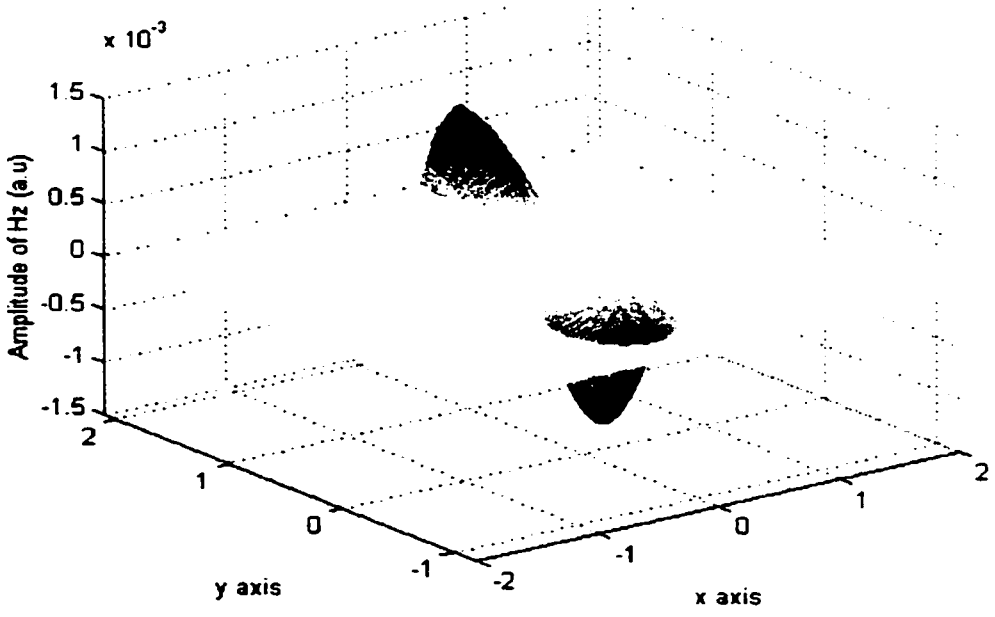

Figure 3.7f H_z field distribution for first lossless rib structure in E_x^{11} mode

Since the formulation and MoL program will be used in the design of the TWPD we must ensure that the method is thoroughly tested. Therefore we cannot base the entire validation on a single data point. A second lossless structure is analyzed using the MoL where the entire dispersion curve is generated and compared against the results provided in the literature. This structure is illustrated in Figure 3.8.

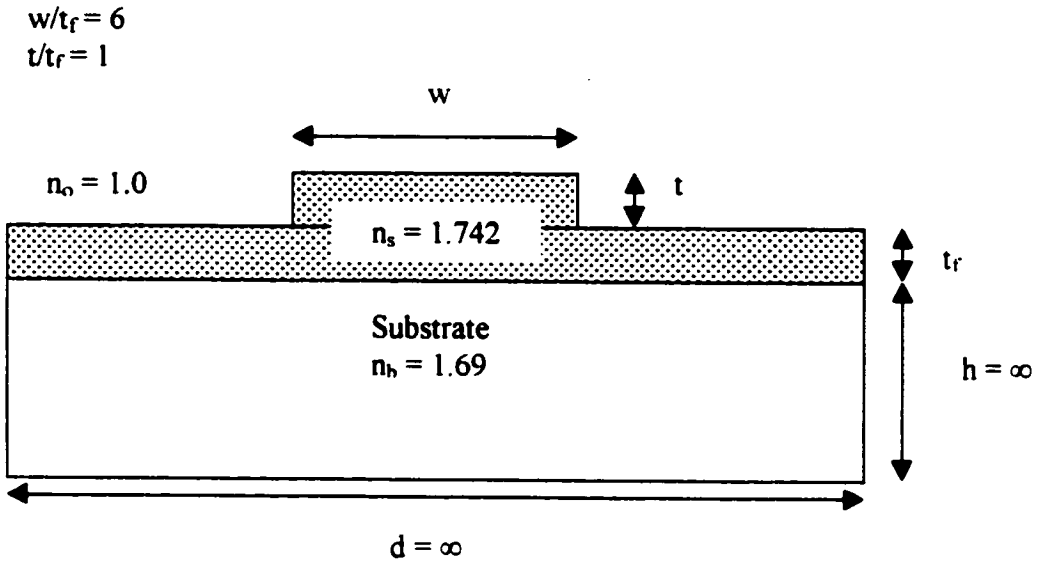

Figure 3.8 Second lossless optical rib structure

Again the vertical symmetry is exploited down the center of the structure by placing a vertical electric wall for the E_x^{11} mode and a vertical magnetic wall for E_y^{11} mode. While the entire E_x^{11} and E_y^{11} dispersion curves are generated, no extrapolation is performed to determine more accurate values for each dispersion point. These results are presented in Figure 3.9.

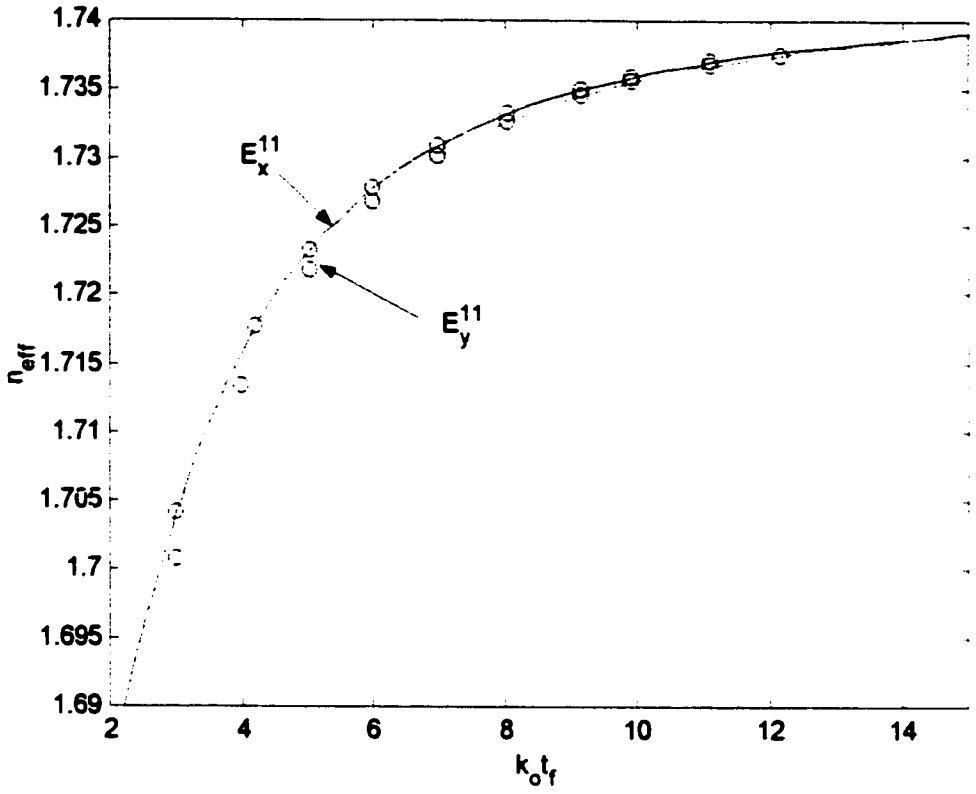

Figure 3.9 n_{eff} vs $k_o t_f$ for second lossless rib structure

The solid lines represent the computed values and the "o" represent the values from Rogge and Pregla[88] et al. It should be noted that reference [88] also used the MoL to compute the dispersion curve. Although not visible there is a difference between the numerical values computed and those reported in [88] of 10^{-5}. However, like the previous example these differences can be accounted for by numerical routines, computer architecture and the fact that reference [88] uses a potential based MoL formulation. Despite the small differences the results agree fairly well with those presented in the literature.

3.3.2 Validation of MoL for Lossy Structure

All of the structures modeled up to this point have been lossless. However, in order to fully characterize a TWPD one must be able to determine the losses in the structure. This can be done in a similar manner to the lossless structure, where the nontrivial solution to the indirect eigenvalue problem (i.e. $\det[G_{e,h}(\gamma)] = 0$) yields the propagation constant. Unlike the lossless case where the roots to this problem are on the positive real axis, the roots in the lossy case must be found in the complex domain. The solution to this problem will yield the propagation constant $\gamma = \alpha + j\beta$ which fully characterizes the mode.

The structure analyzed for the lossy case is illustrated below in Figure 3.10[89].

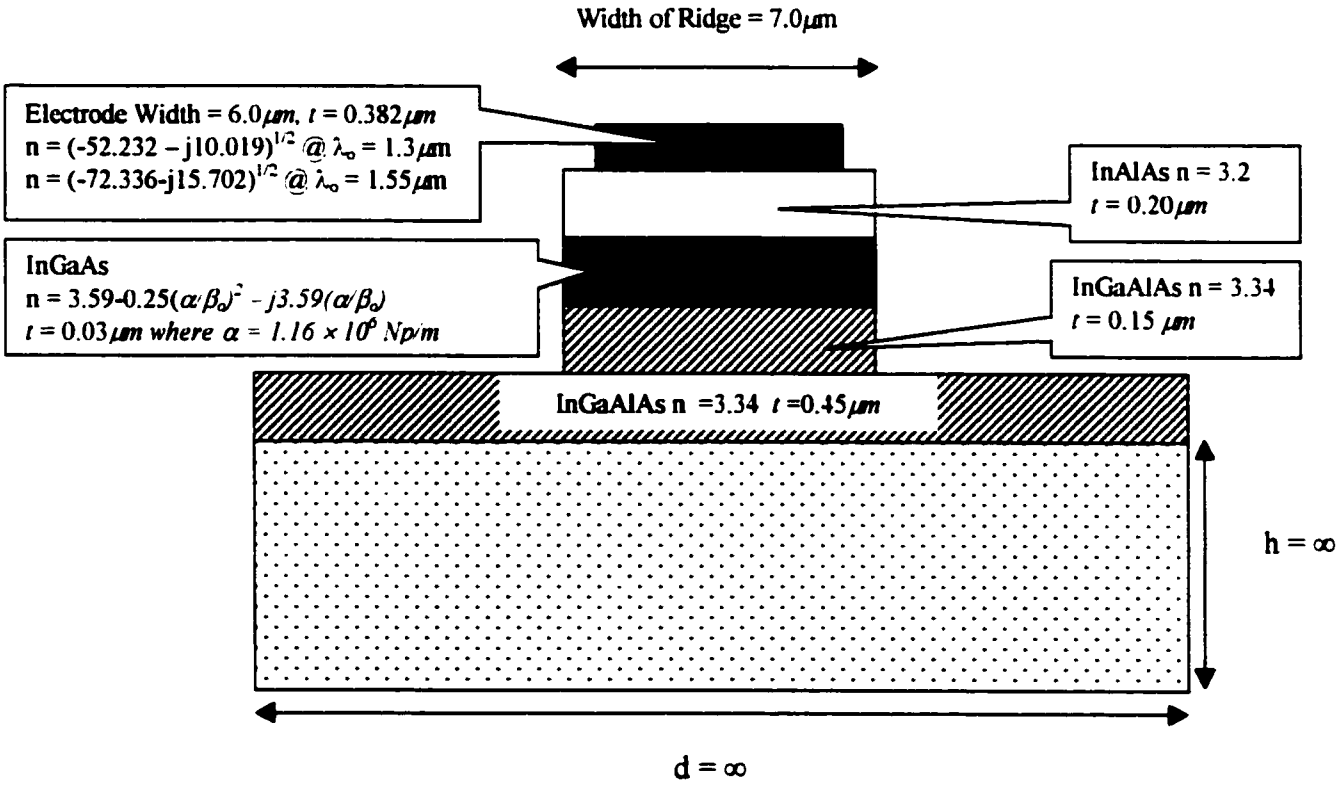

Figure 3.10 Schottky contact TWPD

Table 3.5 shows the results for the lossy case compared to those published by Berini et al[89]. The structure is modeled with using a 40 line hybrid discretization with no extrapolation taken.

Polarisation	Wavelength λ_o	Phase Constant β/β_o	Attenuation Constant $\alpha/\beta_o \times 10^{-3}$	Phase Constant Berini et al. β/β_o	Attenuation Constant Berini et al. $\alpha/\beta \times 10^{-3}$
E_x^{11}	1.3μm	3.282243	2.9610659	3.282227	2.963627
	1.55μm	3.264978	3.210444	3.264955	3.211380
E_y^{11}	1.3μm	3.260217	3.517838	3.260444	3.517666
	1.55μm	3.227240	5.339103	3.227783	5.340059

Table 3.5 Computed propagation constants for Schottky contact TWPD

We observe that the computational accuracy is not as high as those presented for the lossless case. This is due to the fact the electrode was modeled as being 7 μm as opposed to 6μm. As well the differences could arise from the fact that the numerical routine used to compute the root in the lossy case was different than the routine used to compute the root in the lossless case. In the lossless case a commercially available routine provided by Matlab was used. However, in the lossy case an in house routine based on Muller's[90] method was coded. This routine may not be as efficient or numerically accurate as those routines provided commercially. Despite the difference, the accuracy is sufficient to use the MoL in the design of the TWPD. The differences in the propagation constant in Table 3.5 above accounts for at most a 0.01 dB difference in the absorption coefficient.

In summary an algorithm has been presented and coded via Matlab. Three separate structures were analyzed to validate both the derivation and the program. The result of which demonstrates the MoL ability to model both lossy and lossless structures. The MoL along with the expressions presented in Chapter 2 are used to design two TWPDs.

Chapter 4 Design and Simulation

The previous two chapters introduced the material types, design parameters and models which are used in the design of a TWPD. TWPDs like the one shown in Figure 2.11 present three different design problems to be solved with competing design requirements. First, the choice of semiconductor parameters for the p-i-n photodetector determines the wavelength of optical absorption, carrier transit time and probability of recombination. Second, the optical waveguide is designed as a rib structure and must be optimized such that the peak intensity of the mode field occurs in the detection region thus maximizing optical absorption. Maximizing optical absorption will increase the responsivity and sensitivity of the device. Third, the microwave waveguide is designed as a quasi-coplanar structure with the center metallization deposited on top of the rib. This center metallization must be placed far enough from the optical mode field peak to ensure that no deleterious effects are introduced on the propagation.

This chapter will present the design of two traveling wave photodetectors. We will start with the photodiode architecture. This is followed by the semiconductor layer design used for the detection of optical energy. Next, the optimized optical waveguides will be discussed which will include any effects seen on the optical phase constant as a result of the top metallization. Subsequently the microwave performance of the quasi-coplanar waveguide is analyzed, discussing key design parameters such as microwave loss, phase velocity mismatch and characteristic impedance. The chapter will conclude with a discussion of the mask design and fabrication issues.

4.1 Photodiode Architecture

As discussed in Chapter 2 a TWPD could have been designed using an avalanche, Schottky or p-i-n architecture. The original objective for the work was the design of a high speed, high efficiency detector, thus the use of an avalanche photodiode can immediately be ruled out as a possible architecture. We

therefore have two architectures left, the Schottky contact TWPD and the p-i-n TWPD. As a designer the choice is obvious, when one compares a well designed Schottky detector with a well designed p-i-n detector, the Schottky detector will generally be the faster device. This is due to the fact that these devices are majority carrier devices hence, are not limited by minority carrier recombination time as seen with p-i-n diodes. However, Schottky contacts on InP are notoriously leaky, in fact a considerable amount of development work would have had to be done in terms of processing in order to minimize the leakage current. As a result a Schottky contact configuration was not chosen. By default, one is left with a p-i-n detector, which despite the fact that it is a minority carrier device has been demonstrated to operate at exceptionally high speeds.

4.2 Semiconductor Layer Parameters

As stated in Chapter 1 the work focuses on the third optical transmission window centered at 1550nm. InP is the semiconductor material often used in the design of optoelectronic devices in this domain. It is a direct bandgap semiconductor hence, has a strong optical absorption coefficient, it has high electron mobility, high thermal conductivity and high electric field breakdown. Thus, the design of all p-i-n heterostructure will be done on a InP substrate.

4.2.1 Heterostructure Material Choice

Due to the fact that the design of a p-i-n diode involves a number of semiconductor layers each with different bandgap profiles to form a heterostructure, good lattice matching is critical. While it is not possible to have perfect lattice matching, minimizing the lattice mismatch will ensure that minimal strain is introduced into the layers and thus reduce the number of defects present at the interfacial layers. Thus good

lattice matching has the positive effect of reducing the series resistance in the diode and minimizing the number of traps responsible for carrier recombination.

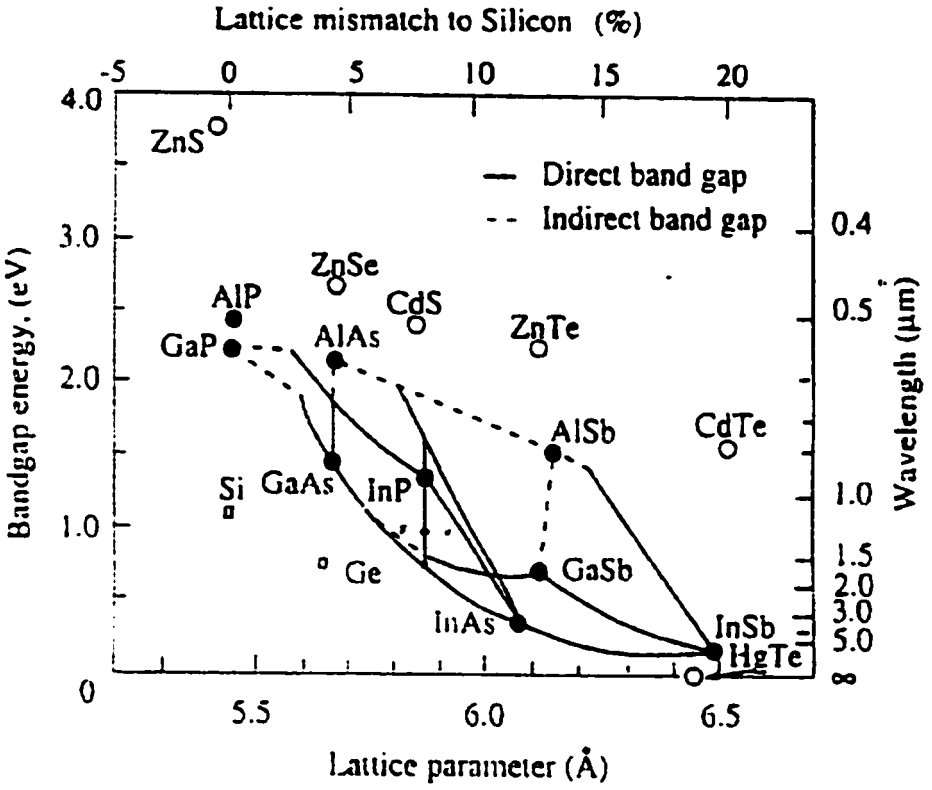

Figure 4.1 Lattice constants and bandgap of semiconductor materials[91]

Referring to Figure 4.1 we see that there are two material systems that can be lattice matched to InP, they are InAlAs/InGaAs/InP and InGaAs/InGaAsP/InP. One could have chosen to work with Al material system, however, it was determined that very few labs grow Al since it is difficult to work with due to the fact that it oxidizes rapidly. If we chose to proceed with this material system this would have meant a considerable amount of engineering development work to ensure that the fabrication process was stable and mature. For this reason the alternative material system consisting of InGaAs/InGAsP/InP was used to construct the equivalent heterostructure diode.

As discussed in Chapter 2 if careful attention is not paid to the material design, optical energy will either not be detected or be detected at the incorrect wavelength. Therefore, to ensure that detection occurs at 1550nm we must guarantee that the bandgap energy of the absorbing layer is lower than the energy carried in a photon of light at 1550nm.

4.2.2 Increasing Efficiency via Bandgap Engineering

One of the important design parameters in fabricating a detector is the maximization of quantum efficiency. One way of achieving this is to introduce excitons at room temperature. These excitons which are e-h pairs bound together by the Coulomb force cause peaks in the absorption spectra at lower temperature in bulk material. In order to make use of them at room temperature a designer must introduce a quantum well structure. The quantum well provides carrier confinement, hence there is strong interaction of the electron and hole wave functions. This results in the introduction of excitons at room temperature, which causes a significant increase in the optical absorption coefficient. Thus by placing one or more quantum wells in the intrinsic region one can increase the quantum efficiency. InGaAs is a direct bandgap semiconductor which can be designed to have high optical absorption around 1550 nm, it can be easily latticed matched to InP and for this reason was chosen as the material for the active absorbing layer. The molar fraction for the InGaAs quantum well(s) was determined using the following well known bandgap relationship for $In_{(1-x)}Ga_xAs_yP_{(1-y)}$[91].

$$E_g = 1.35 - 0.72y + 0.12y^2 \qquad \textbf{(4-1)}$$

where $x = 0.47y$ for lattice matching to InP.

By definition a QW is formed when a narrow bandgap material is completely enclosed by a larger bandgap material, provided that the narrow bandgap material is thin enough so that the carriers experience confinement in one direction. Therefore, in order to complete the design of the QW one must place two

large semiconductor bandgap materials on either side of the InGaAs absorbing layer. These layers are the barrier layers, which are used to confine the carriers, thus completing the design of a QW. Hence, as a semiconductor designer one must optimize the bandgap energy of the barrier layers such that it is much larger than the bandgap present in InGaAs. This was also done using equation (4-1) while maintaining the constraint of lattice matching.

4.2.3 Optimized Layer Designs

Classically, traveling wave devices are usually made several wavelengths long such that there is a considerable amount of interaction between the two waves as they propagate down their respective guides. As well, the bandwidth of traveling wave devices, in the classical sense of the word, is usually determined by the coherent interaction of these two waves. That is the amount of velocity matching between the waves generally determines the bandwidth of these devices. In the case of the traveling wave detector, the theory presented in Chapter 2 not only states that these devices are electrically very short and optically very long, it also suggests via equation (2-37) that the bandwidth is independent of velocity matching. This raises several interesting and perplexing questions, the most critical being why are these devices called traveling wave if there exists almost no interaction between the microwave and optical signals? As a consequence of this question it was decide that two detectors should be fabricated. The idea behind fabricating two devices is simple, one TWPD would behave as a control device while the other TWPD was the test device. In doing this a direct comparison could be made between both devices in assessing, empirically, the importance of key parameters such as velocity matching, microwave loss and characteristic impedance on bandwidth and responsivity.

Structure A, the test device, was designed to have good velocity matching, maximum return loss and minimum insertion loss. Structure B, the control device did not take into account any of the previously mentioned parameters. Instead it made use of a geometry presented by Bower[92] et al. There were only

three minor design modifications made to this TWPD compared to the TWPD presented in the literature[92]. First the operating wavelength presented in the literature occurred at 830 nm as opposed to 1550 nm, hence a different material system was required. Secondly, the p^{--} and n^{--} contacts were swapped and finally MQWs were added to the device to increase the optical absorption coefficient.

Figure 4.1 through Figure 4.5 along with Tables 4.1 and 4.2 describe the optimized semiconductor layer designs, the device architecture and energy bandgap structure for structures A and B.

Function	Material Layers	Layer Thickness (μm)	Doping Type	Optical Index of Refraction n	Microwave Relative Permittivity ε_r
Superstrate	Air	∞	-	1.0	1.0
Metal	Ti/Pt/Au	1.0	-	0.9178 - j8.5544	-
Cladding	InP	0.60	p++	3.1659	12.4
Cladding	InP	1.49	NiD	3.1659	12.4
Core	$In_{0.80}Ga_{0.20}As_{0.43}P_{0.57}$	1.05	NiD	3.2967	12.3
QW	$In_{0.53}Ga_{0.47}As$	0.02	NiD	3.4481	13.9
Core	$In_{0.80}Ga_{0.20}As_{0.43}P_{0.57}$	0.45	NiD	3.2967	12.3
Core	$In_{0.80}Ga_{0.20}As_{0.43}P_{0.57}$	0.60	n++	3.2967	12.3
Substrate	InP	∞	SI	3.1659	12.4

Table 4.1 – Layer parameters for structure A

Table 4.1 gives the layer description for the structure A shown in Figure 4.2. The top layer is composed of InP whose function is to act as the cladding layer for the guide while at the same time p doped to act as the p^{--} contact for collection of holes. Referring to Table 4.1 the next four layers are InP, InGaAsP, InGaAs (QW) and InGaAsP respectively. These layers are non-intentionally doped (NiD) and act as the core for the guide. The InGaAs QW layer is placed between two InGaAsP layers that act as barriers. The detection of the optical signal will occur in the QW region. The e-h pairs generated here will be swept

across the intrinsic InGaAsP layers to their p^{++} and n^{++} contacts respectively. The next layer is n doped InGaAsP region used for the collection of electrons. Finally we have the semi-insulating (SI) InP substrate layer. The bandgap profile of this device is shown in Figure 4.3.

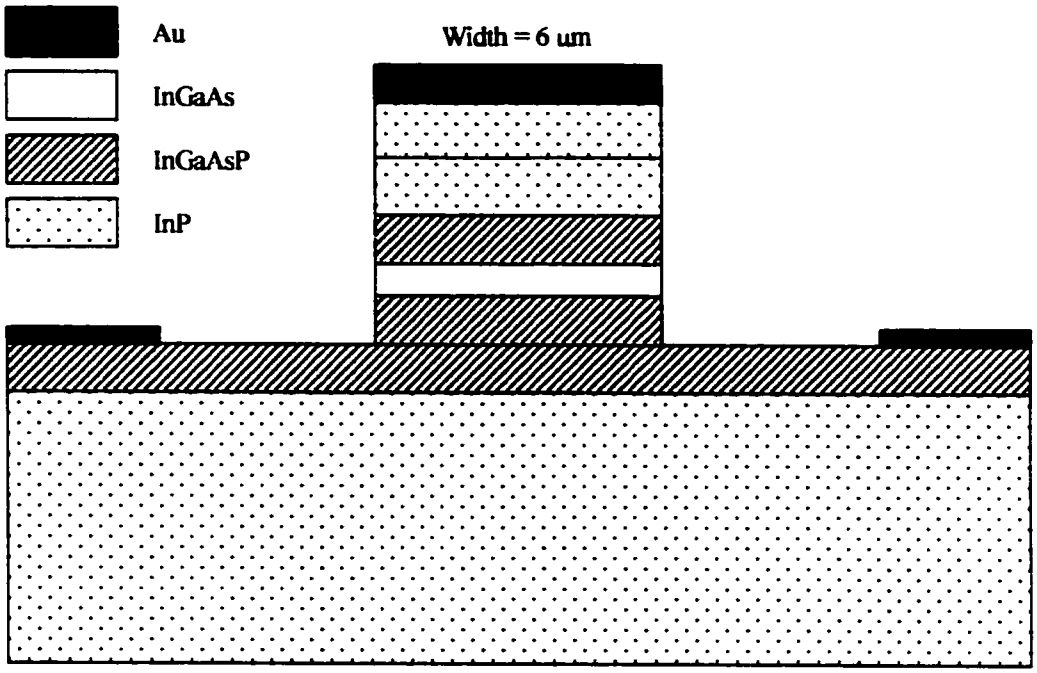

Figure 4.2 Structure A

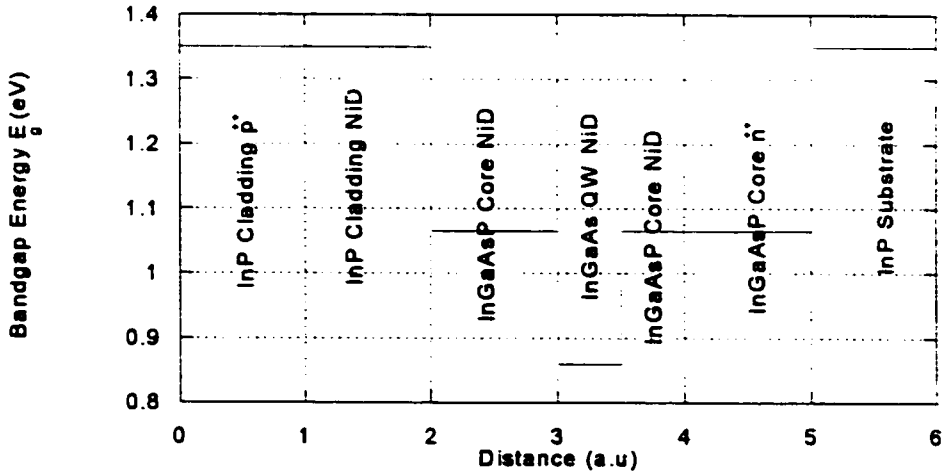

Figure 4.3 Bandgap profile for structure A

In keeping with our design philosophy structure A was optimized such that the microwave quasi-coplanar waveguide has a characteristic impedance of 50 Ω and coherent interaction between the optical and microwave signals. The main parameter that determines the characteristic impedance of this quasi-coplanar waveguide and the velocity of the microwave signal, is the capacitance of the intrinsic region. The quasi-coplanar structure is defined in terms of the signal electrode outlined on top of the rib waveguide as the p^{++} contact metal and the adjacent ground electrodes defined on either side of the rib. The latter are outlined as the n^{++} contacts and can be ten optical wavelengths away from the rib shown in Figure 4.2 and 4.4. This structure is described as a quasi-coplanar waveguide for two reasons: first, if the n^{++} InGaAsP layer is assumed to offer a very low sheet resistance or is equivalently heavily doped, the quasi-coplanar structure described above approaches the geometry of a microstrip and secondly the ground electrodes are not on the same plane as is the case with typical CPWs. The value of the capacitance is a function of the total junction area as well as the distance between the p and n contacts. By varying the thickness of the intrinsic layer one changes the impedance and the phase velocity of the device.

Function	Material Layers	Layer Thickness (μm)	Doping Type	Optical Index of Refraction n	Microwave Relative permittivity ε_r
Superstrate	Air	∞	-	1.0	1.0
Metal	Ti/Pt/Au	1.0	-	0.9178 - j8.5544	-
Cladding	InP	0.60	p++	3.1659	12.4
Cladding	InP	0.14	NiD	3.1659	12.4
Core	$In_{0.80}Ga_{0.20}As_{0.43}P_{0.57}$	0.07	NiD	3.2967	12.3
QW	$In_{0.53}Ga_{0.47}As$	0.01	NiD	3.4481	13.9
Core	$In_{0.80}Ga_{0.20}As_{0.43}P_{0.57}$	0.01	NiD	3.2967	12.3
QW	$In_{0.53}Ga_{0.47}As$	0.01	NiD	3.4481	13.9
Core	$In_{0.80}Ga_{0.20}As_{0.43}P_{0.57}$	0.07	NiD	3.2967	12.3
Core	$In_{0.80}Ga_{0.20}As_{0.43}P_{0.57}$	0.60	n++	3.2967	12.3
Substrate	InP	∞	SI	3.1659	12.4

Table 4.2 Layer parameters for structure B

Table 4.2 gives the layer description for device B shown in Figure 4.4. The top two layers are composed of InP: the p^{--} layer is the contact to the device. Both the doped and undoped InP layers act as the top cladding layers for these detectors. The next six intrinsic layers in Table 4.2 define the core of the guide made of InGaAsP and InGaAs. Similar to the structure A, the InGaAs QW layer is placed between two InGaAsP layers which act as barriers for the QW. A single QW was found to provide insufficient optical absorption, hence a second QW was added to increase the optical sensitivity of the device. Below the intrinsic layers is a n^{--} contact layer made up of InGaAsP core material on top of the semi-insulating InP substrate.

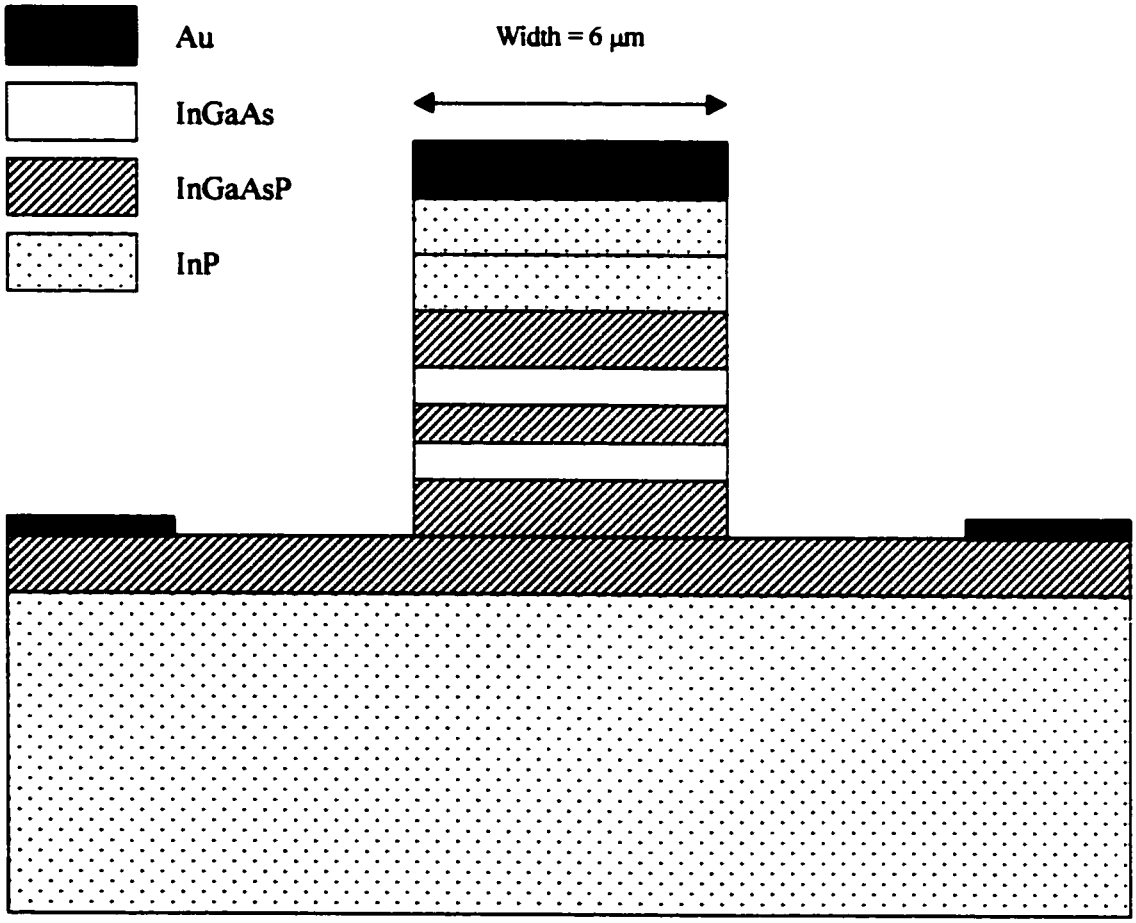

Figure 4.4 Structure B

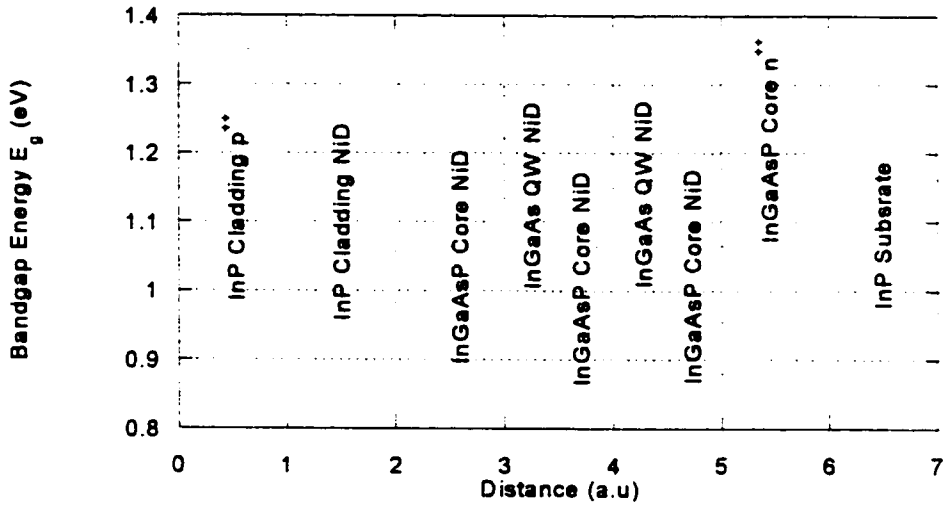

Figure 4.5 Bandgap profile for structure B

Unlike structure A, no attempt was made in this case to achieve phase velocity matching between the optical and microwave signals, nor was there any optimization done to obtain a 50 Ω characteristic impedance for the transmission line. The design philosophy for this device was to observe if velocity mismatch, characteristic impedance are secondary factors in determining the speed of TWPDs.

4.2.3 Tradeoffs and Design Limitations

Several important observations can be made regarding the two designs. First the position of the QW for both may have a fundamental limit on the speed of the device. That is, there is a trade off between the carrier performance of the device and the location of the quantum well(s). Under strong reverse bias conditions, photons having an energy greater than the QW band gap penetrate the QW and intrinsic region of the detector. This results in electron-hole pair generation in the vicinity of the QW. The carriers are collected at the p^{++} and n^{++} contacts. The positioning of the QW in the core layer will determine the

distance the electrons and holes must travel before being collected, and hence, introduce a fundamental limitation in the performance of the device. From a semiconductor perspective, it is ideal to place the QW closest to the p^{++} contact. Holes having a slower mobility than electrons would have less distance to travel before being collected by the p^{++} contact, thus decreasing the carrier transit time and hence increasing the speed of the device. However, placing the QW close to the p^{++} contact would reduce the sensitivity and efficiency because of potential coupling to plasmon-polariton modes supported by the metal.

Another consequence of moving the QW closer to the p^{++} contact is that the optical maxima of the modes would also be closer to the metallization which would increase the optical losses outside the detection area. This increase in loss outside the detection area is generally undesirable and is caused as a direct consequence of the optical mode coupling to plasmon-polariton modes supported by the metal. This would not only short out the mode but would perturb the optical field rendering the devices polarization sensitive by introducing large differences between E_x^{II} and E_y^{II} propagation constants.

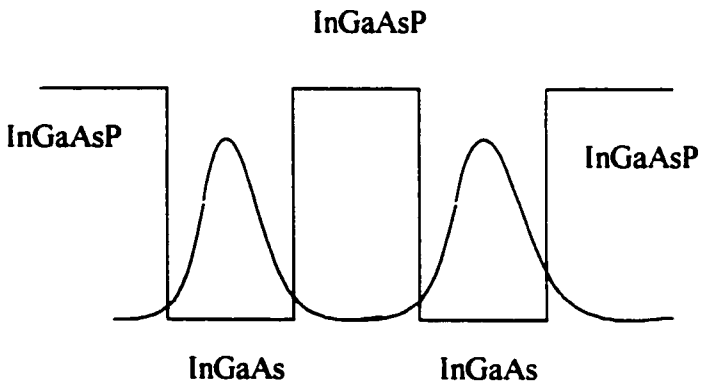

Figure 4.6 Interaction of wave function in structure B

Despite the proper use of the empirical relationships provided in Equation (4-1) in the design of both layer structures, a designer cannot expect the maximum of the absorption peak to occur exactly at 1550 nm. There are several relationships regarding quantum well interaction, biasing etc. which are not considered in the semiconductor layer design presented above. These relationships, which are discussed below outline

possible deficiencies in the design of the semiconductor layer, which may cause a shift in the maximum of the absorption spectra away from the design wavelength of 1550nm.

The interaction of the wave functions in the quantum wells for structure B is one such effect not considered. This is illustrated in Figure 4.6. That is the use of two QWs in device B forms a super lattice since the InGaAsP barrier layer separating the two wells is appreciably thin. Thus, there is considerable interaction as a result of the wave function in the neighboring well. This will result in band bending which would manifest itself in a shift in the absorption spectra. Obviously this effect is only present when there is more than one QW with an appreciably thin barrier layer between them hence, the effect is unique to the design of structure B and should not influence structure A.

In general we expect that when a semiconductor is placed in an electric field the absorption coefficient will change with the applied field. In normal operation of a photodiode one usually applies a strong reverse bias to ensure that the intrinsic region is completely depleted of charge carriers. This photoconductive mode of operation ensures that the electron and holes are at their saturation velocity hence, maximum speed for the device is achieved. Therefore we expect that when we apply a reverse bias to the diode this will have an effect on the absorption coefficient.

Two effects that change the nature of the absorption spectra with applied bias are the Franz-Keldysh effect and the quantum confinement Stark effect. The Franz-Keldysh effect is commonly observed in p-i-n photodiodes when a large electric field or equivalently when a large bias is applied. Depending on amount of band bending present the optical absorption coefficient can either experience a rapid change with bias or an oscillatory change with bias.

The quantum confined Stark effect is the other phenomenon that can be observed when bias is applied to a photodiode. This effect which only occurs in the presence of quantum wells results in a decrease in the absorption coefficient as well as a shift in the absorption spectra.

The designs presented above illustrate an optimized first order layer design considering only the empirical relationship given in (4-1). An important observation was made regarding the position of the QW and the fundamental limitation of the device, as well as deficiencies in considering other effects, which may have a significant impact on the absorption coefficient.

4.3 Optical Modeling and Design

Optical modeling and numerical simulations for both structure A and B was performed using the MoL. As stated in Chapter 3, the method of lines (MoL) is a good technique for generating accurate propagation constant while requiring a minimal computational effort. This is a result of the fact that the method is based upon a one dimension spatial discretization, while an analytical solution is applied along the remaining dimension. The method was used to determine the optical phase constant of the E_x^{11} and E_y^{11} optical modes supported by the devices as described in Figure 4.2 and Figure 4.4 and Table 4.1 and Table 4.2 above.

A TWPD will have semiconductor losses and possibly additional undesirable losses, as a result of the center signal electrode. The intentional semiconductor losses are introduced in the detecting layer to translate optical energy to microwave energy. This is the familiar optical absorption parameter (α_p) which is wavelength dependent, material dependent and doping dependent all of which were discussed in Chapter 2. Accurate characterization of both these losses is tremendously important in the design of TWPDs.

4.3.1 Modeling of Semiconductor Losses

Since we are dealing with a non-magnetic material the assumption is made that no losses will occur as a result of the permeability μ. Losses in general are represented mathematically by the superposition of dielectric and conductor losses. This is given by the imaginary part of the permittivity given as ε''-σ/ω. At optical frequencies the conductor losses can be considered to be negligible compared to the semiconductor losses. As a result the semiconductor losses will dominate the loss expression (i.e. $\omega \rightarrow \infty$, ε''-$\sigma/\omega \rightarrow \varepsilon''$).

The introduction of semiconductor losses has the effect of changing both the real and imaginary part of the dielectric permittivity. This is quantified in equation (4-2) and is related to the refractive index n in the usual manner (i.e. $n^2 = \varepsilon_r$).

$$\varepsilon_r(x) = n^2(x) - \frac{1}{4}\left(\frac{\alpha_p}{\beta_o}\right)^2 - jn(x)\frac{\alpha_p}{\beta_o} \qquad \textbf{(4-2)}$$

where $\beta_o = \omega / c_o$ is the phase constant of a plane wave propagating in free space, c_o is the speed of light in a vacuum given as 3.0×10^8 m/s and α_p is the absorption coefficient in a bulk medium.

In the optical modeling of structures A and B the semiconductor losses were taken to be entirely in the QW detecting layer. This is a reasonable assumption since the desirable losses in the detecting layer should be much higher than the semiconductor losses elsewhere in the dielectric material (i.e. $\alpha_{InGaAs} >> \alpha_{InP}, \alpha_{InGaAsP}$). Therefore, the real refractive index in the InGaAs material is replaced with a complex refractive index described by the square root of equation (4-2), where α_p is taken to be 1.16×10^6 m^{-1} at a free space wavelength of $\lambda_o = 1550$ nm[98].

4.3.2 Modeling of the Electrode

In order for us to accurately model the electrode at optical frequencies the question must be asked how does a metal behave at these frequencies? Fortunately, through prior work provided by Boardman et al. and others[93-94] on electromagnetic surface modes we know that at optical frequencies a metal behaves, and can be modeled accurately as a free electron gas or equivalently a cold plasma. The complex relative permittivity of such a medium is given by the following plasma frequency dispersion relationship[95-97].

$$\varepsilon_r = \left(1 - \frac{\omega_p^{\,2}}{\omega^2 + \nu^2}\right) - j\left(\frac{\omega_p^{\,2}\nu}{\omega(\omega^2 + \nu^2)}\right) \tag{4-3}$$

where ω_p, ν, ω, is the electron plasma frequency, effective electron collision frequency and the frequency of excitation, respectively. The above equation yields a negative value for the real part of ε_r when $\omega^2+\nu^2 < \omega_p^2$, which is the case for metals at optical communications wavelengths.

The electrode of interest in the detectors shown in the above Figures 4.2 and 4.4 consists of a blend of titanium (Ti), platinum (Pt) and gold (Au) metallization. At the time it was not known how accurate the characterization of the metallization must be, nor was it known how relevant it is to include the metallization in the model. Hence, for convenience and simplicity the electrode was assumed to be made entirely of gold (Au) for which we obtain using equation (4-3) an equivalent permittivity of $\varepsilon_{Au,r} = -72.336 - j15.702$ at a free space wavelength of $\lambda_o = 1.55\ \mu m$[98]. It will be shown later via computed propagation constants that top electrode in our designs is positioned far enough from the peak optical mode power to not affect the propagation of the latter.

4.3.3 Poynting Vector and Confinement Factor

Two important parameters that will be used in the analysis of the optical waveguide we the Poynting vector and confinement factor. The latter is used in the first order approximation of electrical bandwidth for TWPD provided in Chapter 2. The former is used in verifying the propagation constant and provides a visual tool for the field distribution.

4.3.3.1 Poynting Vector

The Poynting vector is presented here as opposed to the six individual field components for two reasons: compactness and physical relevance. The Poynting vector is not only used to confirm that the right root is found but is also used as a visual tool in the design of TWPDs.

A few important comments can be made regarding the field distributions and z component of the Poynting vector for the TWPD. Referring to the field for the rib waveguide presented in Chapter 3 Section 3.3.1 we expect the TWPD distribution to be similar since the structures are optically comparable. With this said, we note that the fundamental optical mode will have one extremum in both the x and y directions. We also note that the fundamental field component will also have a similar field distribution in the perpendicular direction. For example in the E_x^{11} mode there is one maximum in both the x and y direction for the E_x field component. Thus, we expect the H_y field component to have a similar distribution. Observing the field distribution for the rib waveguide shown in Figure 3.5 we conclude that this is indeed true. As a result we expect the z components of the Poynting vector to have a similar distribution as the E_x or H_y field components in the E_x^{11} mode. This occurs because the E_x and H_y field components are much larger than the H_x and E_y field in this mode. Thus, the z component of the Poynting vector defined as

$$S_z = \frac{1}{2}(E_x H_y^* - E_y H_x^*) \tag{4-4}$$

is closely approximated by

$$S_z \approx \frac{1}{2} E_x H_y^* \tag{4-5}$$

provided that the $E_xH_y >> E_yH_x$ which is generally true for the fundamental E_x^{11} mode in a rib waveguide. While the argument above is illustrated specifically for E_x^{11} mode the same can be stated for the E_y^{11} mode by replacing (4-5) with (4-6).

$$S_z \approx -\frac{1}{2} E_y H_x^* \tag{4-6}$$

Hence the use of the Poynting vector provides just as much information regarding the fundamental mode as all six electric and magnetic field components. For this reason the $+z$ component of the Poynting vector will be generated and presented here as opposed to the six individual field components.

The second reason for observing only the S_z component is physical relevance. That is, in general we are only concerned with the amount of power being delivered to some load. Hence, the power flow will occur in the propagation direction, in this scenario defined to be in the $+z$ axis. Thus, all other field components are less significant from this perspective.

4.3.3.2 Confinement Factor

Another important optical parameter is the confinement factor. This parameter gives the designer a measure of how much fractional power is carried by the core QW layer to the total complex power available. This is mathematically expressed as:

$$cf = \frac{\left| \iint_{QW} S_z dz \right|}{\left| \iint_{\infty} S_z dz \right|} \tag{4-7}$$

In equation (4-7), the numerator represents double integration over of the absorbing layer, in this case taken to be the QW or MQWs and the denominator is taken to be the integration of the total power propagating in the guide. It should be noted that the simplification provided in (4-5) and (4-6) can be applied to (4-7). These simplifications give an error of less than 0.01% in terms of the computed confinement factor in the case of the E_x^{11} and E_y^{11} modes in our structures.

4.3.4 Equivalent Slab Structures and Initial Guess

One of the main drawbacks of the MoL is that modes must be found by root searching in the complex plane. The equation generated by the MoL as a result of matching the tangential field components can only be solved via an initial guess for the propagation constant. If the initial guess is poor, the solution to the eigenfunction may converge to a higher order mode, hybrid mode or cavity mode, none of which is the desirable mode, generally taken to be the fundamental one. The first two solutions represent modes that exist in a TWPD however, they are often not the mode of interest. The cavity modes represent solutions generated as a result of enforcing boundary conditions and while physically realizable they are a result of the computational domain.

In order to generate a high quality initial guess for structures A and B, a slab waveguide with the same semiconductor layers as those described in Table 4.1 and 4.2 is analyzed. The slab waveguide is analyzed using the MoL for the TE_o mode only, neglecting the effects of the semiconductor losses and top center electrode on the effective index.

One can justify neglecting the semiconductor losses in the slab waveguide versions of structure A and B since the solution to the propagation constant found will only be used as an initial guess for the optical rib waveguide.

Table 4.3 shows the simulated results of the effective index and confinement factor for the equivalent slab structures corresponding to devices A and B. A reduction of 10^{12} in the value of the determinant is observed for the roots to the eigenfunction as compared to the initial guess.

Structure	TE_0	Confinement Factor
Structure A	3.286280405482080	1.64%
Structure B	3.248694763572332	1.81%

Table 4.3 Propagation constant for equivalent slab guide

4.3.5 Field Distributions Using the Poynting Vector

As mentioned previously a difficulty in working with numerical methods is the inability to determine if the propagation constant calculated corresponds to the fundamental desired mode. In order to confirm or deny the result, the field components or Poynting vector must be numerically generated. It is only through direct observation of the distributions that we can definitely state that the fundamental propagation constant has been determined.

The six field components are generated for the mode in Chapter 3 Section 3.2.10. Once it was determined that the fundamental mode had been obtained, the z component of the Poynting vector is generated. This is illustrated in Figure 4.7 and 4.8 for the equivalent slab structure corresponding to device A and B.

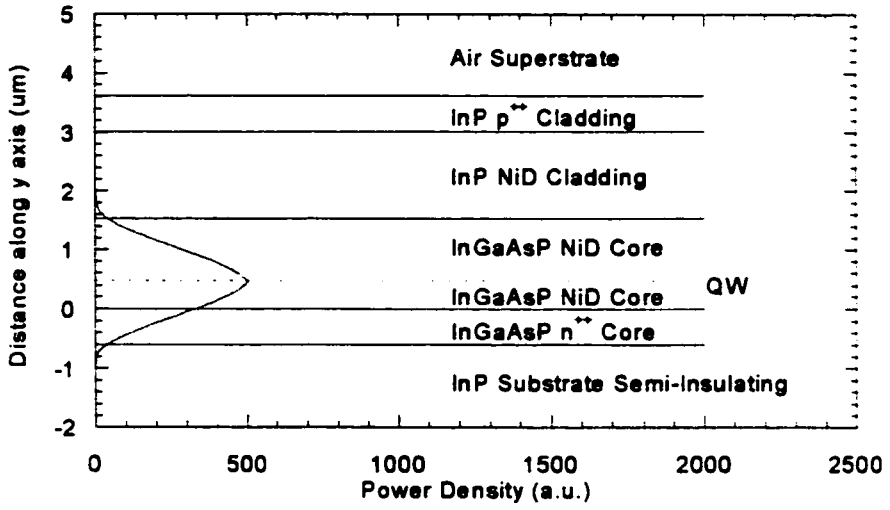

Figure 4.7 TE_0 slab mode profile for structure A

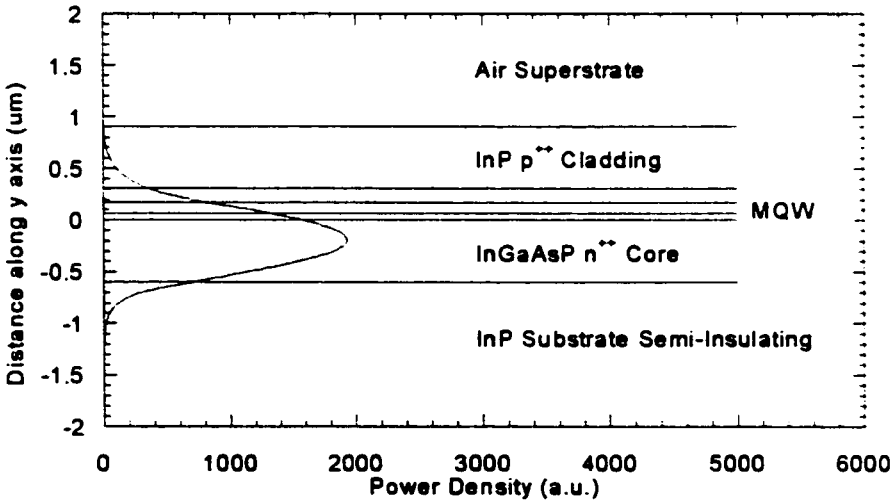

Figure 4.8 TE_0 slab mode profile for structure B

We observe from Figure 4.7 and 4.8 that the propagation constants calculated indeed represent the fundamental TE_0 mode for the equivalent slab guides. We also note that the peak of the QW(s) is placed near the mode maximum to optimize the efficiency of these devices.

4.3.6 Optical Rib Waveguide for TWPD

Referring to Figure 4.9 we see an illustration of the computational domain for structures A and B. We observe that these devices are modeled as open structures by treating the superstrate and substrate layers as being infinitely thick. Using the analytical solutions inherent to the MoL it is possible to prevent the boundary conditions on the top and bottom walls from affecting the mode profile. We also observe that the computational structure lacks the lateral electrodes that are present in Figure 4.2 and 4.4. This is a reasonable assumption since the electrodes are placed more than ten optical wavelengths away from the center electrode. Thus the ground electrodes will have a negligible effect on the optical waveguide. The center conductor cannot be neglected in the same manner since it is placed on top of the rib and must be considered in the operation of the device. The lateral boundary conditions are place more than seven free space wavelengths away from the rib. Physical half symmetry of the structure was exploited by placing a vertical electric or magnetic wall along the y axis to generate the desired E_x^{11} or E_y^{11} modes.

With the computational domain now defined we proceed in determining the propagation constant for the vertical and horizontal polarizations. This is done by using the value of γ found in the equivalent slab structure as an initial guess for the propagation constant for the TWPD structures.

Earlier it was stated that with these specific structures the top signal electrode had a negligible impact on the optical model profile. In order to show that the effect of the electrode is irrelevant to the propagation constant we first analyze the optical rib with the center electrode removed for both the vertical and horizontal polarizations. Then we analyze the structures with the center electrode present. In doing this we can definitely determine if the electrode has any influence on the propagation constants for both the vertical and horizontal polarizations. The results of this analysis are shown in Tables 4.4 and Table 4.5 for structure A and B along with Figures 4.10a–4.10h.

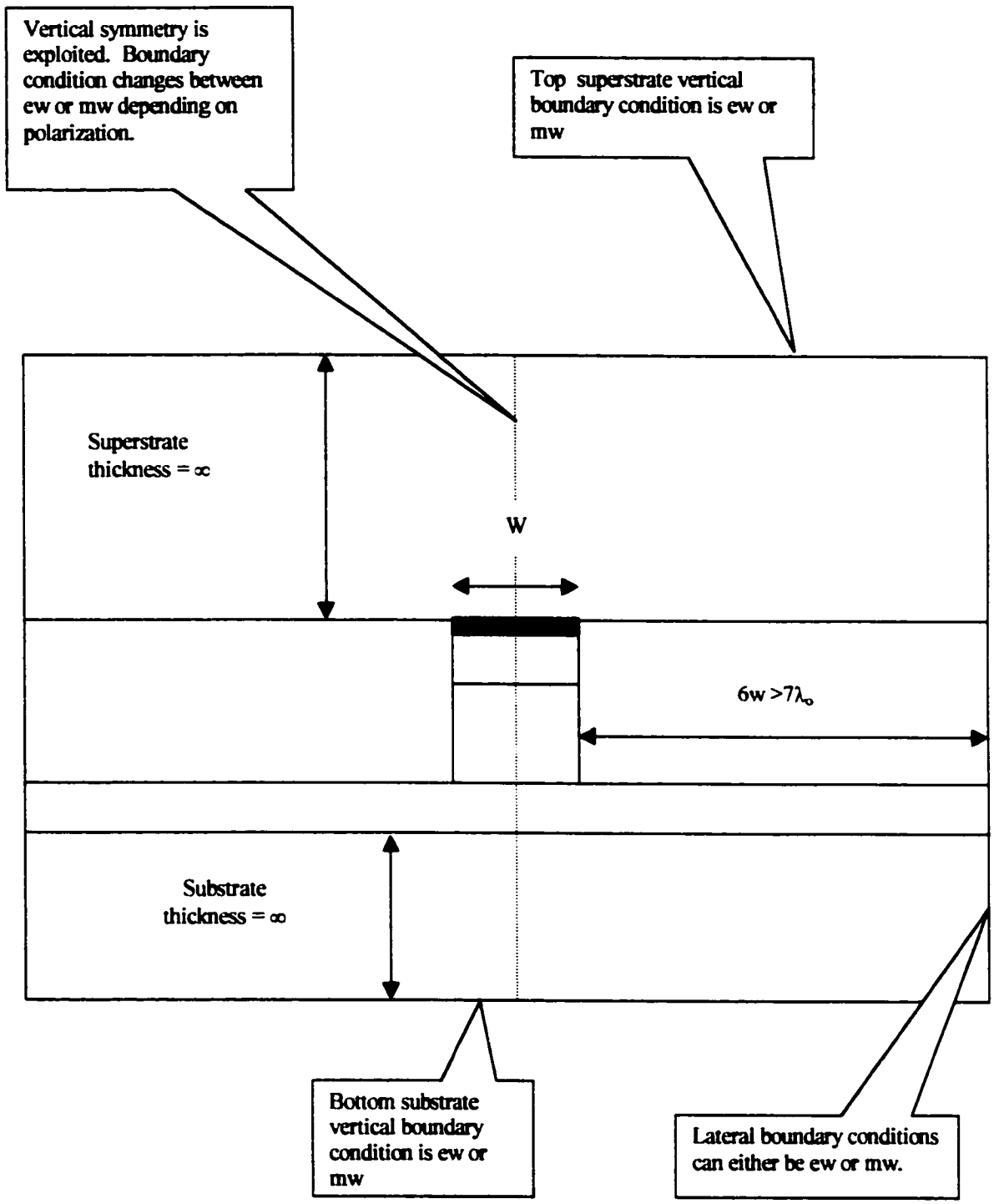

Figure 4.9 Definition of computational domain

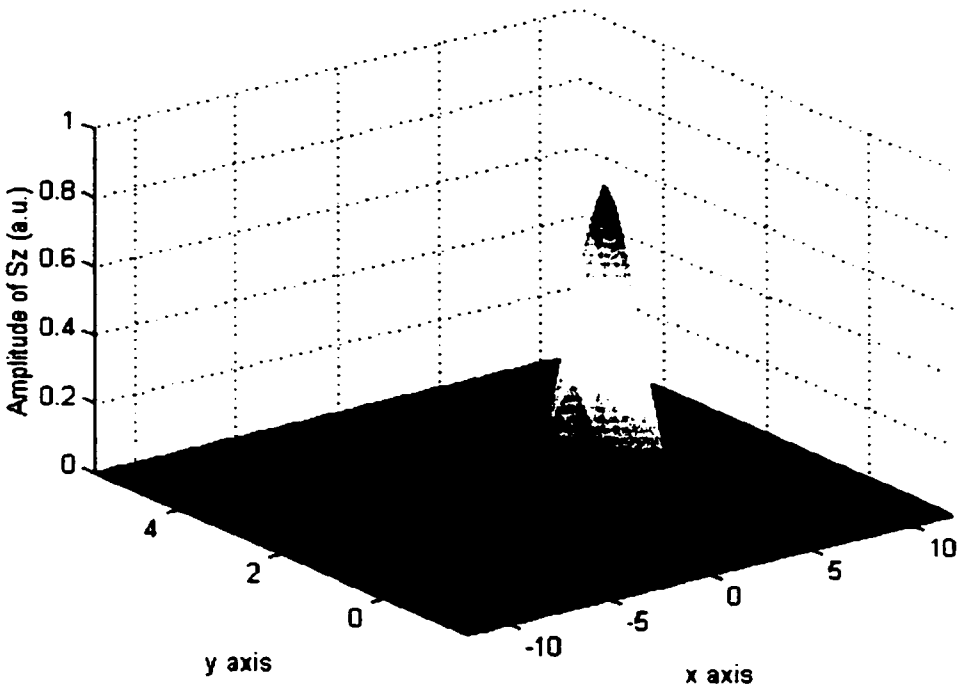

Figure 4.10a Power density distribution for structure A with electrode in E_x^{11} mode.

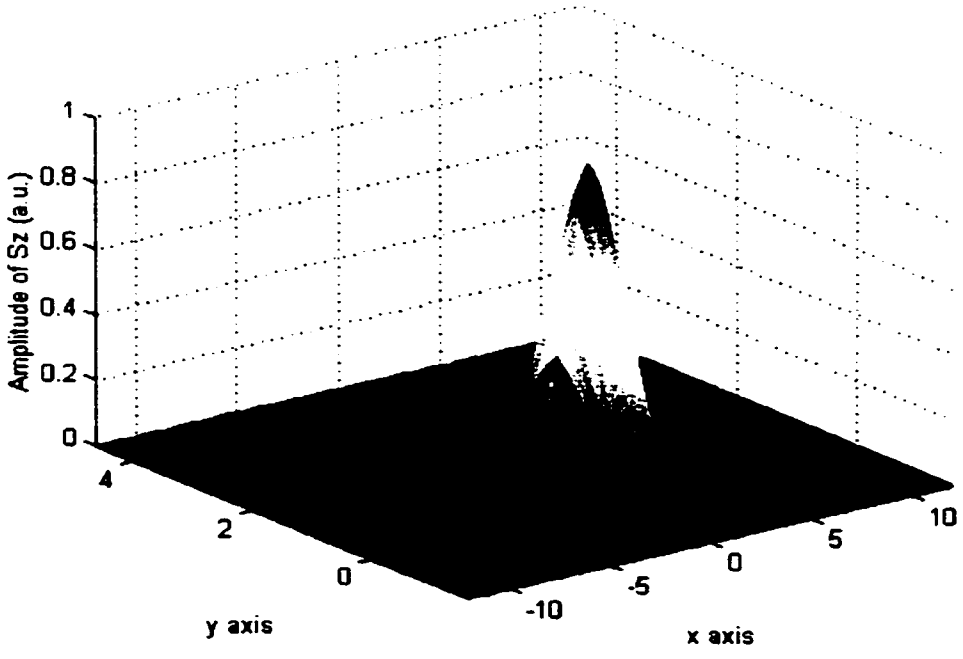

Figure 4.10b Power density distribution for structure A with no electrode in E_x^{11} mode.

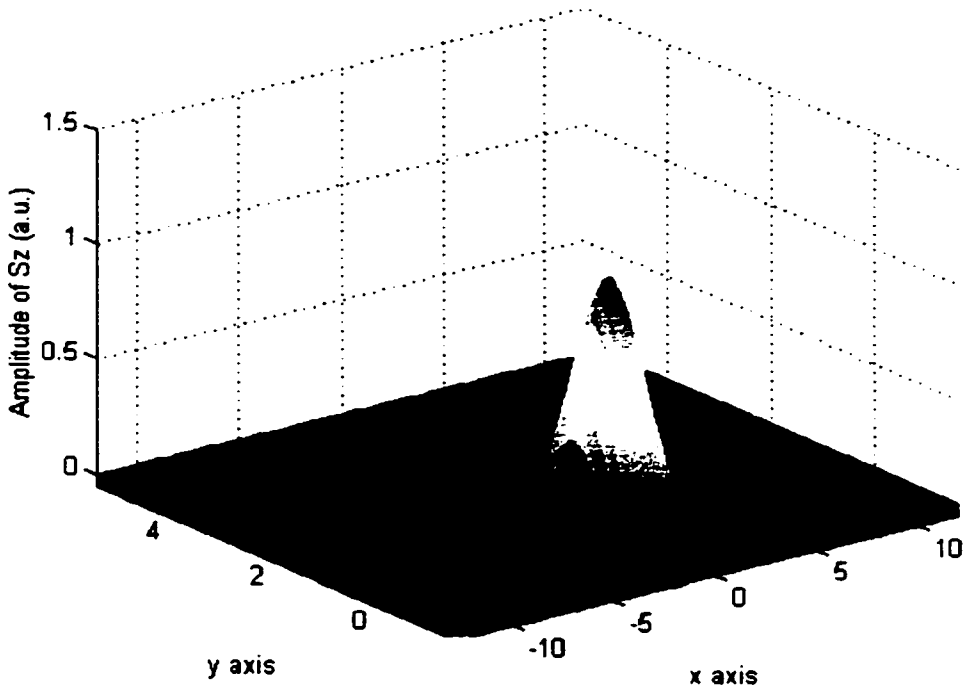

Figure 4.10c Power density distribution for structure A with electrode in E_y^{11} mode

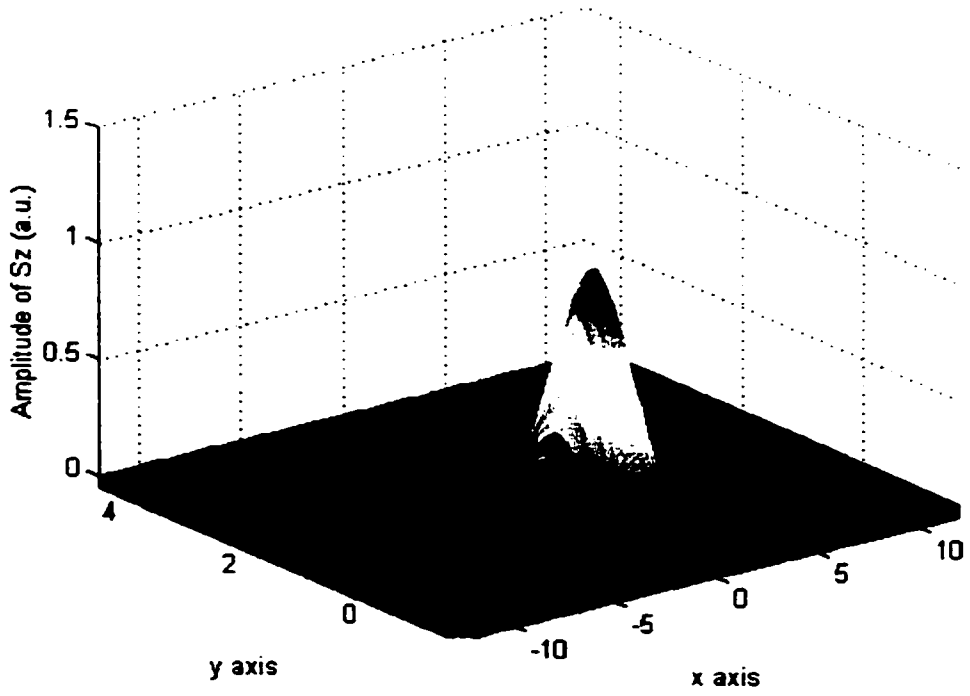

Figure 4.10d Power density distribution for structure A with no electrode in E_y^{11} Mode.

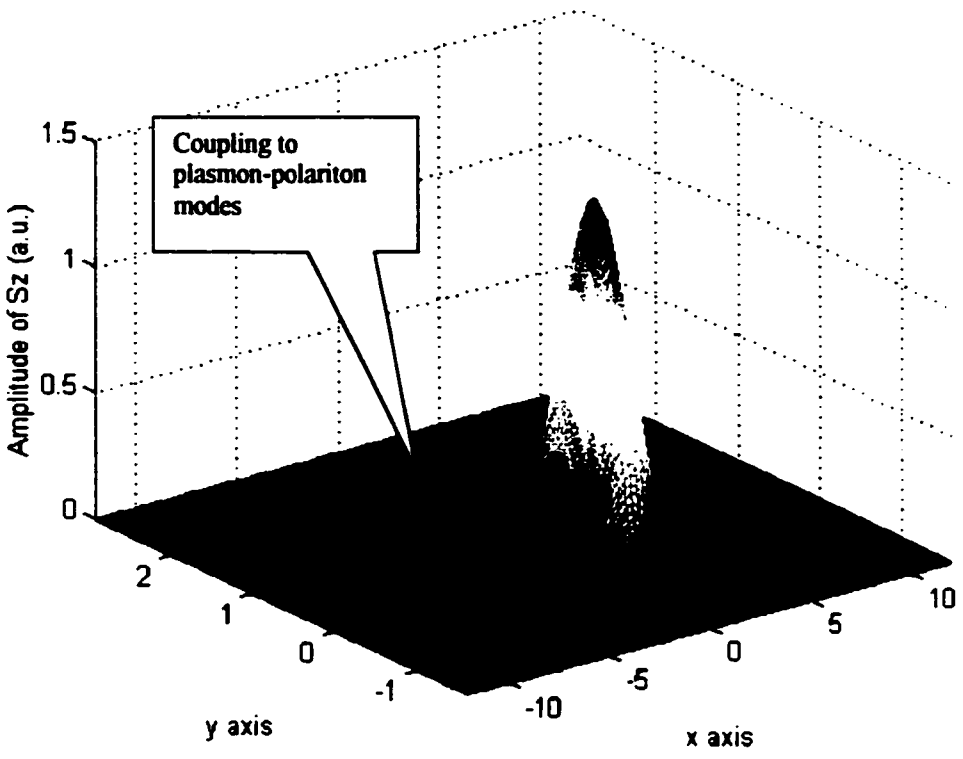

Figure 4.10e Power density distribution for structure B with electrode in E_x^{II} mode.

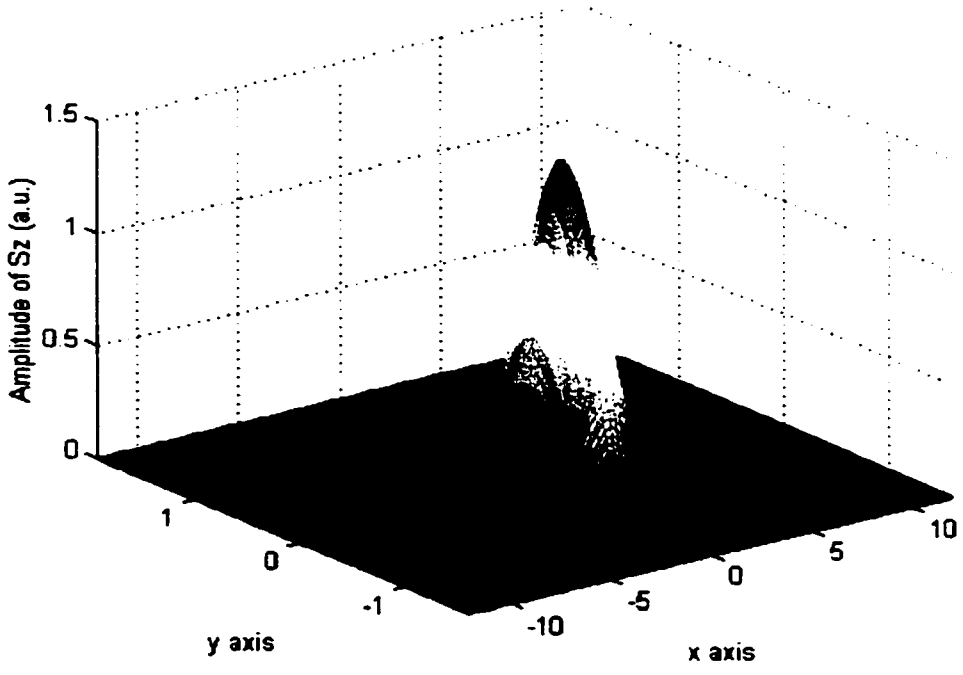

Figure 4.10f Power density distribution for structure B with no electrode in E_x^{II} mode.

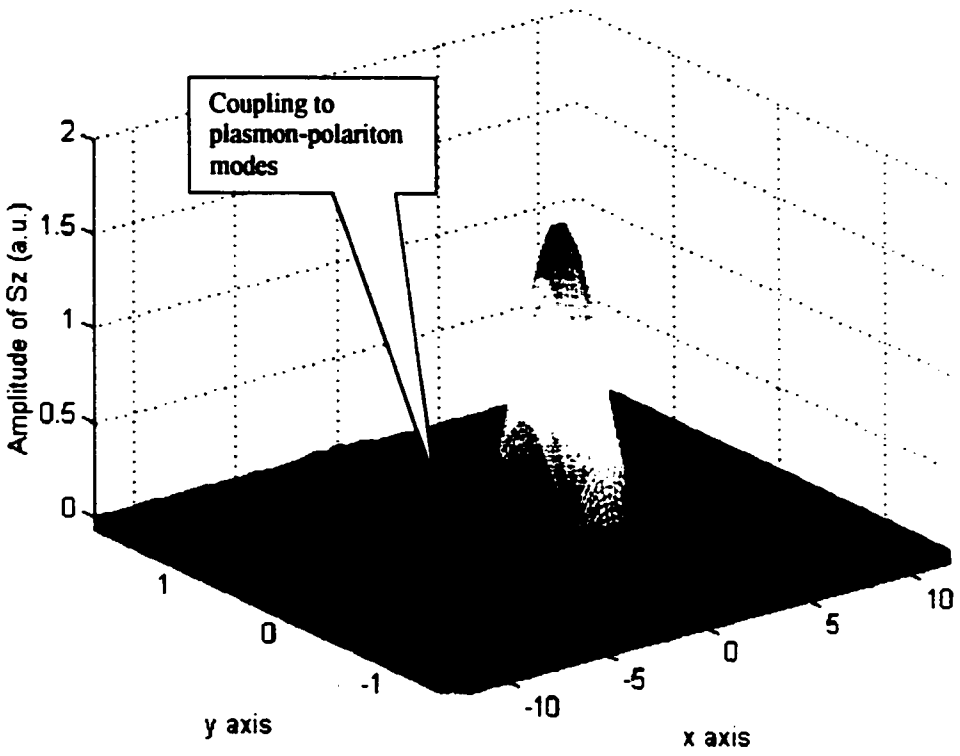

Figure 4.10g Power density distribution for structure B with electrode in E_y^{II} mode.

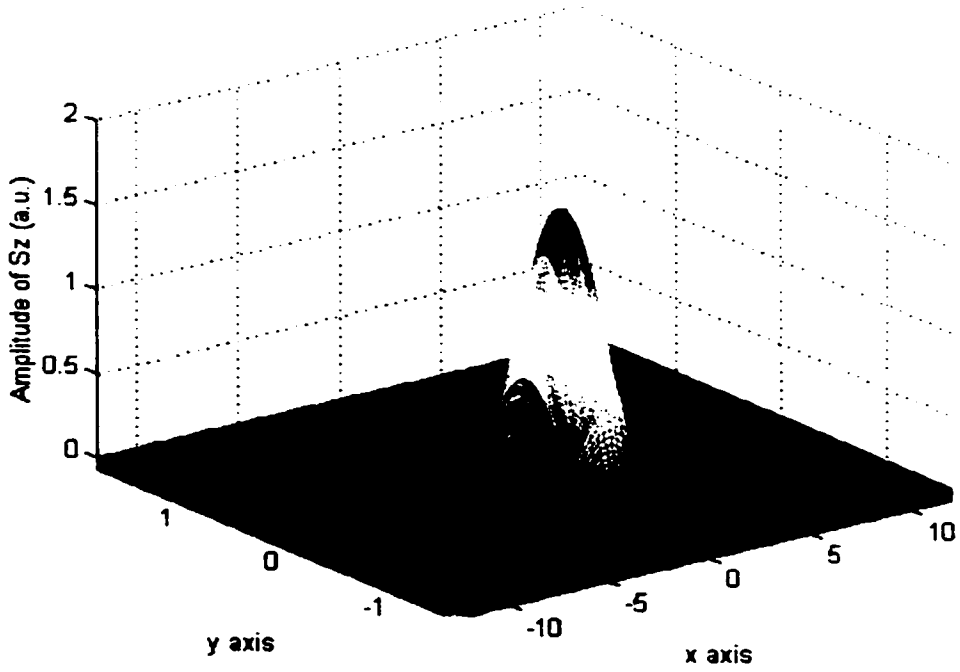

Figure 4.10h Power density distribution for structure B with no electrode in E_y^{II} mode.

Electrode	Mode	β/β_o	α/β_o	c.f(%)
no	E_x^{11}	3.283	2.437×10^{-3}	1.641
	E_y^{11}	3.276	2.429×10^{-3}	1.509
yes	E_x^{11}	3.283	2.437×10^{-3}	1.641
	E_y^{11}	3.286	2.429×10^{-3}	1.509

Table 4.4 Propagation constants for structure A

Electrode	Mode	β/β_o	α/β_o	c.f(%)
no	E_x^{11}	3.246	2.636×10^{-3}	1.791
	E_y^{11}	3.244	2.124×10^{-3}	1.585
yes	E_x^{11}	3.246	2.635×10^{-3}	1.795
	E_y^{11}	3.242	2.044×10^{-3}	1.540

Table 4.5 Propagation constants for structure B

Since these structure are optically very similar to a rib structure analyzed in Chapter 3 we expect the field distribution to be similar to those shown in Figure 3.7a to 3.7f. We also expect these devices to exhibit a similar dependency with polarization as seen in Figure 3.9.

Initially it was thought that the electrode must be included in the determination of the propagation constant since the proximity of the latter in relation to the extremum of the main electric field component will affect the optical profile. The reason for this idea was the fact that the maximum of the mode occurs in the QW region, thus one would expect the electrode to have an influence on both structures. One would also expect the metallization to have a greater effect on structure B due to the fact that the maximum of the mode profile is closer to the electrode in this geometry.

It has been reported and validated in Table 3.5 of the MoL chapter that the top center signal electrode for TWPD, in general, reduces the phase constant and confinement factors for both modes. It also increases the attenuation constant for the vertical polarized mode while decreasing the attenuation constant for the horizontally polarized mode. These effects have been attributed to the optical mode coupling energy into the electrode. This results in an excitation of metal modes or plasmon-polariton modes, which influences

the overall propagation constant. Some of these observations such as coupling to plasmon-polariton modes were observed for structure B, however, the results are small and do not significantly influence the propagation constant.

The results presented in Table 4.4 and 4.5 are exceptionally surprising. In addition to finding that these devices are practically polarization insensitive we also find that the phase constant and confinement factor change little from their equivalent slab waveguide counterparts. While this observation has only been made for the horizontally polarized mode if it were true for the vertically polarized mode, then any future designs would not require the rigor that has been presented here. In fact a simple transverse resonance program is all that is necessary to determine the propagation constant for the optical waveguide.

At first the results of polarization independence seem erroneous. We expect, and it has been reported that these devices are polarization sensitive. However, upon careful inspection of the waveguiding behavior of an optical rib we find that the polarization dependency of these waveguides is relatively small. At high frequencies the effective index becomes virtually independent of polarization. This is clearly illustrated in Figure 3.9 of the MoL chapter.

Another important design consideration is to ensure that optical absorption parameter is maximized over the waveguide's length of interest. This can be achieved by positioning the QW at the peak of the optical mode.

Figure 4.11 shows that fifty percent of the optical power is absorbed within approximately 25 μm of the waveguide for both structures, making the active length of these TWPD devices very short compared with the microwave wavelength. Even at 50 GHz where the microwave wavelength is in the millimeter range the absorption length is still much smaller than the electrical wavelength.

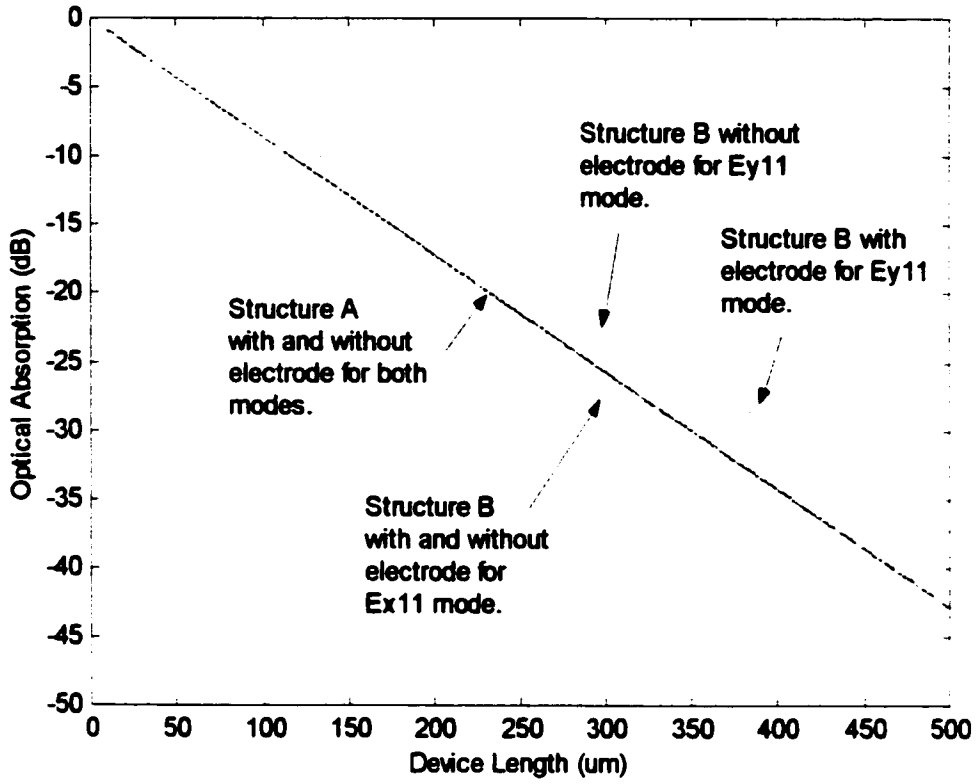

Figure 4.11 Optical absorption vs. device length

This agrees very well with the theory provided in Chapter 2. That is, TWPD are usually electrically very short and optically very long. Again this raises an interesting question that has previously been stated. If the devices are electrically very short and optically long, then where is the traveling wave effect? It is the hope once the devices are fabricated we can begin to resolve this lingering question empirically.

4.3.7 Higher Order Modes

It would be an incomplete discussion to talk about the optical design of the optical design of the TWPDs without discussing their modal operation as a whole. The two designs presented in Figures 4.2 and 4.4 do not exhibit single mode operation but are in fact multi-mode in nature.

Indeed, while designing structure B it was determined that the optical absorption coefficient for the fundamental mode was exceptionally low. It was observed that most of the absorption was occurring in a higher order mode. Thus, in order to increase the fundamental absorption coefficient a second QW was added.

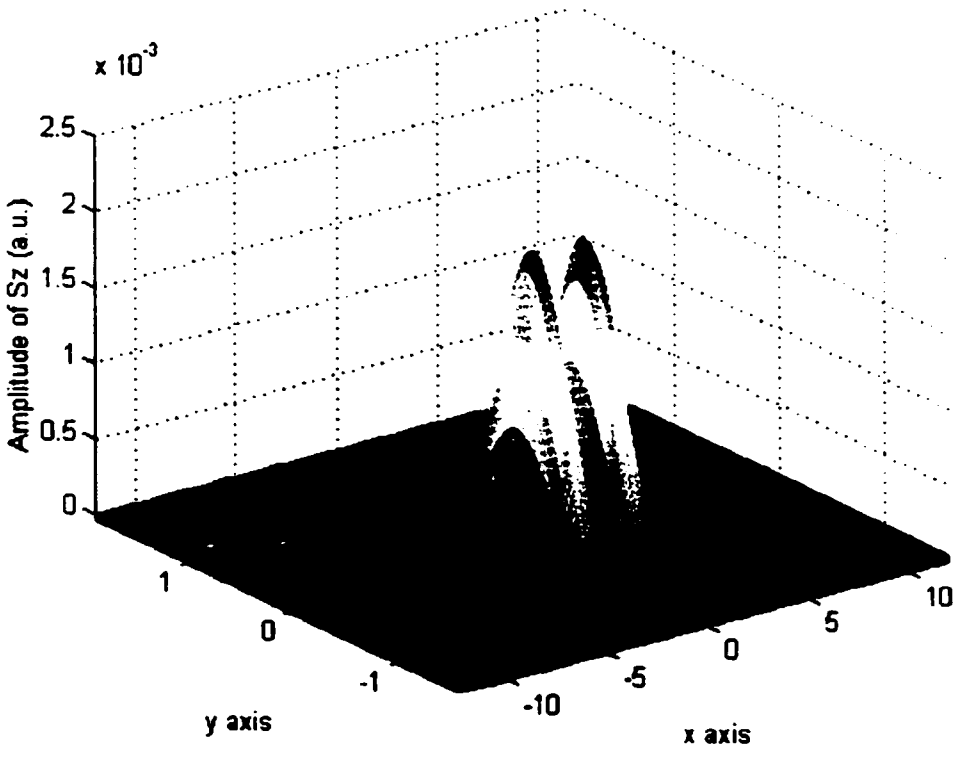

Figure 4.12 E_x^{21} mode for structure B with electrode present

On numerous occasions a propagation constant had been determined via the MoL only to discover later with the field distribution that it was a higher order mode. Such a scenario is illustrated in Figure 4.12 for structure B.

4.4 TWPD: Microwave Modeling and Design

Microwave modeling and design of the quasi-coplanar waveguide was accomplished using a commercially available CAD package based on the Method of Moments (MoM). It could have been also accomplished using the MoL with a minor simplification, however this was not done for the following reasons.

First the nature of the structure puts into question where the matching of the field components should occur. That is should the tangential fields be matched on the top signal electrode or on the two bottom ground electrodes? Only later was it determined that a simplification could be made to the computational structure such that a designer using the MoL is only required to match the transform tangential fields at the top signal electrode.

Second generating the dispersion curves is extremely tedious and time consuming. In fact curves like the ones seen in Figure 3.9 takes several days to generate and verify. It would have been necessary to do several iterations of this process since optimization of the structures is required. The time required to accomplish such a task ranges from several weeks to months before a final optimized design is submitted for review. Accurate and quick frequency sweep of the various microwave parameters such as impedance, effective permittivity etc. are very common in commercially available CAD. Several different device iterations can be accomplished in the span of one day, thus saving a tremendous amount of microwave design time.

Lastly, previous work on this structure using the MoL has shown that the indirect eigenvalue problem $det[G_{e,h}(\gamma)]$ becomes very unstable when it converges. This is due to a substantial difference between the microwave wavelength and the geometrical dimensions of the structure. Specifically, analyzing the structure in the microwave domain we are generally working with wavelength on the order of centimeters (cm) to millimeters (mm). However, the geometrical dimensions of the structure are given in micrometers (μm). This causes the minimum discretization distance h_{min} to be very small which results in the diagonal eigenvalue matrices $[\gamma_e^2]$ and $[\gamma_h^2]$ to be unusually large. This large argument is then passed to the *sinh* function creating an inherent instability in the indirect eigenvalue problem.

4.4.1 Semiconductor Simplifications to Microwave Design

In order to analyze the microwave waveguide several assumptions were made regarding carrier mobility, depletion width, reverse breakdown, leakage or dark current as they are related to doping concentrations and molar fractions.

Let us begin our discussion with reverse breakdown voltage. We know that the breakdown voltage is a function of the doping concentration, and critical electric field (i.e. $V_{BR} \propto N_A, N_D, E_{cr}$). The critical electric field is a physical constant, which is material specific. This value can be found in the literature for several different semiconductor materials. However, the numbers often reported deal with either bulk materials or specific heterostructures, none of which applies to our specific designs. The same difficulties can be stated for dark current (i.e. $I_o \propto A, n_i, W, \tau_o$), depletion width (i.e. $W \propto V_{bi}, N_A, N_D$), and carrier mobilities (i.e. $\mu_{p,n} \propto N_A, N_D$).

These parameters are important because not only do they determine the characteristic impedance, microwave phase velocity but also the ability to measure an electrical signal. In particular, if a designer is

not conscious of these parameters a photodiode may be fabricated in which the breakdown voltage is too low, or the dark current is too high. Both of which would result in an inability to measure the microwave signal.

Thus six assumption were made regarding the carrier mobility, depletion width, dark current, contact resistance, doping concentration and molar fractions. First the carrier mobility is taken to be $\mu_p = 150cm^2/Vs$ for holes and $\mu_n = 4600cm^2/Vs$ for electrons. These are the carrier mobilities for bulk InP with an intrinsic non-intentional doping concentration of $10^{15}/cm^3$. These carrier mobilities are used regardless of the InP alloys (i.e. InGaAsP or InGaAs). Second the intrinsic region is assumed to be equal to the depletion width. Hence, when strong reverse bias is applied to the intrinsic region it will be completely depleted of charge carriers. Third the leakage current is assumed to be small and not affected by carrier recombination, surface states or carrier lifetimes. Fourth the contact resistance is not modeled and assumed to be negligible. The last two assumptions made are that neither, doping concentration or molar fractions significantly affect the above parameters. Strictly speaking none of the above assumption are valid, but these simplifications are reasonable and justified to allow for a first design iteration of the detectors.

4.4.2 Microwave Waveguide Design

With the above semiconductor simplifications stated, we can now proceed with the microwave design by making use of:

$$\sigma = q\mu_p N_A + q\mu_n N_D \tag{4-8}$$

A description of the assumptions made can be found in Table 4.6. These semiconductor assumptions were applied to both structures A and B.

Material	Doping type and mobility	N_A, N_D provided by grower (cm^{-3})	Values used (cm^{-3})	σ values used (S/m)
InP	p^{--} $\mu_p = 150\ cm^2/Vs$	2.0×10^{18}	2.0×10^{18}	4806
$InP/InP_{0.53}Ga0._{47}As/$ $In_{0.80}Ga_{0.20}As_{0.43}P_{0.57}$	NiD	5.0×10^{15}	0	0
$In_{0.80}Ga_{0.20}As_{0.43}P_{0.57}$	n^{--} $\mu_n = 4600cm^2/Vs$	2.0×10^{18}	2.0×10^{18}	147384
InP	S.I	1.0e9	0	0

Table 4.6 Microwave values

For both structures the rib was modeled as an inhomogeneous layer with the values of permittivity seen in Table 4.1 and 4.2 and the assumptions described in Table 4.6. The metallization is assumed to have a finite thickness of 1 μm with a conductivity equal to that of gold $\sigma = 4.10 \times 10^{7}$ S/m.

We have already discussed in Chapter 2 that the microwave portion of this guide is very similar to an MIS structure. It is well known that these structures support a slow wave mode of propagation. The basic and absolute condition for a structure to support a slow wave mode of propagation is that the structure must provide a separate storage of electric and magnetic energy in either the axial or transverse directions. In this case the depletion region in the p-i-n detector provides the necessary separation of electric and magnetic energy. The low impedance doped semiconductor which is a nonmagnetic material is virtually invisible to the H-field as it propagates down the guide, while the E-field is highly confined in the depleted intrinsic layers between the p^{--} and n^{--} contacts.

The same effect that causes the slow wave mode of propagation is also responsible for these structures having effective permittivities that can be larger than the permittivities of the individual materials. That is, normally we expect the effective permittivity to fall between the two extreme permittivities. In this case air and the highest permittivity of the structure, InGaAs (i.e. $1<\varepsilon_{r,eff}<13.9$). Once doping is taken into account the effective permittivity actual falls between , $1 < \varepsilon_{r,eff} < |\varepsilon_r - j\sigma/\omega\varepsilon_o|$. It is this doping that generates the depletion layer and hence causes the condition for slowing the electrical wave.

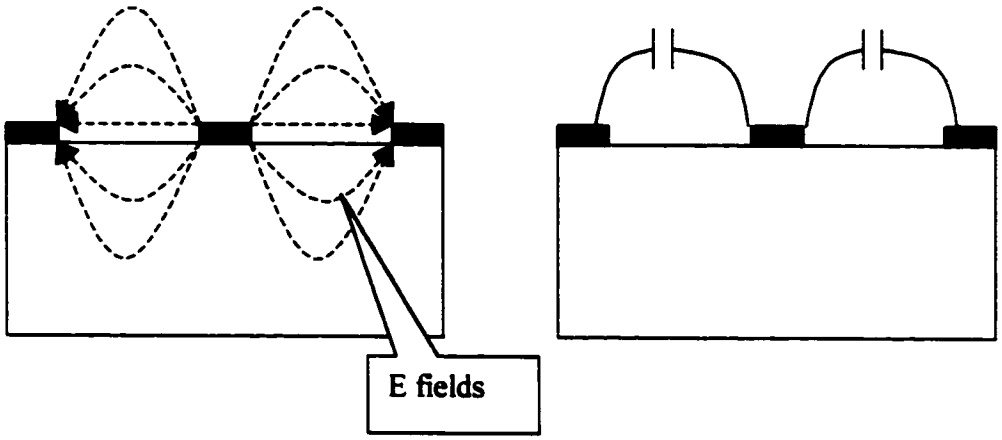

Figure 4.13 CPW electric fields

Referring to Figure 4.13 we see that the characteristic impedance and phase velocity of a typical coplanar waveguide is determined by the capacitance between the center signal electrode and the two adjacent ground electrodes. Viewing the TWPD one would believe that the characteristic impedance and phase velocity is also determined by the separation between the center electrode and the two ground electrodes however, such is not the case.

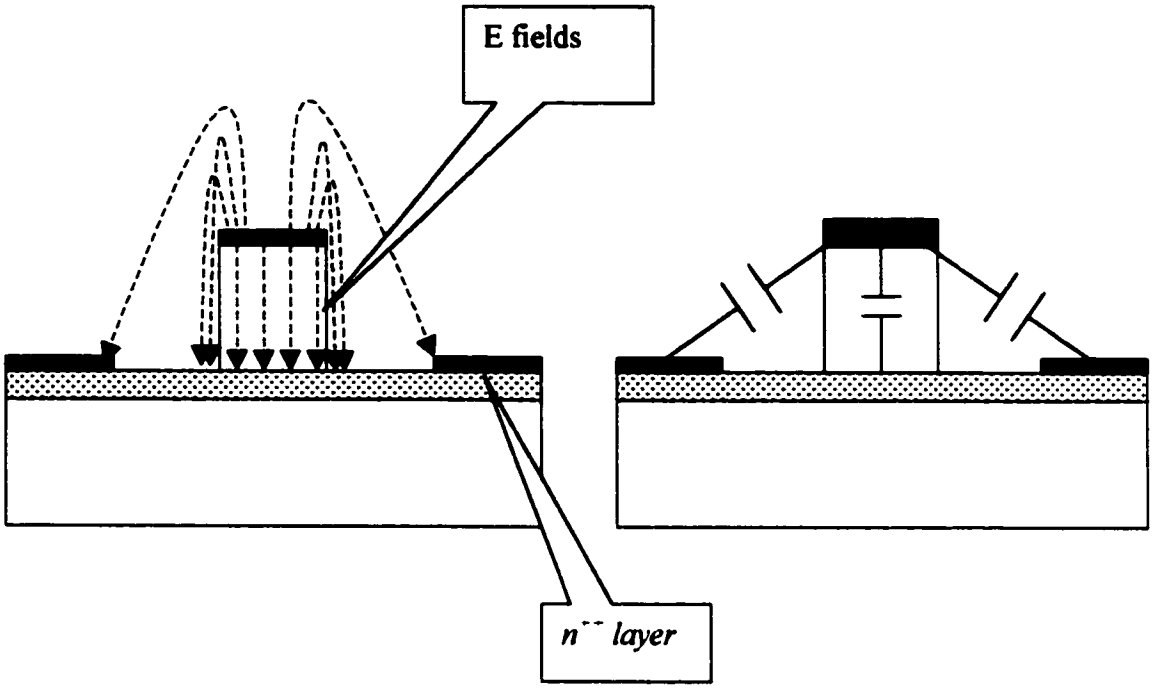

Figure 4.14 TWPD electric fields

We noted from the semiconductor layer design that most of the capacitance was found to reside within the depletion region and not between the signal and ground electrodes. This is clearly illustrated via the electric field distribution shown in Figure 4.14. Comparing Figure 4.14 with the electric field distribution for a microstrip line shown in Figure 4.15, we observe that the electric field behavior is very similar to that of a microstrip. The difference arises as a result of the two ground electrodes. That is the two ground electrodes cause the magnetic field distribution to be very similar to that of a coplanar waveguide. As a result, the effect of the two ground electrodes on the characteristic impedance of a TWPD is purely secondary. This effect can be a primary concern if the n^{++} and p^{++} layers are not heavily doped or the n^{++} and p^{++} layers are switched in the above design.

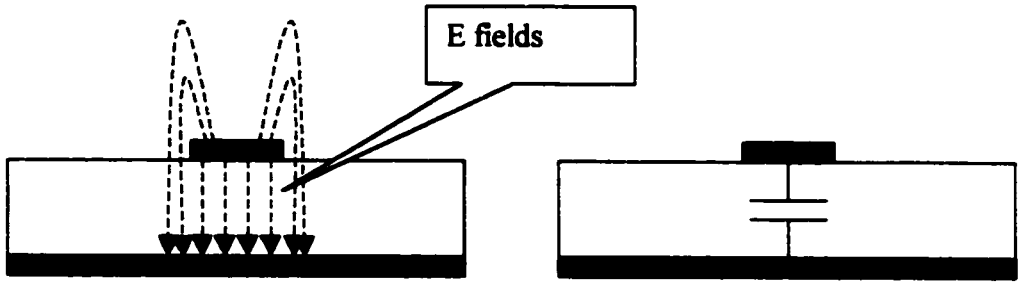

Figure 4.15 Microstrip electric fields

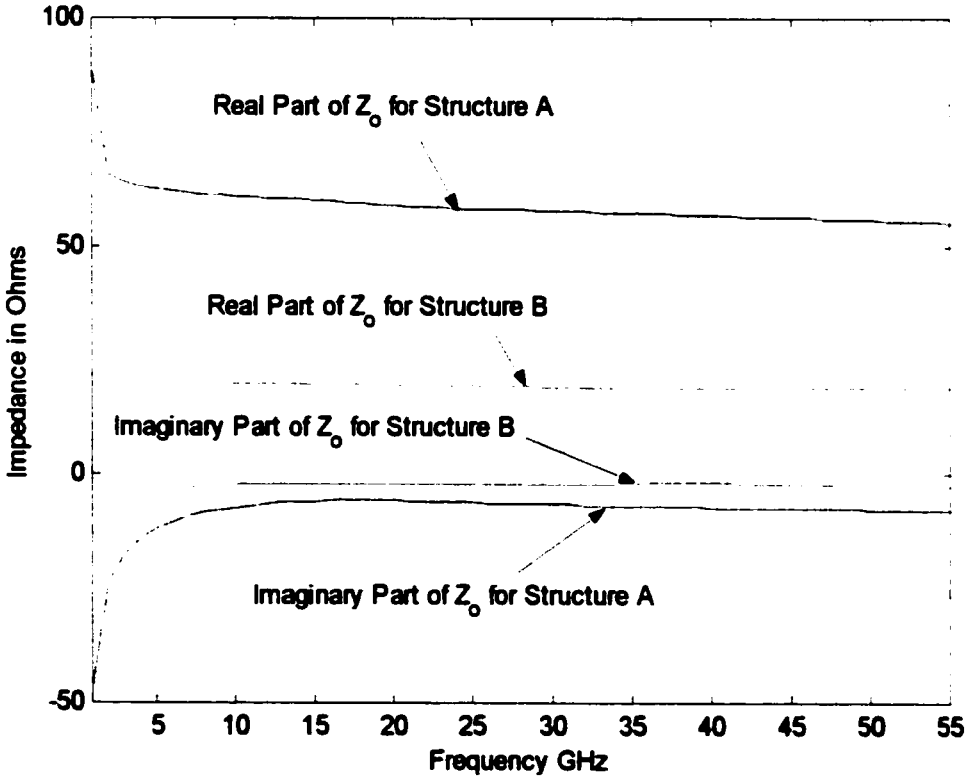

Figure 4.16 Characteristic impedance vs. frequency for structures A and B

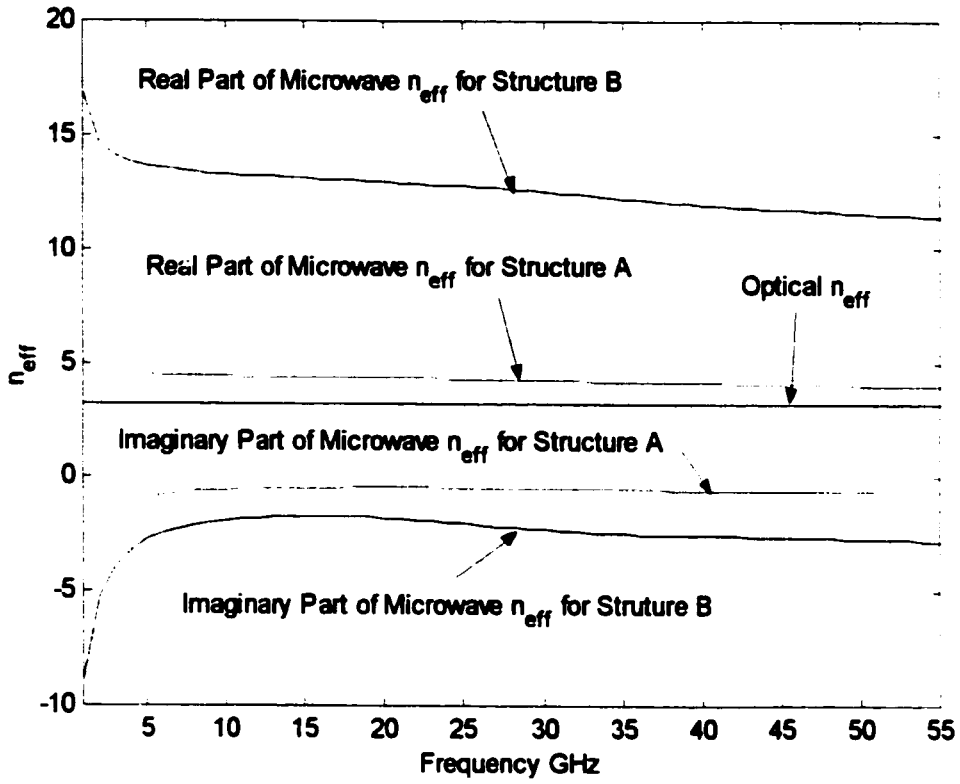

Figure 4.17 Microwave effective index vs. frequency

In keeping with our two separate design philosophies for structures A and B. We observe from Figure 4.16 that a characteristic impedance of approximately 50Ω has been obtained for structure A. While as expected for structure B the impedance is numerically different from 50Ω.

Figure 4.17 shows the microwave effective index as compared to the optical effective index under strong reverse biasing. As expected we see phase velocity matching between the optical and microwave signal for structure A and velocity mismatch for structure B.

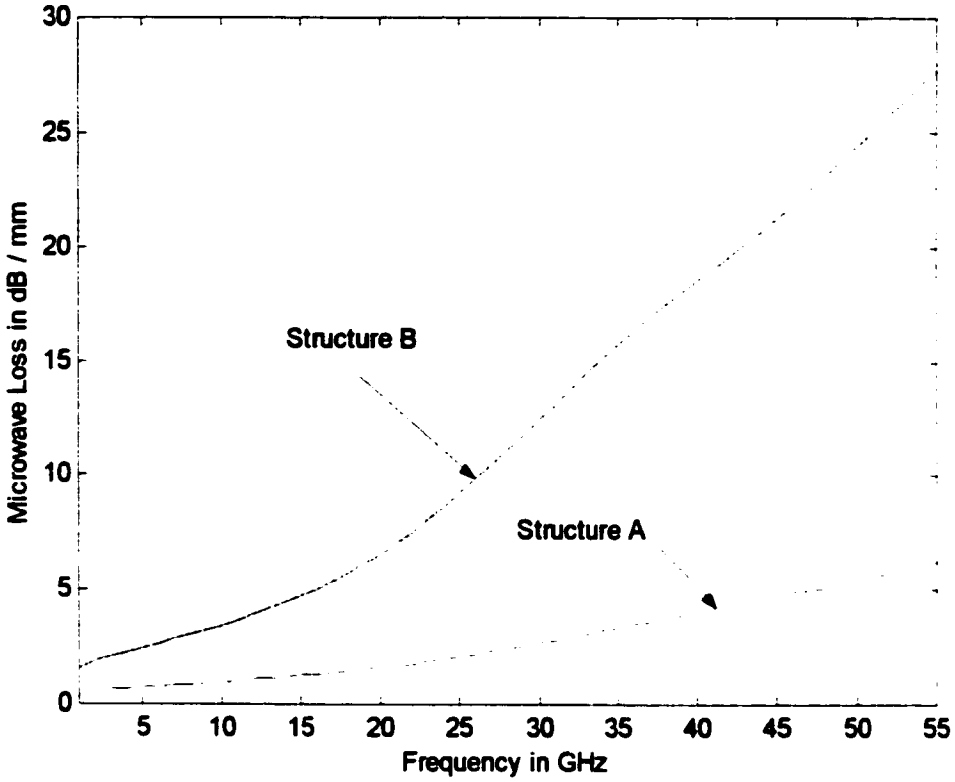

Figure 4.18 Microwave loss vs. frequency for structure A and B

We observe in Figure 4.18 the microwave loss in dB/mm as a function of frequency. Again we observe the loss has been minimized for structure A while structure B remains unoptimized. The loss at 55 GHz is 7 dB per mm for structure A, which gives 3.5 dB of attenuation for a 0.50 mm long device.

Using equation (2-37) we calculate the microwave bandwidth as a function of effective index. This is illustrated in Figure 4.19 and 4.20 for E_x^{11}, E_y^{11} modes for structure A and B respectively.

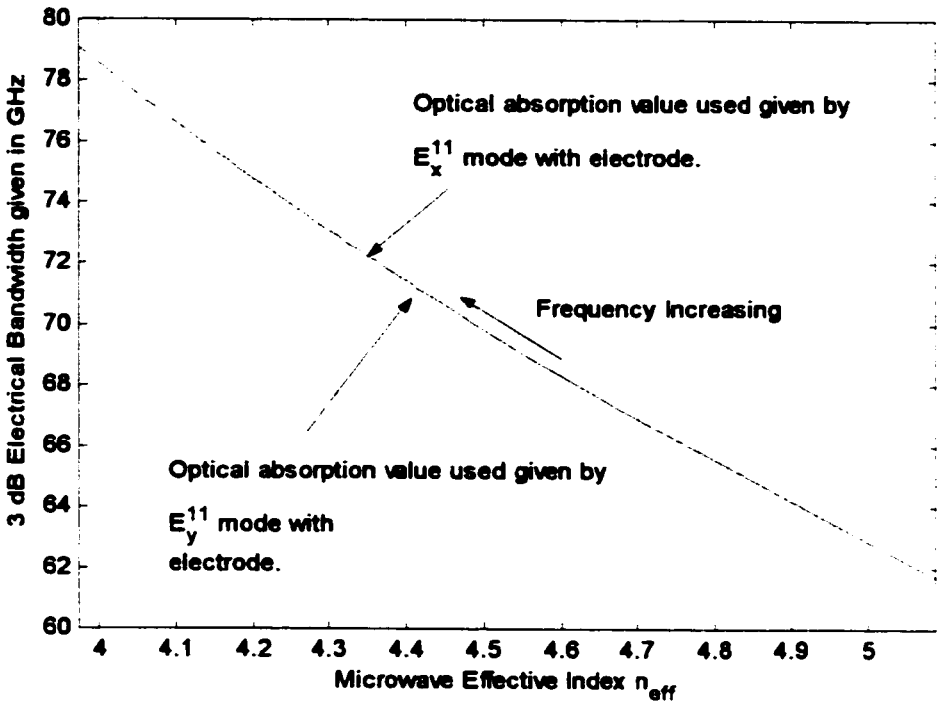

Figure 4.19 Microwave bandwidth vs. microwave effective index for structure A

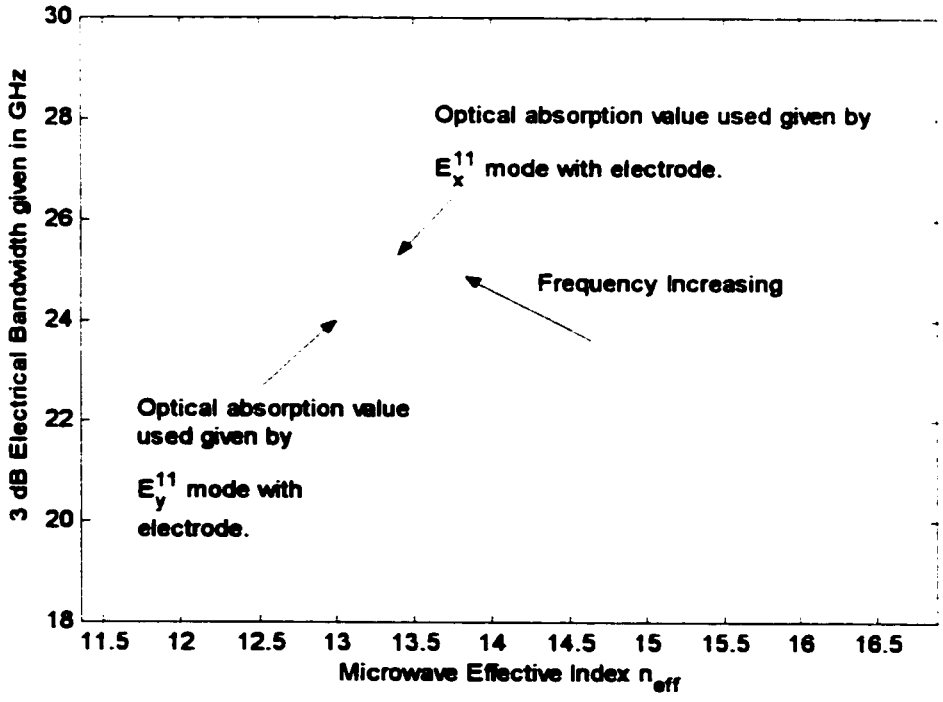

Figure 4.20 Microwave bandwidth vs. microwave effective index for structure B

According to Figure 4.19 and Figure 4.20 structure A should have the larger bandwidth. However, the derivation presented in Chapter 2 does not include any effects due to transit time. For example optimizing structure A for 50 Ω and velocity matching required an increase in the height of the ridge to change the capacitance hence, with it a change in the impedance and phase velocity. However, as a consequence of increasing the rib height to meet these criteria the transit time should increase making device A inherently slower. Such a result is not reflected in the Figure 4.19. Thus we can state, that it is not possible, with the present derivation, to calculate with any degree of certainty the theoretical bandwidth of the device. As a result of this uncertainty several different device geometries were attempted in the mask design.

4.5 Mask Design and Layout

Obviously tremendous care has been taken in the optical, microwave and semiconductor modeling and design. Where possible the utmost rigor has been considered. Despite this, assumptions and simplifications have been made in all three designs for both structures. Coupled with these assumptions are the fundamental limitations of the foundry.

Specifically there are certain limitation in terms of alignment tolerance, etch depth, contamination etc. that a designer has no control over and must accept as part of the fabrication abilities of the foundry. These limitations are illustrated in Figure 4.21 for the devices in this thesis. Such issues may be irrelevant in the design of TWPDs or they could be extremely important, however, only the measurement can determine definitely either way.

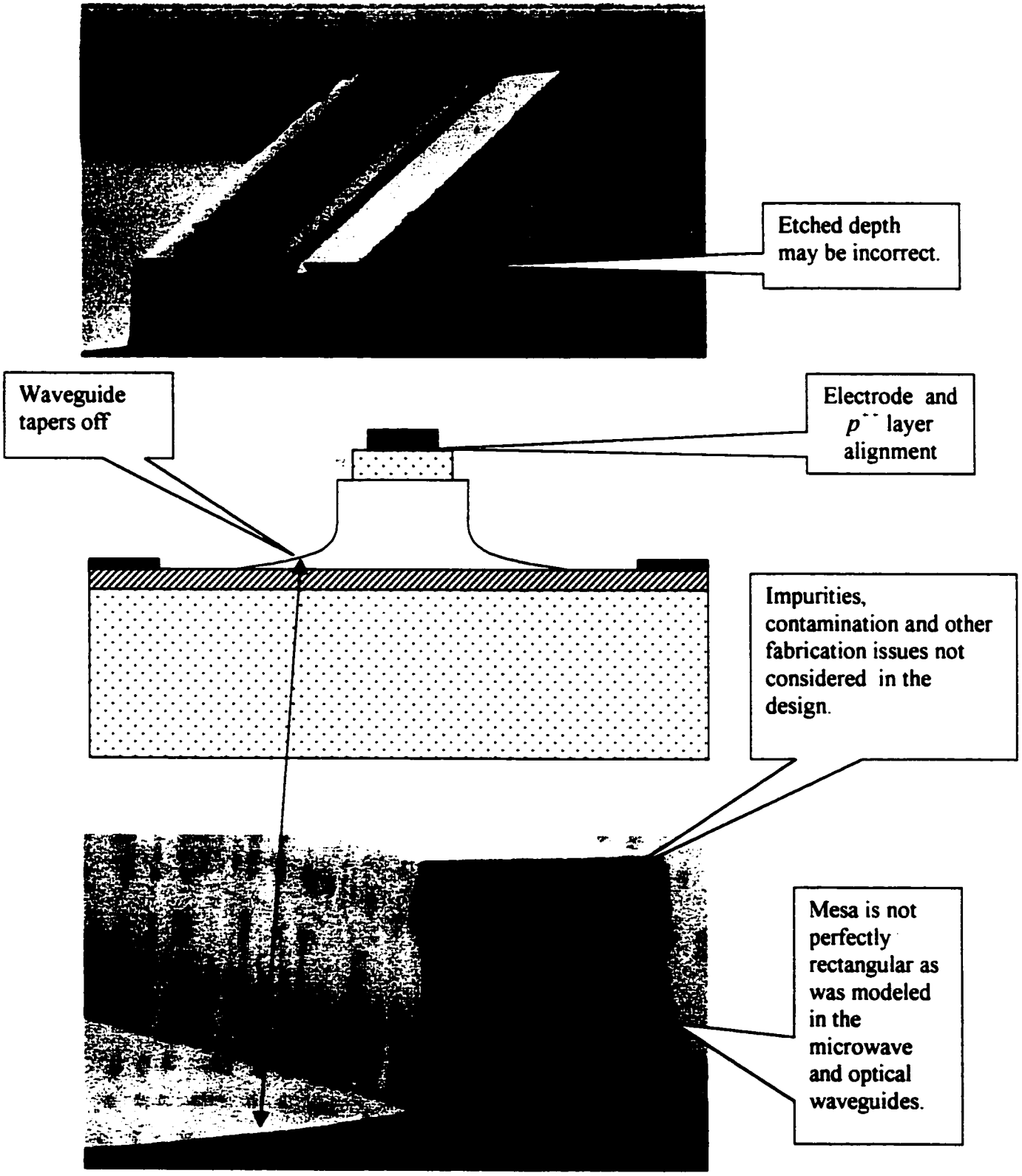

Figure 4.21 Examples of for fabrication issues

The optical and microwave simulations used perfectly rectangular blocks to simulate these guides. However, it is clearly visible in Figure 4.21 that the mesa layer is not rectangular. In fact, in reality, the deeper the mesa, the more error that can occur in terms of the etched depth and the mesa being rectangular.

Prior to the work on TWPDs the Communication Research Center had not etched a mesa beyond 1 μm in depth. The etch rate for the reactive ion etch (RIE) chamber is approximately 1 μm in 20 minutes. In order to achieve an etch depth of 3.61 μm the RIE chamber could need to be active for well over an hour. Leaving the chamber active for this long would cause severe process contamination. Hence, in order to mitigate this problem the sample was etched for 20 minutes, then removed, and the RIE chamber cleaned. The process was repeated until a mesa depth of 3.61 μm was achieved. The sheer act of turning off the chamber, removing the sample and placing the sample back into the chamber introduces errors in the alignment and etched depth. Therefore, one would naturally expect more error in terms of etched depth to occur in structure A than structure B.

As well in the simulation of these two guides, perfect alignment was considered between the waveguide layer, p^{--} layer and the electrode. This is beyond the abilities of the foundry and an error of up to 1 μm must be accepted in the alignment of these layers. If this tolerance issue is not considered in the mask design then during the alignment process the p^{--} contact can droop over the mesa making contact directly with the n^{--} layer hence, shorting the diode. Thus in keeping with this tolerance the p^{--} layer and electrode widths are decreased by 1 μm on either side.

It is under this atmosphere of unknowns that the mask design takes place. The layout considered 100 different device geometries. Varying such parameters as the signal ground spacing, width of the ridge, length of the device. The wide variation of device geometries was designed not only to maximize measurement success but also to validate, or dispute theory. Figure 4.22 shows the mask design with the various device geometries.

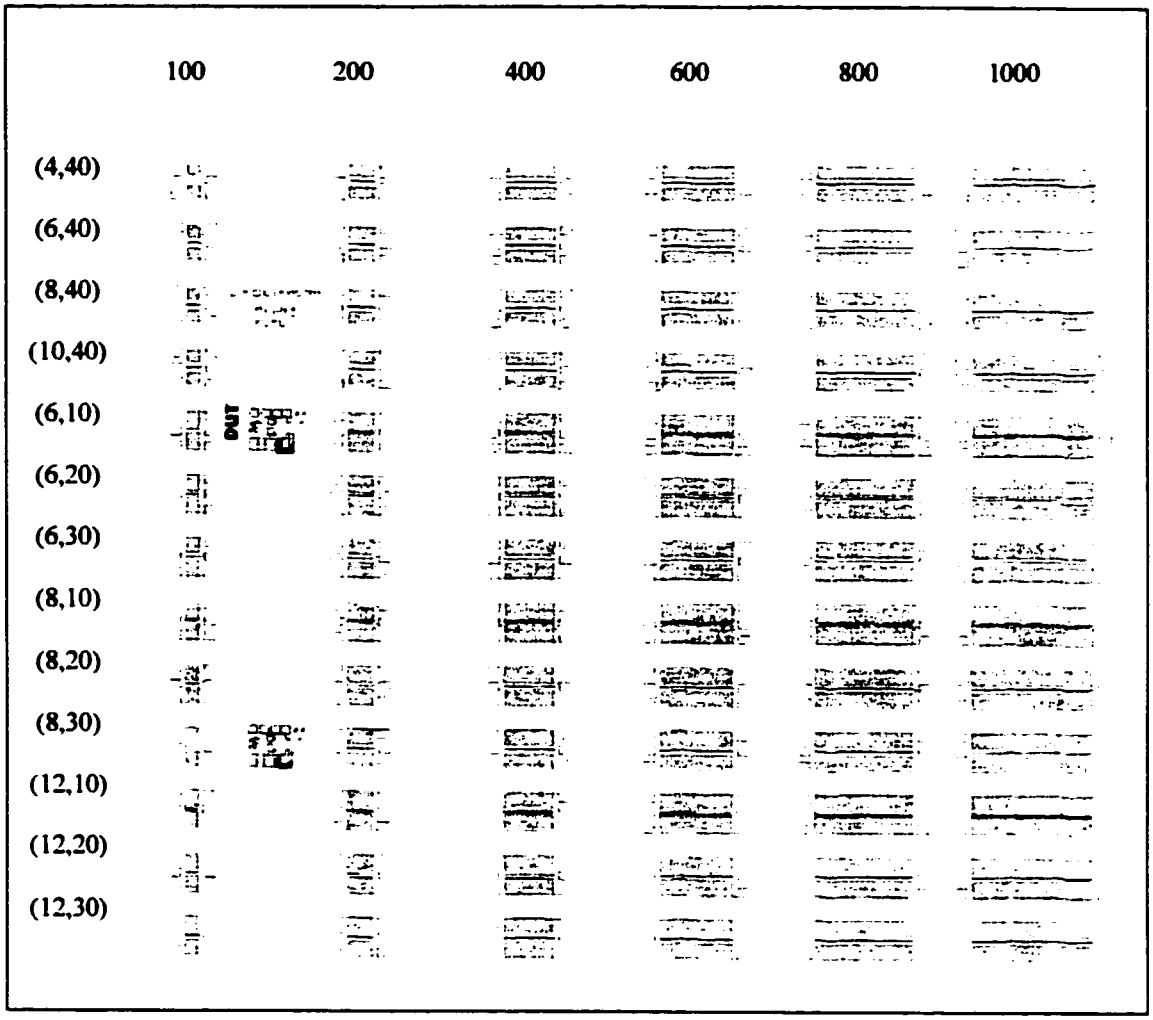

Figure 4.22 Layout of mask design

All dimensions are given in μm. The notation given on the left hand side of Figure 4.22 represents the width of the electrode followed by the signal ground spacing. The top notation represents the length of the device.

Shown in Figure 4.23 is the final wafer with the p^{--} contact, n^{--} contact, mesa and first level metal present. The array of TWPD detectors is clearly visible along with the pads where the probes will come down to make electrical contact.

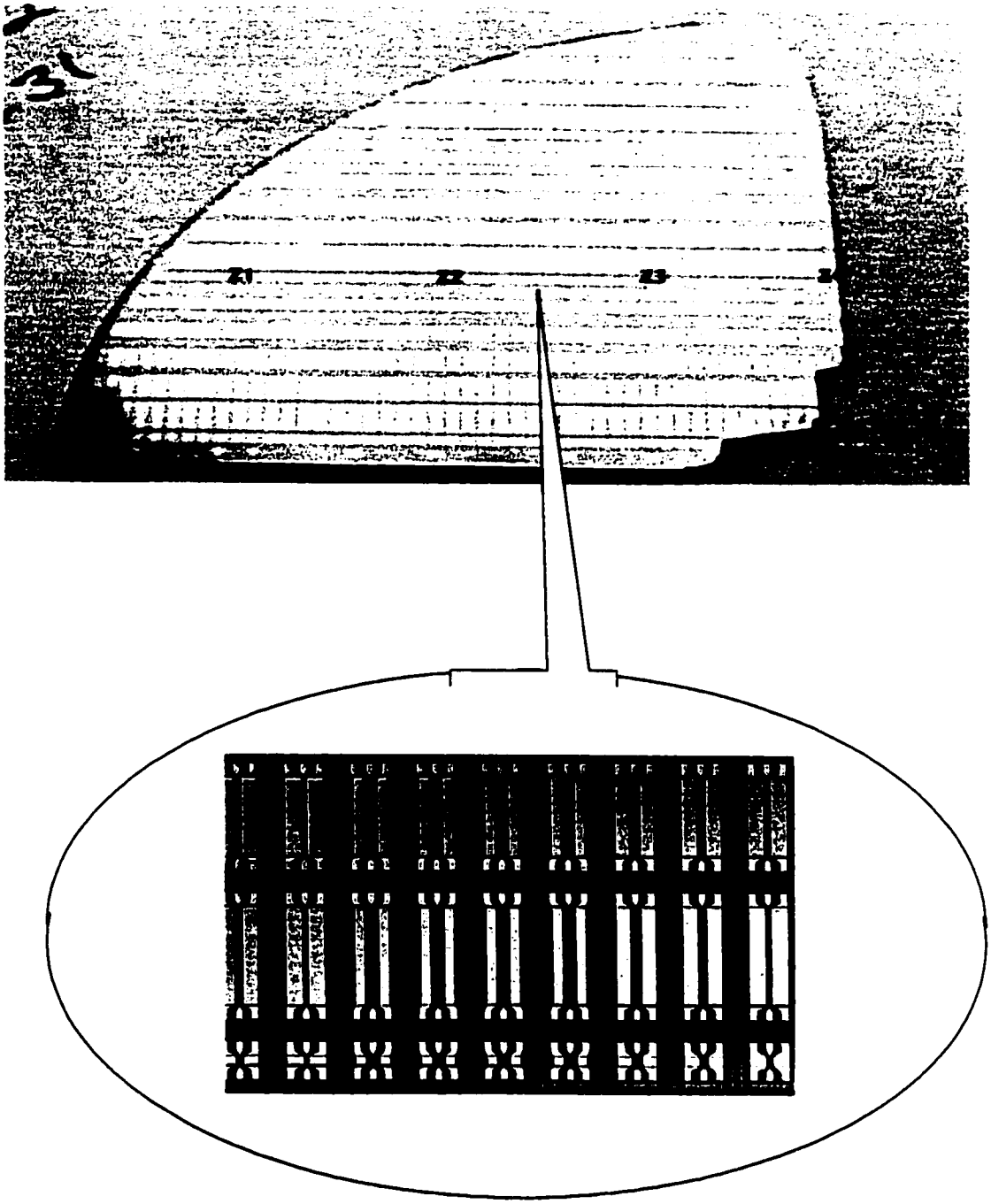

Figure 4.23 Fabricated wafer and array of TWPD

In summary what has been presented are the simulated designs for two structures. A final mask design and the corresponding unknown parameters.

Chapter 5 Measurements and Analysis

Theory, design, simulation and fabrication culminate in the measurements. Ideally the measurements should identify both the successes and shortcomings of the development. Practically this is often difficult since observing individual effects in a measurement is rare. Often the differences between the theory and the measurements are a result of a multitude of parameters interacting with each other in ways that a designer has not considered and does not expect. All the TWPD measurements are broken down into three sections:

- DC Measurements
- Optical Measurements
- Microwave Measurements

Obviously, there exist a potential to generate a tremendous amount data given the two layer structures and the various device geometries however, this would take us away from the original goal of the work. Recalling that the key advantage of using a TWPD detector over a conventional VPD is the inherent trade between bandwidth and efficiency present in all conventional detectors. Thus while other measurements are presented for completeness the emphasis of the measurements shall be placed on the microwave bandwidth and quantum efficiency or equivalently responsivity.

Each section will begin with an explanation of the measurement setup where appropriate, followed by the presentation of the results obtained for specific TWPD geometries for both designs. The results of which are compared and discussed against theory.

5.1 DC Measurements

All measurements taken in this section occur while no modulation is present on the laser. These measurements will characterize such important p-i-n junction diode parameters as the responsivity, dark current, breakdown voltage, forward bias voltage and linearity. These parameters give valuable information regarding the process development of the diodes. As well the responsivity gives a direct indication of the optical absorption coefficient.

5.1.1 Responsivity

As we have discussed previously one of the goals of this work was to demonstrate a detector that had simultaneously high bandwidth and high responsivity. We know from discussions in Chapter 2 that generally speaking there is a trade off between high responsivity and high electrical bandwidth. The design of TWPD presented in Chapter 4 suggests that these detectors should have a high responsivity since most of the optical power is absorbed within 200μm as we have seen in Figure 4.11. Shown below in Figure 5.1 is the setup used to determine the responsivity of the photodiode.

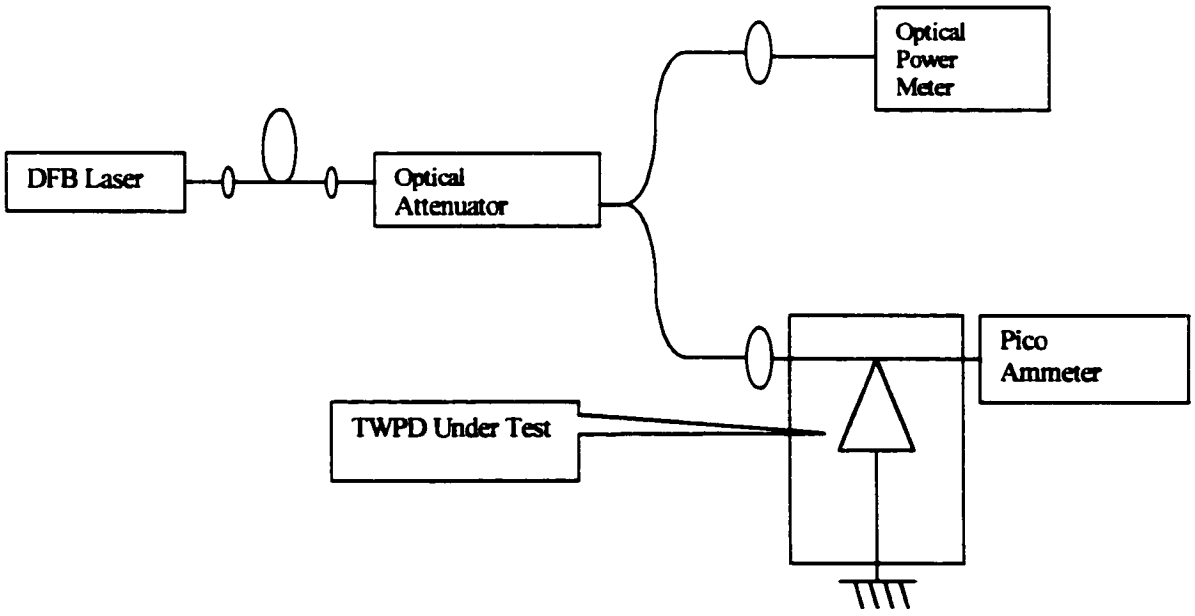

Figure 5.1 Responsivity measurement setup

The DFB laser had a maximum output power of 5 dBm at a fixed wavelength of 1553.3 nm. No intensity modulation was impressed upon the laser. The DC optical signal was then fed directly into an attenuator, which was used to control the optical input power to the TWPD. The signal was then fed into a Y-junction 3 dB splitter with one end feeding an optical power meter and the other side feeding the TWPD. The photocurrent was then fed into a pico-ammeter, which possessed a sensitivity of 1.0 fA. A device with a signal ground spacing of 10μm, width of 8 μm and length of 50 μm was used for both layer designs. The TWPD was reversed biased at −1V while the optical power was swept via the potentiometer. This was done while recording the input power via the optical power meter and the photocurrent generated via the pico-ammeter. The results are shown in Figure 5.2 for structure A and Figure 5.3 for structure B.

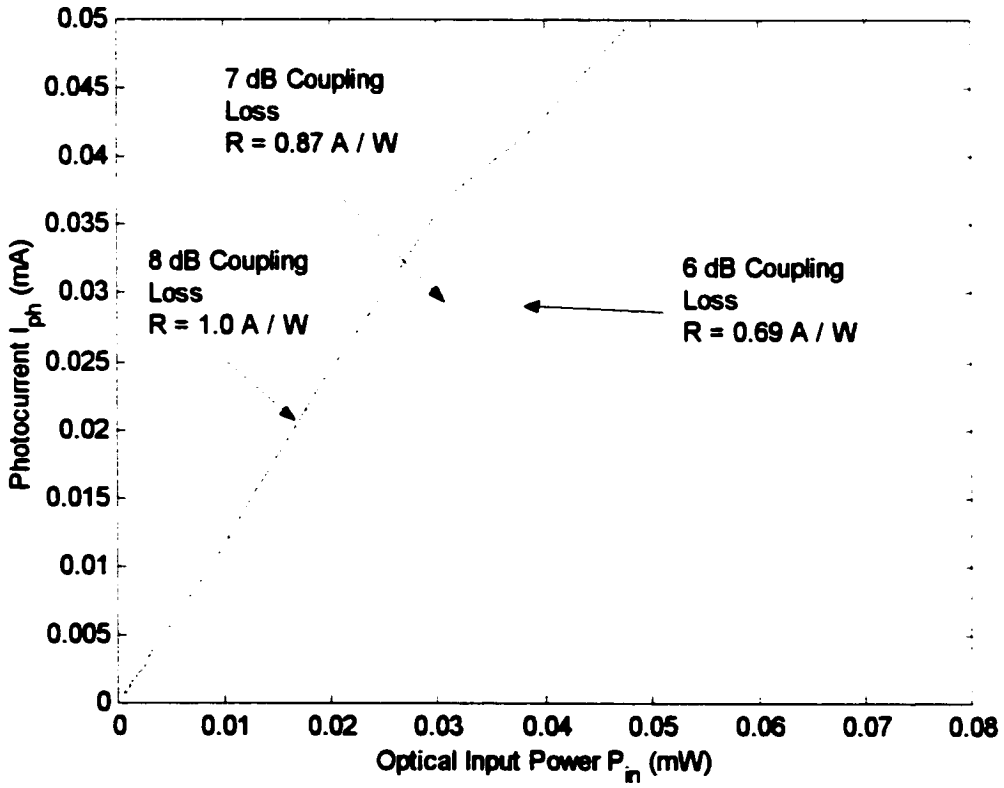

Figure 5.2 Photocurrent vs. optical input power for structure A

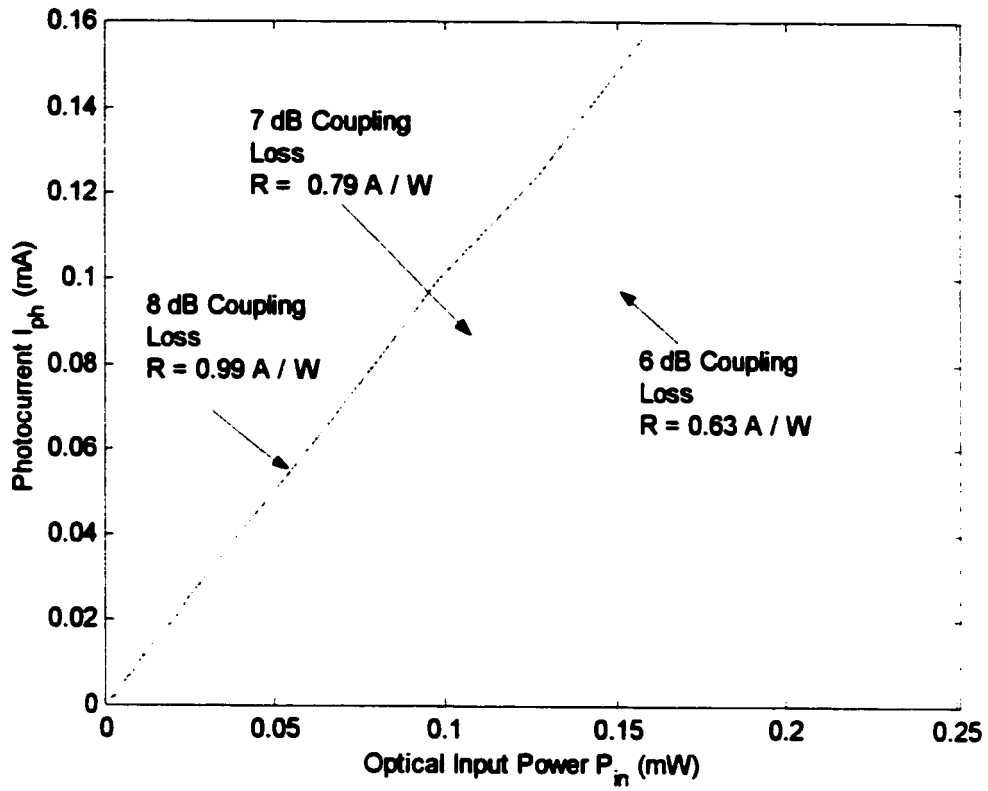

Figure 5.3 Photocurrent vs. optical input power for structure B

These series of graphs were plotted assuming coupling losses of 6, 7 and 8 dB. If one assumes a typical coupling loss of 7 dB, this would result in a responsivity 0.87 A/W for structure A, and a responsivity of 0.79 A/W for structure B. We find that despite the short length of these devices they exhibit an unusually high responsivity. This can be explained by noting that the simulation did not account for multiple passes of the optical signal. That is in the simulation the loss calculations were done based on a single pass of the optical signal through the detector. However, in reality the optical signal will be reflected at the both the input end and the termination end. Any energy that is not absorbed will be reflected back toward the input. The multiple optical reflection would increase the responsivity of the device making the optical absorption coefficient (α) appear larger than those calculated in the simulation.

5.1.2 Linearity and Saturation Current

One measurement that is often quoted in commercial photodiode data sheets is the dynamic range. That is what is the maximum output current that the photodiode can deliver to a load before saturating. This measurement was attempted by placing an EDFA with a gain of 30 dB and a noise figure of 10 dB after the DFB laser shown in Figure 5.1. Unfortunately, the maximum output power of the EDFA is 9 dBm, thus limiting the maximum input power to the detector before coupling of to 6 dBm. Saturation was not observed for either Structure A or Structure B at these power levels, thus concluding that the saturation current is somewhere above -2 dBm assuming a 8 dB coupling loss.

5.1.3 Ideality Factor and Extrapolated Leakage Current

The ideality factor is a measurement of how close to ideal were the conditions under which the physical device was fabricated. The ideality factor can range from 1.0 for an ideal diode to 2.0 where the diode exponential curve is poor. The measurements for the ideality factor were performed using a four probe measurement system to minimize the parasitic capacitance of the measurement. Two probes were placed at the anode while the remaining two probes were placed on the cathode. This is shown below in Figure 5.4.

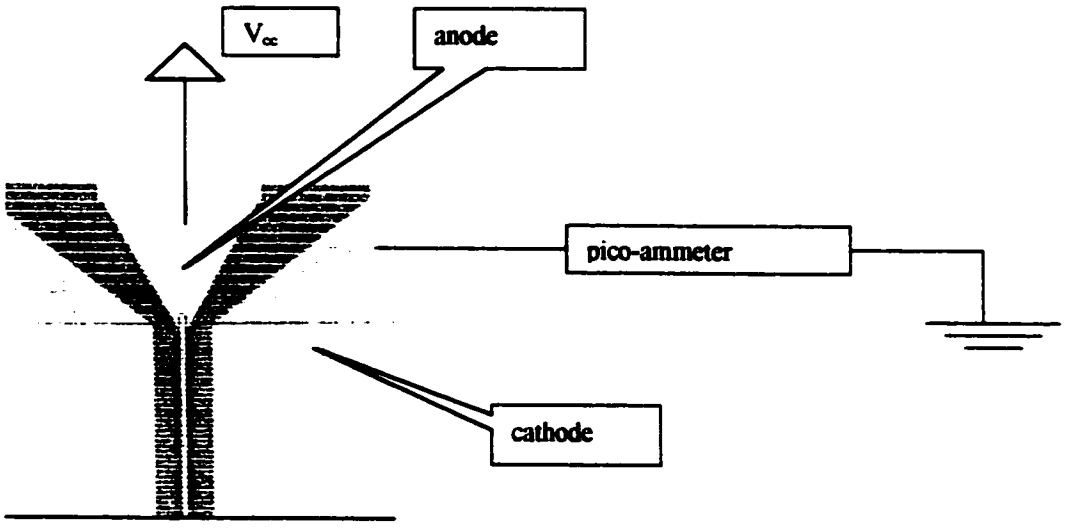

Figure 5.4 Ideality factor measurement setup

The voltage was swept in the forward bias direction and the current was measured. Two exponential curves were generated as illustrated in Figure 5.5 and the ideality factor for both structures is calculated via relationship (5-1) using the most linear section of the graph.

$$\ln I = \ln I_o + \frac{qV_a}{nkT} \tag{5-1}$$

Structure A exhibits an ideality factor of 1.59 while structure B exhibits an ideality factor of 1.93. Structures having the same geometry were measured; the ground electrode spacing is 40 μm, the width of rib is 10 μm and the length is 50 μm. The high ideality factor could be due to surface states or material impurities.

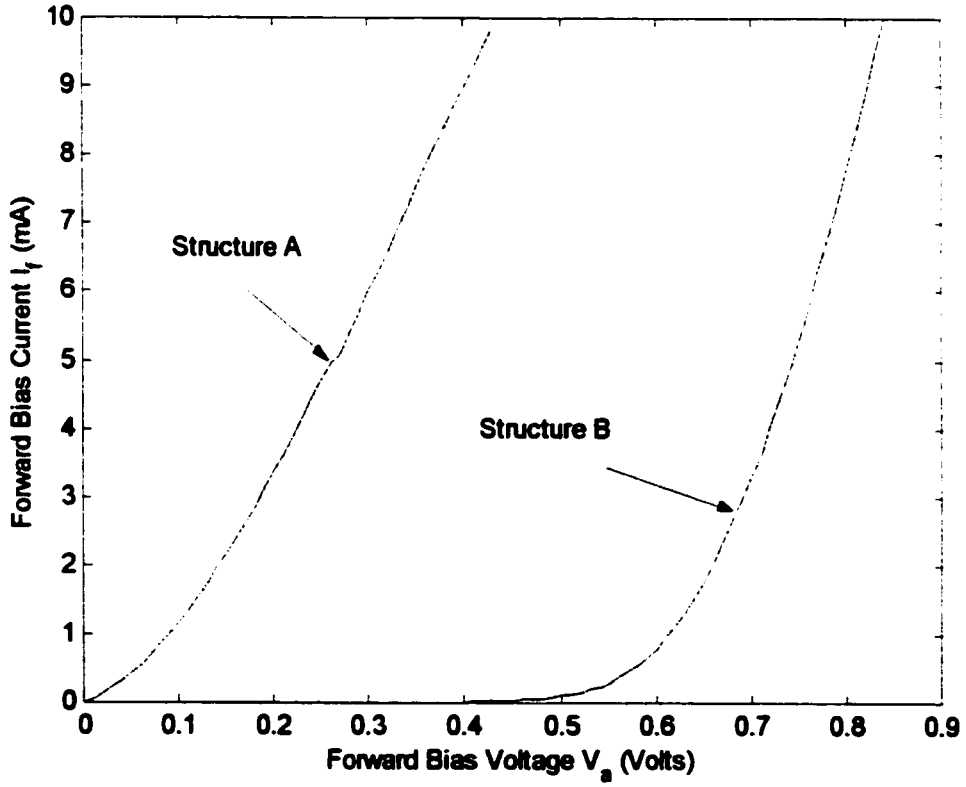

Figure 5.5 I-V curves for structure A and B

Equation (5-1) was also used to extrapolate a leakage current value for both devices. The extrapolated leakage current using equation (5-1) was determined to be 44 fA for structure A and 37 nA for structure B. Although presented here for completeness these extrapolated values generally do not correspond very well to the actual measured values. This is because equation (5-1) neglects the recombination current. That is at low or no bias voltage there is a significant amount of recombination in the intrinsic region, this recombination current contributes to the overall diffusion current thus increasing the measured value of leakage current.

5.1.4 Threshold Voltage and Breakdown Voltage

As observed in Figure 5.5 the built in potential voltage for structure A appears to be approximately 50 mV while the built in potential voltage for structure B is 550 mV. The reverse breakdown voltage for structures A and B were measured using a curve tracer and found to be approximately –5 V and –8 V respectively. Both the threshold voltage and breakdown voltage were observed to be relatively independent of device geometry.

5.1.5 Leakage Current

As stated in Section 5.1.3 the extrapolated leakage current is inaccurate because the recombination current is assumed to be insignificant at low bias voltages but this is generally not the case. For this reason the extrapolated leakage current using equation (5-1) tends to underestimate the true leakage current value. Table 5.1 shows the measured leakage or dark current as a function of length when –0.25 volts reverse bias is applied to structure A and B. The geometry for both structure A and B has a rib width of 10 μm width with a signal ground spacing of 40 μm. We know that the leakage current will be a function of device area, specifically the device length. It will also be a function of the width of the rib, however, this effect should be secondary compared to be the device length.

Length of Device (μm)	Dark Current for Structure A (nA)	Dark Current for Structure B (nA)
50	39	31
100	63	54
200	74	63
300	91	82
400	126	108
500	129	108

Table 5.1 Leakage current vs. device length

As expected the leakage current increases with device length and the value of the leakage current is greater for device A than device B. The larger leakage current in device A can be explained by observing that the thickness of the intrinsic region is greater for device A than device B. From theory we know that the recombination current is directly proportional to the thickness of the intrinsic region, thus the larger the intrinsic region the greater the leakage current, hence we expect structure A to have a higher leakage current value than device B.

Ideally the leakage current should be constant with negative voltages. However, in reality the I-V characteristics of p-i-n diodes usually exhibit a small slope with negative voltage. Table 5.2 shows the leakage current at different bias voltages for structure A and B for a 50 *μm* device with a signal ground spacing of 40 *μm* and a rib width of 10 *μm*.

Bias Voltage	Structure A (μA)	Structure B (μA)
-1	7.424	1.8649
-5 (V_{BR} for Structure A)	44.88	9.669
-8 (V_{BR} for Structure B)	N/A	48.312

Table 5.2 Dark current at different bias voltages for structure A and B

The devices were typically biased at a reverse bias voltage of −1 V. This bias voltage represents a satisfactory compromise between minimizing leakage current, achieving electron saturation velocity and at the same time assuring the device is operating sufficiently far away from the breakdown voltage. That is at this voltage the electrons are at saturation velocity and the leakage current is relatively low as to be able to differentiate the signal from the dark current. In fact it can be seen in Table 5.2 and has been observed through measurements that the leakage current can be large enough such that an optical signal could not be detected. This ultimately has the detrimental effect of reducing the sensitivity of the detector.

5.2 Optical Measurements

From the simulation chapter there are three optical measurements that are important and can be compared against the measurement results. The first is the optical absorption coefficient, which has already been discussed with the responsivity measurement. The other two are polarization dependency and the absorption spectra. We shall begin with the polarization dependency of TWPD.

5.2.1 Polarization Dependency

Ideally the detector should be insensitive to polarization, and generally speaking most commercially available detectors are polarization insensitive. However, the very nature of the optical rib waveguide used

in TWPD implies polarization dependency. Despite this the simulation had predicted that these TWPD should be relatively insensitive to the polarization. The following polarization measurement setup illustrated in Figure 5.6 provides us with the empirical evidence as to whether these devices are polarization dependent.

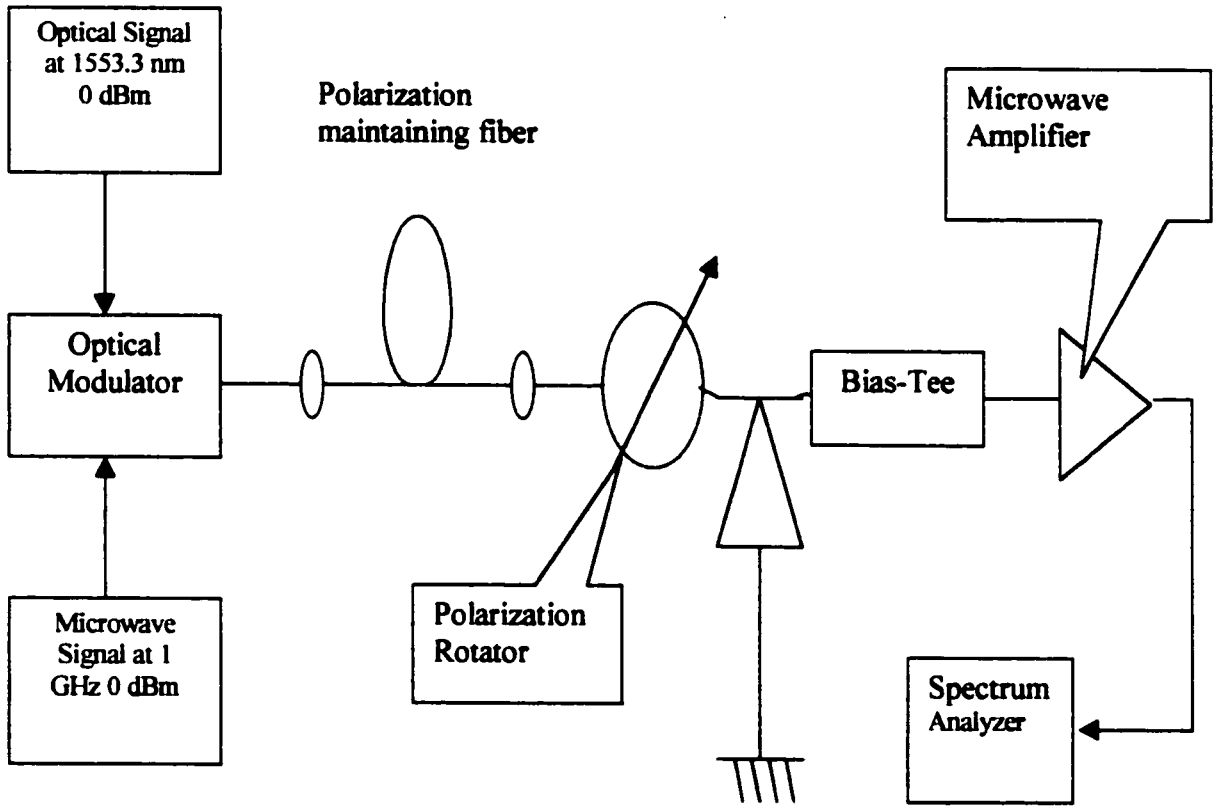

Figure 5.6 Polarization measurement setup

The output of the laser is at 1553.3 nm with a 1 GHz microwave modulation was fed directly into a polarization-maintaining fiber. The optical power and microwave power were both set to 0 dBm. The output of the fiber was then fed into a fiber rotator, which was then butt coupled into the TWPD biased at −1 V. The alignment of the fiber to the TWPD was optimized to obtain maximum output power. A measurement was noted and then using the fiber rotator a 90° rotation was performed. The fiber alignment

was again optimized and a measurement was noted. The results are presented in Table 5.3 for structure A and B.

Structure	Measured Microwave Power at 0° TM (dBm)	Measured Microwave Power at 90° TE (dBm)	Δ (dB)
A	-1.05	-1.70	0.65
B	-1.13	-3.56	2.43

Table 5.3 Polarization measurement results

There is a slight difference between the TE and TM polarization for structure A and a significant difference between the polarizations for structure B. The results are not surprising since device B is has a substantially shorter rib height than structure A, hence will be more susceptible to the differences between TE and TM modes due to coupling to plasmon-polariton modes supported by the metal.

5.2.2 Electroluminescence

Through the responsivity measurement we have determined that optical absorption occurs around 1550 nm. However, as noted in Chapter 4 it is doubtful that the peak of the absorption spectra occurs at the design wavelength of 1550 nm. There are two ways to determine the peak of the absorption spectrum. One way is using a tuneable laser to sweep the wavelength while recording the responsivity. This was done using a tuneable laser with a sweep range from 1500 nm to 1580 nm. However, it was observed that the sweep range was insignificant to observe any measurable changes in the responsivity. Thus an electroluminescence measurement was used to determine the peak absorption wavelength.

Although this structure was design to operate under reverse bias, applying a sufficient forward bias voltage to the p-i-n diode, creates high electron and hole population that recombine in the i region. Thus the TWPD becomes an LED with a peak optical output around the design wavelength of 1550 nm. We can

infer that the peak of the emission spectrum occurs around the same wavelength as the peak of the absorption spectrum. Figure 5.7 shows the measurement setup for the electroluminescence measurement. The TWPD is forward biased at 1 V and a single mode fiber whose alignment to the TWPD has been optimized is used to collect the light. The signal is then observed via an HP70951B optical spectrum analyzer which has a range of 600–1700 nm and a resolution bandwidth of 0.08 nm.

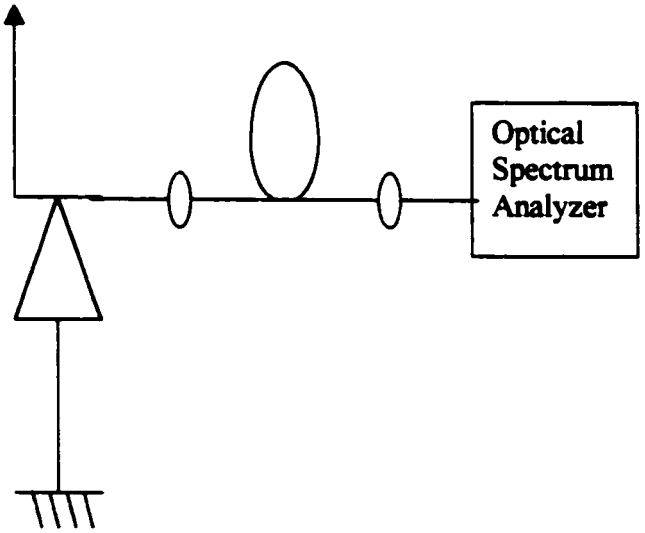

Figure 5.7 Electroluminescence measurement setup

Figure 5.8 show the luminescence curves for structure A and B. We note that the optical spectra are not monochromatic, this is expected since no cavity exists after the diode. We also observe, to no surprise, that the peak occurs at a wavelength other than 1550 nm. In fact the maximum is closer to 1610 nm. The structure used had a signal ground spacing of 40 μm, rib width of 10 μm and length was 50 μm. Several other structures were attempted although it was observed that the optical spectra did not change substantially with device geometry.

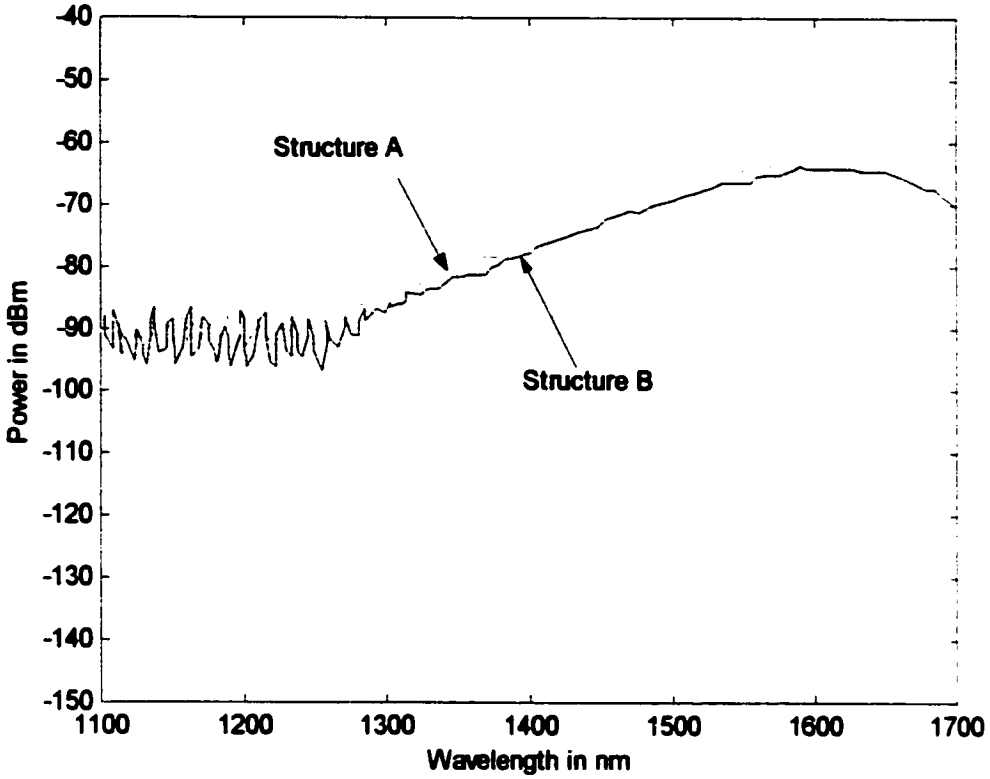

Figure 5.8 Electroluminescence spectra

5.3. Microwave Measurements

Through our discussion of the TWPD we know that two wave guiding structures exist. An optical guide and a microwave guide. Microwave measurements are important in the analysis of the structure because the microwave losses may result in a degradation of bandwidth. We know from Chapter 2 that the microwave bandwidth of TWPD should be nearly independent of device length. However, this is true only where the optical absorption occurs, when the light is completely absorbed and the response is dominated by the microwave propagation characteristics. Thus a very long device may have an inherently smaller bandwidth than a shorter device.

We can characterize the electrical propagation characteristics by using a standard S-parameter measurement setup.

The other important parameter is the electrical or microwave bandwidth. Recalling that the original motivation of this thesis was to demonstrate a TWPD detector that would exhibit both high bandwidth and high efficiency. High responsivity has already been demonstrated, thus an electrical bandwidth measurement would bring this work to a logical conclusion.

6.3.1 S-parameters

S-parameter measurements are a standard and easy way to determine the microwave insertion loss, microwave return loss, characteristic impedance and phase velocity for the electrical waveguide. This measurement was performed using a standard HP8510C vector network analyzer and a cascade probe station. From Figure 4.23 we see that before they have been cleaved the devices are electrically symmetrical, hence only the return loss (S_{11}) and insertion loss (S_{21}) is presented here for a both structures with signal ground spacing of 40 μm, rib width of 8μm and length of 1000μm. Two GGB Industries picoprobes were used which have a passband frequency response up to 40 GHz. The response of the probes, cables and components were properly calibrated out using a standard wafer TRL calibration. A −1V reverse bias was applied to all devices. The results are shown in Figure 5.9 for S_{11} and Figure 5.10 for S_{21}.

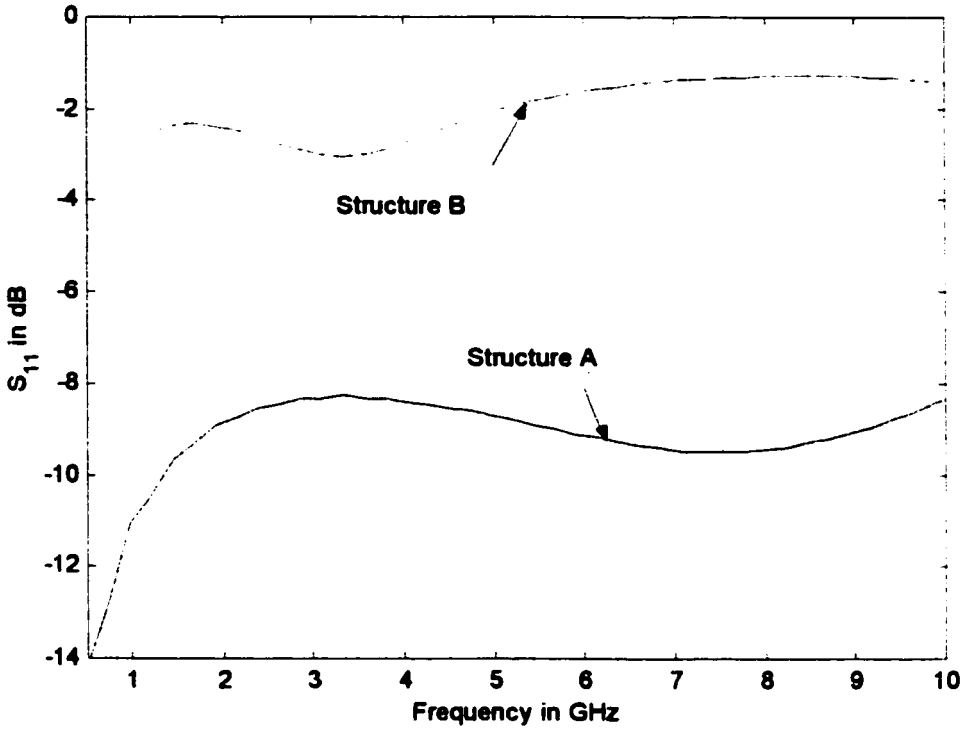

Figure 5.9 Measured S_{11} for structure A and B

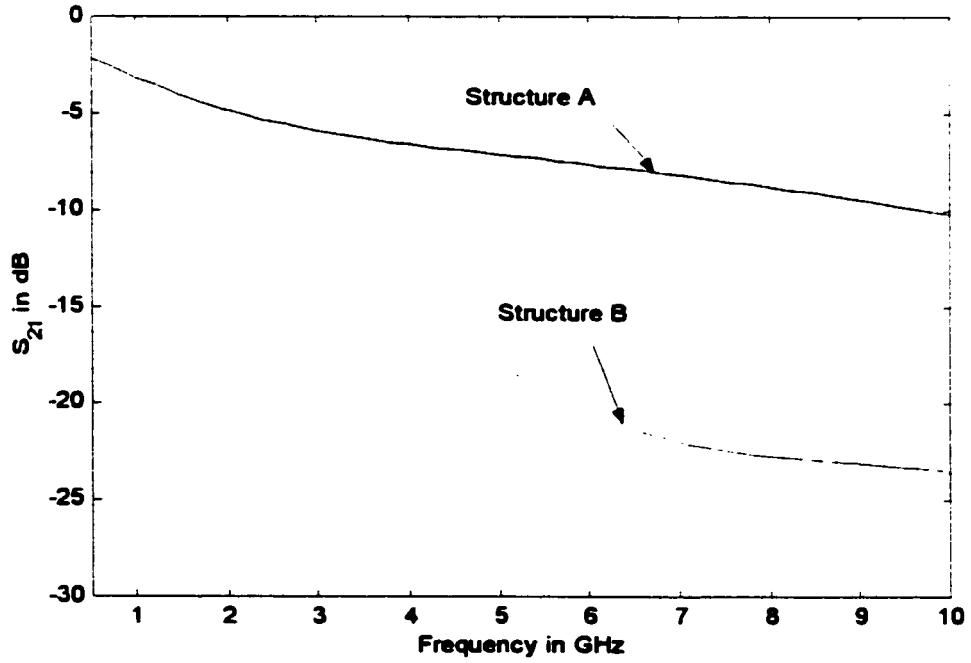

Figure 5.10 Measured S_{21} for structure A and B

Structure A has a better return loss and lower insertion loss than structure B as simulated Chapter 4. Despite this the simulated and measured values are different. The losses are higher than was predicted by the microwave simulations performed in the previous chapter. We shall focus our attention on the simulated results for structure A since a significant amount of time was spent optimizing the microwave guide. As mentioned earlier such attention was not paid to device B. Referring to the simulated results for structure A, shown in Figure 4.16 to 4.18 the simulated return loss at 10 GHz is expected to be 20 dB, the measured results in Figure 5.9 indicate a return loss of 8 dB. We also expect the insertion loss for structure A to be approximately 1 dB/mm at 10 GHz, however the measurement in Figure 5.10 shows an insertion loss 10 times this, resting at a value of 10 dB/mm. The return loss and insertion loss for both structures was observed to be almost independent of signal ground spacing and rib width.

Two possibilities exist that could explain the discrepancies between the simulated and measured results. The first is that during the microwave simulation the assumption was made that under strong reverse bias conditions the intrinsic region is completely depleted of charged carriers. In reality this may not be the case, if the i region is not completely depleted of charge carriers this would have the negative impact of increasing the microwave loss. The second possibility is the probe footprint, which shall be discussed in the next section.

5.3.2 Microwave Bandwidth

We have already demonstrated high responsivity, which was one half the original criteria for designing TWPD detectors, the other half rests with the microwave bandwidth. The measurements were done using an OC-192 modulator having an electrical bandwidth of 10 GHz. The measurement setup is shown in Figure 5.11.

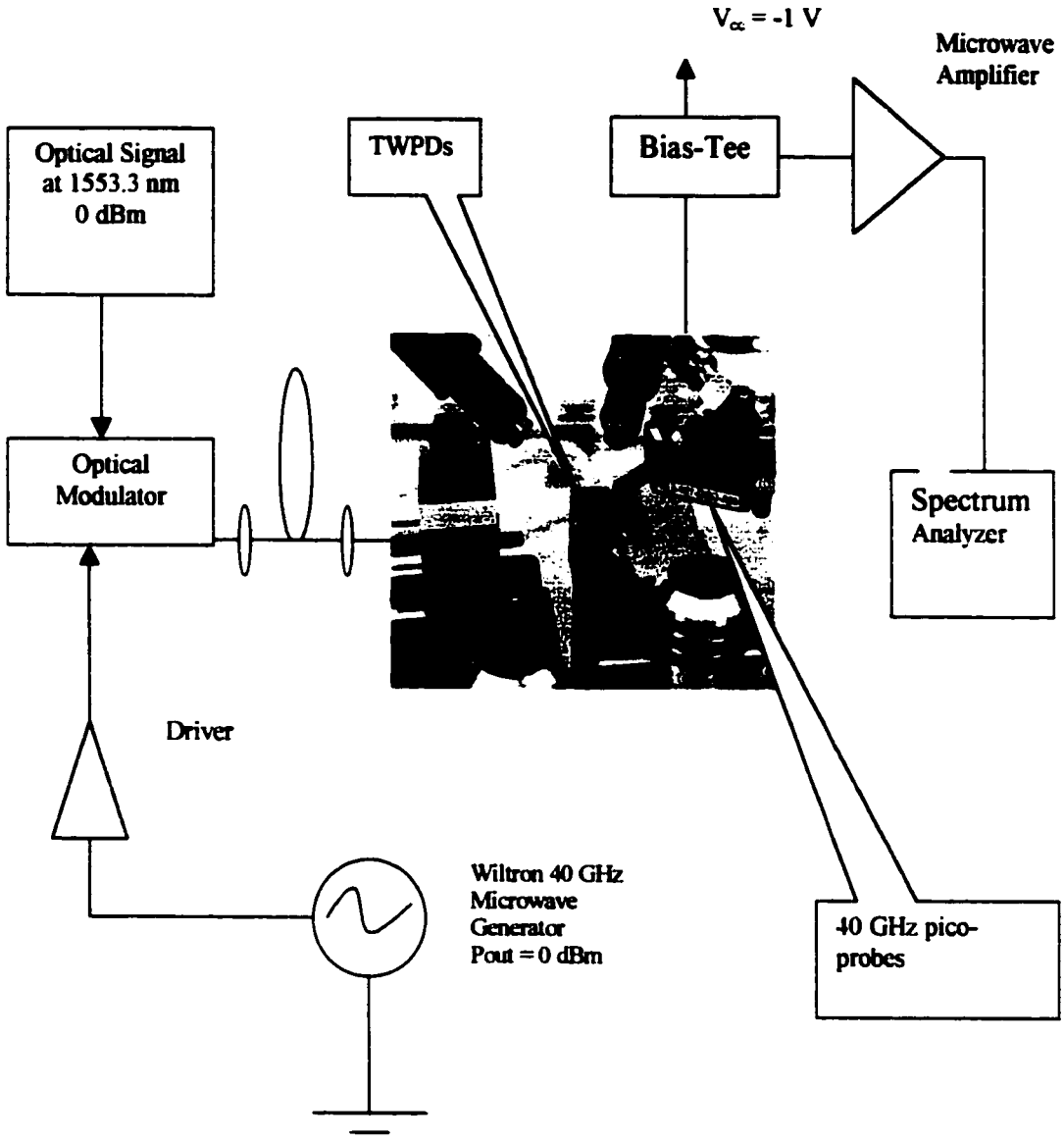

Figure 5.11 Microwave bandwidth measurement setup

An optical signal was generated at 1553.3 nm with an output power of 0 dBm. A microwave signal was generated via a Wiltron microwave generator with an operational range of 10 MHz to 40 GHz. The microwave signal power is set to 0dBm, which was fed into a driver amplifier and then modulated onto the optical carrier. From here the modulated output goes directly into a single mode fiber, which was butt coupled into the detector under test. One GGB Industries picoprobe was used to collect the AC photocurrent. The probe has a pass band response up to 40 GHz. The electrical signal was then fed into a

bias tee where the DC component was blocked passing only the AC signal to the microwave pre-amplifier. The pre-amplifier has a mean gain of 40 dB over a bandwidth of 22 GHz. The demodulated microwave signal is monitored via a HP8565E microwave spectrum analyzer whose operational range extends to 55 GHz.

The TWPD was biased at –1 volts with the DC signal being applied to the bias-tee whose frequency response extends to 22 GHz. The microwave frequency was swept from 1 GHz to 10 GHz by increments of 500 MHz while the microwave power is recorded. The response is shown below in Figure 5.12 and 5.13 for structure A and B respectively. The data were gathered for devices having a signal ground spacing of 40 μm a rib width of 10 μm and length of 50, 100 and 500 μm.

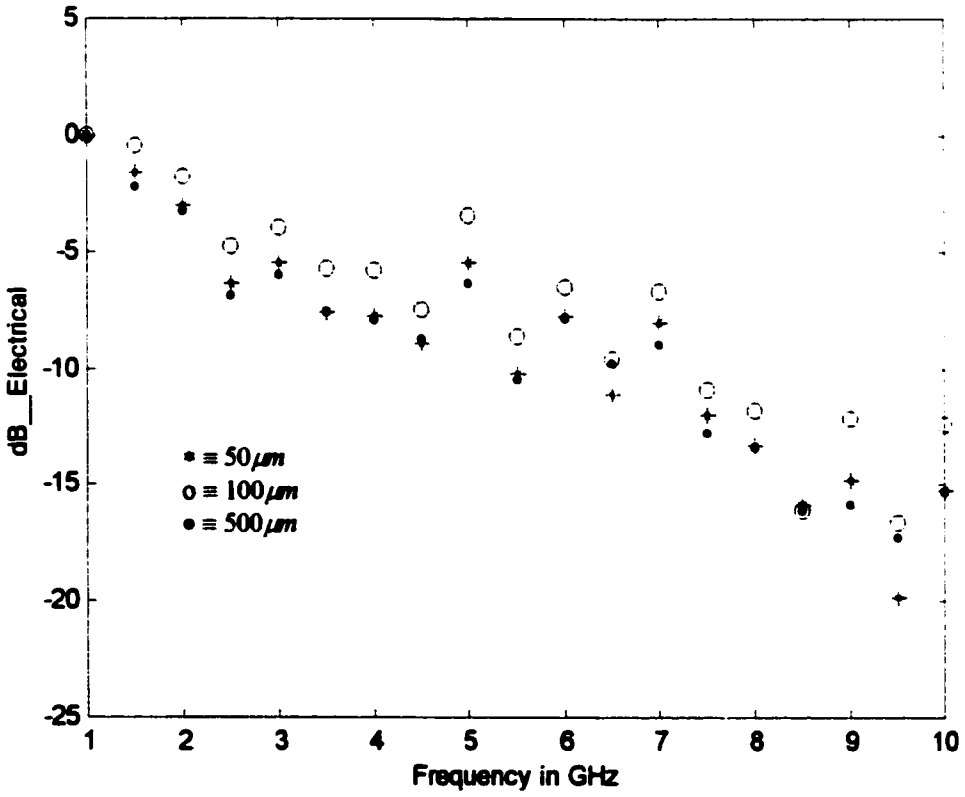

Figure 5.12 Frequency response of structure A

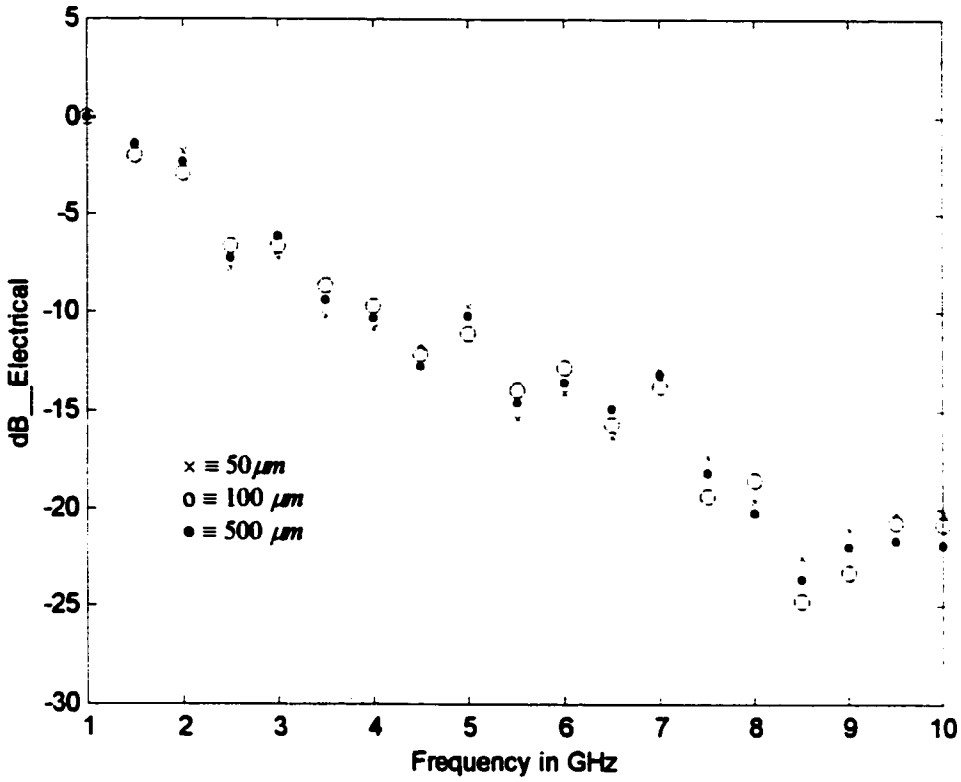

Figure 5.13 Frequency response for structure B

It is evident from Figure 5.12 and Figure 5.13 that the frequency response appears to be relatively independent of device length. It is also evident that the 3 dB that the response appears to be quite similar for both devices resting around 1.2 or 1.3 GHz. The 3 dB frequency response is much lower than what is expected and also what has been reported in the literature.

As noted in Chapter 4 no equation or model has been presented here, or in the scientific literature that can accurately predict the microwave bandwidth of a TWPD, thus one can imply that no direct comparison with theory could be made. In fact this was one of the reason why two designs were implemented. Hence, it would be very easy to state that the bandwidth was observed to be independent of device length thus confirming the theory. However, this would be an incorrect statement because it does not account for why the microwave bandwidths are also very similar for both devices A and B. This similarity in bandwidth

between the two designs suggests a commonality between both structures that is affecting the bandwidth of both designs equally. Recalling that design philosophy was to optimize one structure while trying to reproduce results presented in the literature for another structure. Hence the common thread cannot reside in the semiconductor, microwave and optical design since the two structures are significantly different. Thus the commonality must be in the layout. That is the same mask design was used for both structures A and B hence, any design flaw must reside there. Looking at the mask design we note one key parameter that was not initially considered in the layout: the probe footprint. This footprint is used to make electrical contact with the device so that the photocurrent could be collected. This is shown in Figure 5.14.

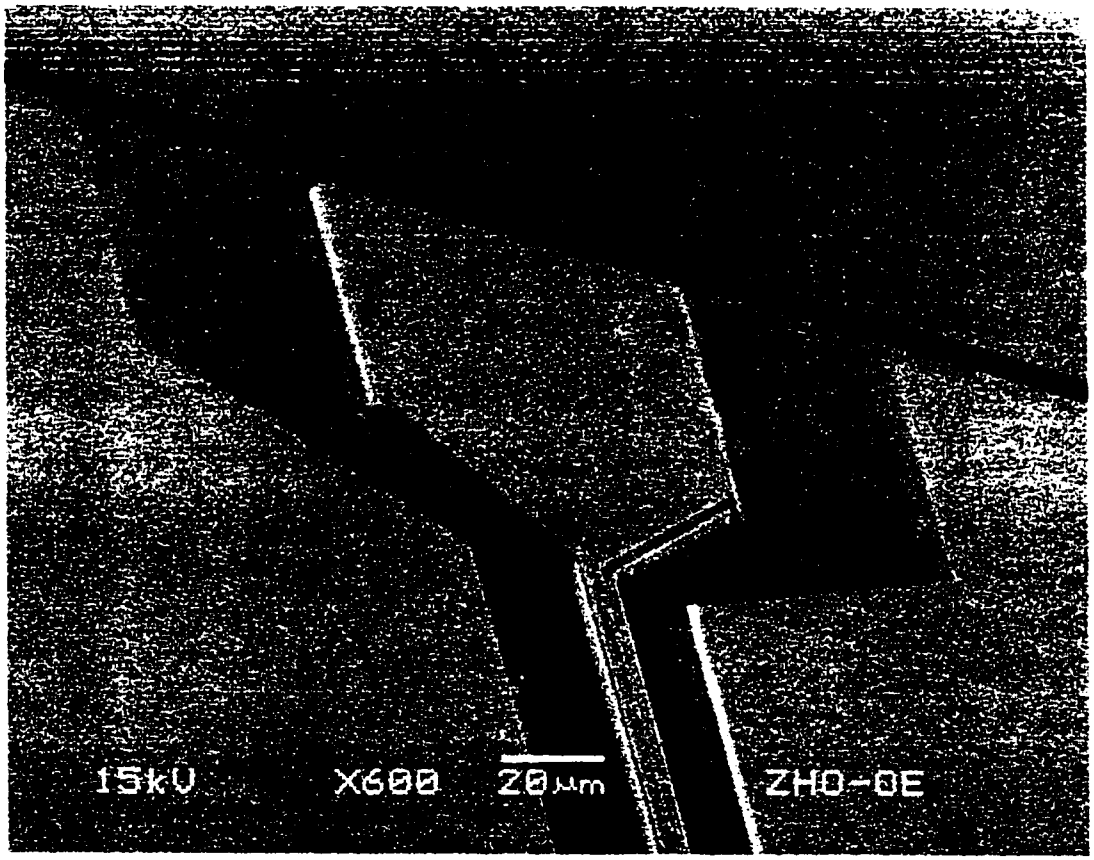

Figure 5.14 Probe footprint

This probe footprint behaves electrically like a large capacitor at the load. Hence the equivalent circuit for the TWPD is shown in Figure 5.15:

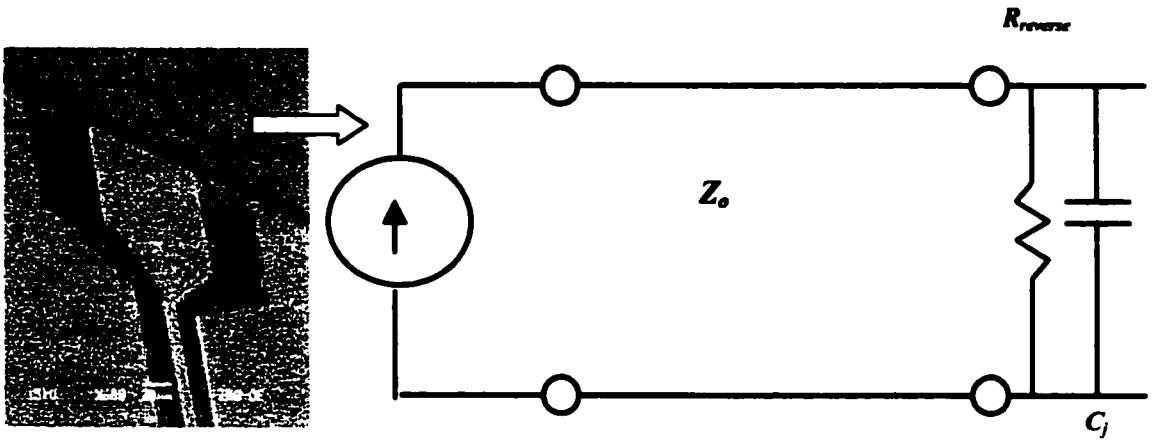

Figure 5.15 Equivalent circuit for TWPD including probe footprint

Z_o, $R_{reverse}$, C_j are the characteristic impedance, reverse bias resistance and junction capacitance respectively. It is suspected that the reverse bias resistance and junction capacitance is limiting the high frequency performance of the device. Thus what we are observing through the measurements is not the TWPD bandwidth, but the RC bandwidth of the probe footprint. To confirm this hypothesis a simple calculation is performed for the capacitance and reverse bias resistance. The calculation uses $50\mu m \times 75$ μm as the approximate area of the probe footprint. With a –1 V reverse bias and –5 dBm optical input power before coupling this generates a 75 μA photocurrent for structure A and a 54 μA photocurrent for structure B. Using these values the corresponding reverse bias resistance, junction capacitance and bandwidth is calculated and shown in Table 5.4.

Structure	R (kΩ)	C (pF)	BW (MHz)
A	13	0.132	≈ 92.7
B	18.5	1.34	≈ 6.43

Table 5.4 Calculation of RC bandwidth for probe footprint

Since measurement were started at 1 GHz with these devices it can be argued that the roll off frequency may be in fact lower than 1.2-1.3 GHz. That is the similarity in measured bandwidth for both designs coupled with the bandwidth calculation done for the probe footprint indicates that this footprint may be affecting the response of both designs. This low frequency response would mask the true performance of the TWPD detector, thus making the true result indeterminate.

This same argument represents the second possibility for explaining why the microwave return and insertion loss measurements presented in the last section differ from those simulated. That is the true response of the device could be masked by a large capacitance and thus one can not definitely determine the microwave loss in this device.

Chapter 6 Conclusion

The original motivation for this work was the design of a high-speed photodetector around 1550 nm that would exhibit both high responsivity and high bandwidth. One half of this original goal has been successfully satisfied and demonstrated via the measurements. The other half of the criteria, high bandwidth, has been shown to be around 1.2 GHz for structure A and 1.3 GHz for structure B. The lack of a sufficiently adequate microwave bandwidth has been attributed to the probe footprint in the mask design. This footprint may be masking the true microwave response of the detector.

The work to date has encompassed the modeling, design, simulation, fabrication and measurements of a detector. Despite this a significant amount of unknown parameters still need to be investigated further both from an empirical and modeling perspective.

6.1 Summary

Chapter 2 discussed the physical phenomena behind optical detection and their relationship to the material parameters. Different photodiode architectures were presented and the advantages and disadvantages of each structure discussed. A derivation was formulated demonstrating the inherent trade off between bandwidth and efficiency present in all vertically illuminated detectors. This was followed by a list of design points illustrating how to increase the frequency response of p-i-n detectors.

The WGPD detector was presented noting its similarities to the TWPDs, and pointing out both its advantages and shortcomings over vertically illuminated detectors. The shortcomings of the WGPD can be overcome by the use of a TWPD. This type of architecture has the potential of providing simultaneously a large microwave bandwidth and high responsivity, something that has been traditionally been traded off in VPDs and WGPDs because of their inherent RC limitations.

Three models were presented that described the electrical behavior of TWPDs. The first is the waveguide

model, which uses a transverse resonance method to solve the propagation constant thereby yielding the characteristic impedance, microwave loss and other microwave parameters. The equivalent circuit model is essentially a transmission line model, which allows the microwave characterization of the structure via inductance (L), capacitance (C), conductance (G) and resistance (R) terms.

Using the velocity mismatch bandwidth model a theoretical bandwidth formula was derived. This bandwidth calculation not only demonstrates that a TWPD can be made optically long and electrically short, but also demonstrated that under the open circuit input condition, which is the condition present in the laboratory, the microwave bandwidth is independent of velocity matching. This raises an intriguing question. Are these devices truly traveling wave in nature?

Traditionally a traveling wave device involves the copropagation of two waves propagated down their respective guides, interacting with each other over several wavelengths. In this case the two waves are microwave and optical in nature and if these two waves co-propagate in a coherent fashion, the waves are said to be velocity matched, otherwise they're velocity mismatched. However, in this case the structure is electrically very short and optically very long hence very little traveling wave effects actually occur. Thus can one justify describing these devices as a traveling wave devices? This same effect is observed in the prediction of microwave bandwidth. The bandwidth prediction is independent of velocity mismatch, which is indicative of a device that does exhibit no traveling wave effects. This lack of comprehension along with the inadequacy of the models leads to the conclusion that a full wave analysis is required to understand the waveguiding behavior of these devices.

Chapter 3 was solely devoted to the formulation and validation of the Method of Lines. The chapter began with a heuristic description of the method. Proceeding with a list of the advantages and disadvantages inherent to this numerical algorithm. A formulation was derived and presented for a lossy inhomogeneous structure and the results compared against those found in the scientific literature.

The validation section of Chapter 3 involved the use of three structures presented in the literature to

adequately confirm the formulation and the program. The first two are lossless rib structures where the effective index is calculated for one rib and the dispersion curve generated for the other. The monotonic behavior of the MoL was demonstrated and Richardson's extrapolation was performed. The field distributions are presented to confirm that the correct propagation constants have been found as well as to point out the optical similarities between the rib waveguide and the TWPD. To ensure that a lossy structure can be handled a Schottky contact TWPD was analyzed. All results indicate that the formulation is correct and the program has been coded properly.

The simulation and design of the TWPD devices is presented in Chapter 4. It is recognized that the design of a TWPD must be broken down into three sub-designs, the semiconductor design, the optical design and finally the microwave design. Each of these sub-designs will have their own individual design requirements, which may conflict with the requirements of the other sub-designs. The chapter begins with the choice of photodiode architecture, followed by the semiconductor layer design. A discussion of the material choice was presented in the semiconductor design along with the reason for the use of quantum wells and the importance of lattice matching.

Chapter 2 demonstrated the limitations of the current theoretical models. To help address modeling issues, a design philosophy was taken involving two designs. One design would be optimized for phase velocity matching, characteristic impedance and minimization of microwave loss, while the other design would be unoptimized. The idea behind this design philosophy was to allow a direct comparison regarding velocity matching, microwave loss and characteristic impedance between the two structures. If these devices are truly traveling wave structures than coherent propagation between the microwave and optical signal will be important, that is velocity matching will be critical. If these structures exhibit no traveling wave effects, as the theory suggests, then the velocity matching will be irrelevant. Either way, two designs are necessary to do such a comparison. With this said, two TWPD designs were presented each having their own semiconductor structure, optical and microwave behavior. In the semiconductor design section of Chapter 4 the layer designs were presented and the tradeoffs are discussed along with any design assumptions and limitations.

The optical design began with a discussion on how to model the semiconductor losses and the top ohmic contact. Confinement factor and the Poynting vector are two important parameters involved in the optical design they were discussed in detail. An observation was made regarding these parameters and a possible simplification inherent to rib waveguides. The use of the equivalent slab waveguide was presented for structures A and B to provide a good initial guess for the MoL. Using the initial guess provided by the slab waveguide the propagation constants for the rib waveguides for structure A and B were generated. The results suggested that the optical guide present in TWPD is polarization insensitive. The effective absorption coefficient calculated via the MoL for each individual structure also suggests that the devices can be made electrically very short. This not only confirms the analytical models presented in Chapter 2, but it also reinforces the question regarding any traveling wave effects presented in these detectors. The multi-mode nature of the guide was discussed and the fields for both single mode as well as higher order modes were generated.

The microwave waveguide design was presented for both devices. In order to analyze this structure from a microwave perspective a series of assumptions and simplifications were made regarding specific semiconductor parameters. These simplifications and assumptions involved molar fractions, breakdown voltage, leakage current, contact resistance, mobility, and their relationship to doping and biasing. With these simplifications it was acknowledged that the microwave design could proceed.

In keeping with our design philosophy one design was optimized assuming the traveling wave effect would be critical while the other considered this criterion irrelevant. While designing the microwave waveguide the slow wave effect was observed, but more importantly a realization was made that the fields in these structures are very similar to those present in the microstrip line. Thus the critical parameters that affect the characteristics impedance of a TWPD are essentially the same as a microstrip line, that is the thickness between the top electrode and the ground plane.

The simulated microwave results were presented for both structures and a bandwidth calculation was performed using the velocity mismatch bandwidth model derived in Chapter 2.

Chapter 4 concluded with a presentation of the mask design. A discussion involving the limitations of device fabrication, alignment tolerance and contamination is presented. These assumptions had an impact on all three designs, semiconductor, optical and microwave. The mask was designed to reflect the amount of unknown variables.

The theory, design, simulation and fabrication culminate with the measurements presented in Chapter 5. The measurements are broken down into three aspects, the DC measurements, the optical measurements and the microwave measurements. Although other measurements such as breakdown voltage, leakage current, electroluminescence, ideality factor etc. were included for completeness, the emphasis was placed on the microwave bandwidth and responsivity.

The chapter began with DC measurements starting with the most critical of all the DC measurements, the responsivity. The responsivity measurements indicate that even with the shortest device the responsivity is exceptionally high. In fact such a high responsivity suggests that the optical absorption coefficient is significantly higher than the results simulated. Alternatively, it is hypothesized that the cause for this high responsivity, given such a short structure, is a result of optical reflections. That is, multiple passes of the optical signal through the rib waveguide would increase the effective absorption coefficient α, thus increasing the responsivity of the device.

Linearity and saturation current were measured and the results suggest that the saturation current is somewhere above an input optical power of -2 dBm assuming a coupling loss of 8 dB. The ideality factor for both devices was measured and calculated by generating I-V curves. The results indicate that the ideality factor for structure A is 1.59 while the ideality factor for structure B is 1.93. The breakdown voltage was measured using a curve tracer. The results indicate a –5 V breakdown for structure A and a –8 V breakdown for structure B. Leakage current was measured with a pico-ammeter and as expected it is a function of both bias and device length.

The simulations predicted that both devices should be fairly insensitive to polarization. The measurements

indicate otherwise by demonstrating that these devices fundamentally support TM modes and lose some power when the polarization is changed. As expected though the short device, structure B, is definitely more susceptible to the effects of optical polarization. The electroluminescence measurements gave an indication of the spectral location of maximum absorption. By applying a forward bias to the diode and butt coupling the light into a fiber, we observed that the peak occurs somewhere around 1600 nm for both devices. Again as stated in Chapter 4 the predicted shift maybe a result of bias, Stark effect or any other quantum phenomena not taken into account during the simulation.

The two microwave measurements for the devices are S-parameter measurements and bandwidth measurements. The return loss and insertion loss are generally higher than the values simulated. This may either be an indication of potential contamination in the intrinsic region or a result of the probe footprint masking the true response of the device. The first hypothesis rests on the fact that during the simulation the intrinsic region was modeled as being completely depleted of charge carriers. If carriers still exist in the intrinsic region, even under strong reverse bias conditions, this may have a detrimental impact by increasing the microwave losses. The second possibility is the probe footprint, which is discussed in detail in the next paragraph.

The bandwidth for both structures is quite low around 1.2 or 1.3 GHz. The independence of bandwidth on device length and device structure indicates a common problem in the two structures that is affecting the response of both devices equally. A simple capacitance calculation was performed and results seem to indicate that the probe footprint is behaving like a large capacitor, thus causing both devices to exhibit a RC roll off. It is suspected that this RC roll off is masking the true response of the device.

Despite the fact that one half of the original motivation of this work has been met, there still remains a considerable amount of work outstanding. The following suggestions are made for furthering the work initiated by this thesis.

6.2 Future Work and Improvements

A significant amount of work has been done in the areas of numerical modeling, simulation and empirical measurements. It is for this reason that the discussion involving possible future work has been divided in two different areas, improvements to the MoL and improvements to the TWPDs. We shall begin with possible improvements to the Method of Lines.

6.2.1 Future Work and Improvements Involving the MoL

As stated in Chapter 3, one of the difficulties in working with the MoL is the solution to the indirect eigenvalue problem. In order to solve this problem an initial guess has to be given to the eigenfunction $det[G_{e,h}(\gamma)] = 0$. If this guess is poor the propagation constant may converge to an undesirable solution. There has been some suggestion in recent papers in this area by Chen et al[99], that the roots can be found via the Cauchy Integral theorem. Instead of solving the indirect eigenvalue problem by searching for the roots one would use Cauchy Integral theorem to generate an approximate polynomial that would provide a mapping to the propagation constants. If such a mapping does exist it would not only represent a tremendous contribution for the MoL, but a tremendous contribution to the field of numerical modeling in general.

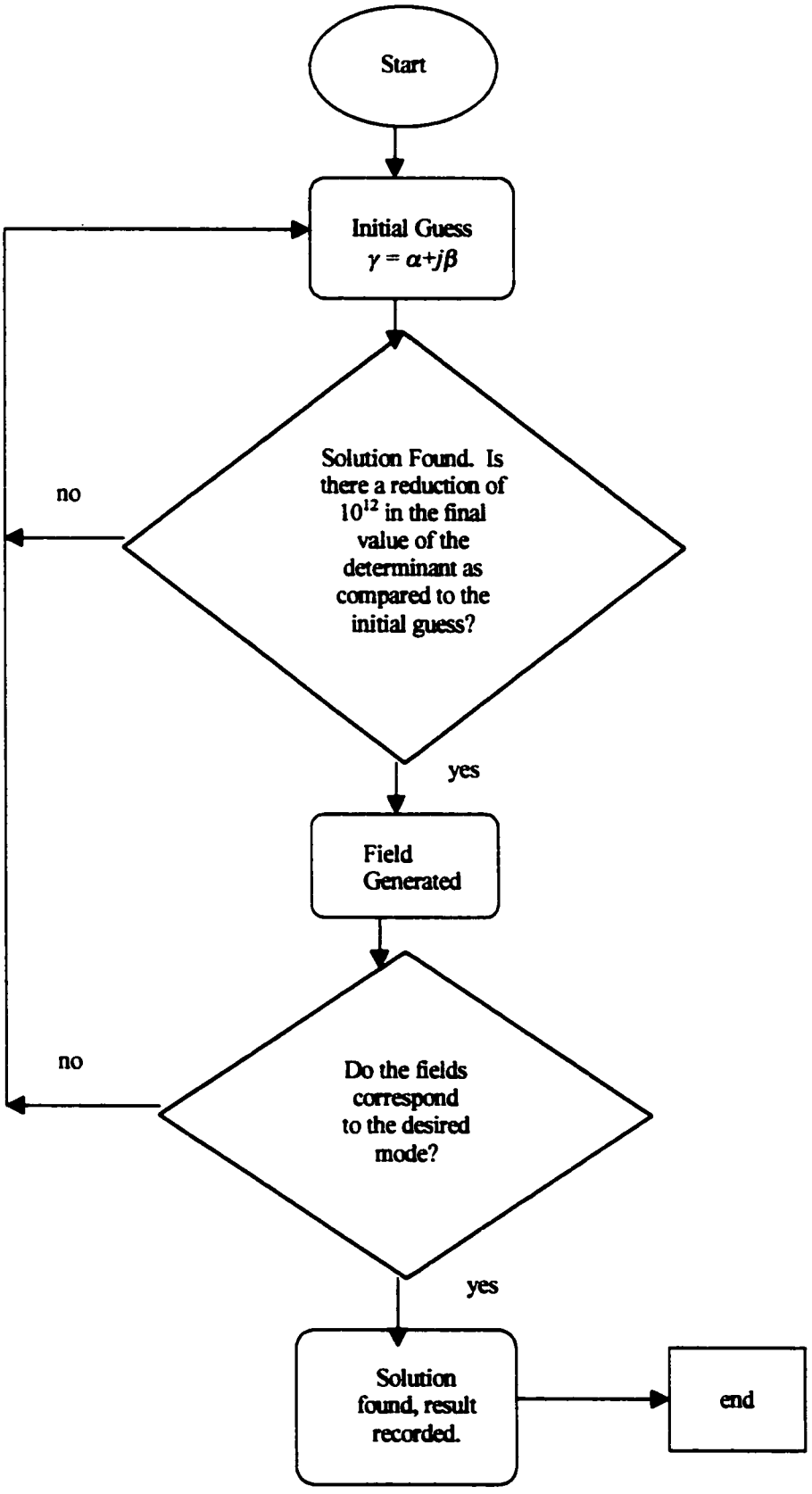

Figure 6.1 Procedure for determining root

Under the current MoL algorithm the roots of the determinant equation have to be determined individually using the procedure described in Figure 6.1. A user must provide an initial guess for the propagation constant, observe if there is a reduction of 10^{12} in the final value of the determinant compared to the original value. If this criterion is observed then a root has been found and the fields are generated, otherwise the another initial guess is given. Once a root has been found the user then proceeds to generate the field distributions to determine if the propagation constant found agrees with the desired mode. If the fields agree with the desired mode the result is recorded, otherwise another initial guess is implemented and the process is repeated. At the end of the entire process one solution has been obtained pertaining to one mode. To obtain curves such as the one shown in Figure 3.9 the process is repeated several times. Generating such curves requires a significant amount of user attention and interaction. Thus making the process tedious and time consuming.

If such a mapping exist it would not only generate individual modes, but all modes, including higher order and hybrid ones simultaneously. This would automated the root finding process and hence significantly reduce the amount of time a designer would spend providing accurate initial guesses to the MoL program.

Another drawback stated in Chapter 3 was the formulation often becomes tailored to specific device geometries which need to be reformulated when the device changes. That is the code often becomes too specific and when there is a slight change in the structure a new program needs to be coded.

All of the MoL coding was done in Matlab. Matlab is an excellent tool for designing and developing programs quickly because it has an enormous number of mathematically efficient functions that have been preprogrammed. With that said, Matlab has one key drawback, it lacks any object oriented abilities. It is a procedural based programming language. Thus true code reuse cannot be implemented and all the benefits provided by object oriented programming such as inheritance, polymorphism and overloading cannot be used. One can envision using a object oriented language and creating a MoL class, where the end user need not worry about whether the structure is inhomogeneous or homogeneous, magnetic or non-magnetic, lossy or lossless. In a well designed MoL class all these parameters associated with the Method of Lines would

be oblivious to the end user. Thus, making the program truly general, hence any structure could be handled without having to re-code entire sections of the program.

6.2.2 Future Work and Improvements Involving the TWPD

As stated in Chapter 5, it is suspected that the true microwave bandwidth of the device may be masked by the RC roll off of the probe footprint. In order to confirm or deny this hypothesis a new mask needs to be implemented and the designs presented in this thesis repeated. This is the logical next step.

Recall from Chapter 2 equation (2-37) which predicts the electrical bandwidth for a TWPD given the phase velocity, confinement factor and optical absorption coefficient. Though this equation was derived in this thesis and has been presented in the scientific literature by Giboney et al[28]. It is unrealistic and inaccurate because it doesn't consider the effects of carrier transit times. Recently there have been two papers that have contributed significantly to the study of TWPDs. The first by Kato et al.[100] presents a formulation for the microwave bandwidth of TWPDs using equation (2-37) but he considers the effects of transit time. The bandwidth equation is shown below with no derivation provided.

$$f_{3dB} = \frac{f_t}{1+\left(\frac{f_t}{B_{VM1}}\right)^2} \tag{6-1}$$

In the above, B_{vm1} is given in equation (2-37) and f_t is the transit time given by

$$f_t \approx \frac{3.5 v_{mean}}{2\pi W} \tag{6-2}$$

where W represents the width of the intrinsic region and v_{mean} is the average carrier velocities of the electrons and holes computed via:

$$\frac{1}{v^4_{mean}} = \frac{1}{2}\left(\frac{1}{v^4_e} + \frac{1}{v^4_h}\right) \tag{6-3}$$

v_e represent the velocity of the electrons, while v_h represent the velocity of the holes. Equation (6-2) provided by Kato et al is essentially the same equation derived in this thesis presented in (2-1). Using (6-2) we re-calculate the predicted bandwidth for structures A and B. We use an electron saturation velocity of $v_e = 2.6 \times 10^7$ cm/s and a hole saturation velocity of $v_h = 8.0 \times 10^6$ cm/s for InP. The results are plotted in Figure 6.2 for device A.

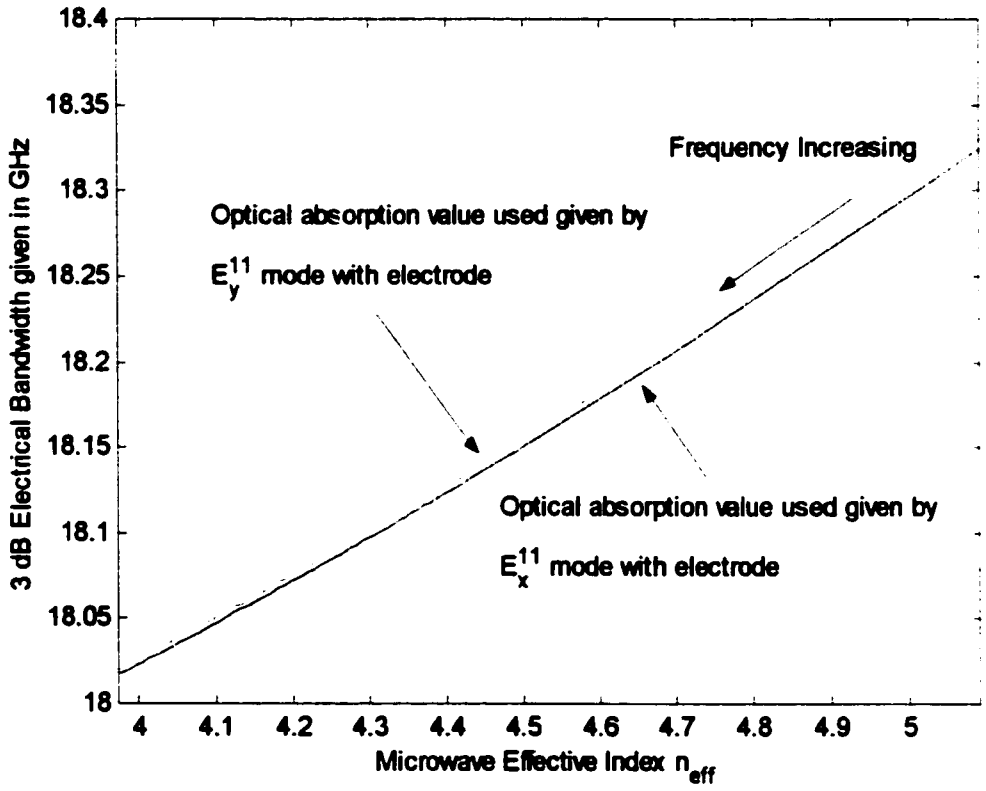

Figure 6.2 Microwave bandwidth vs. effective index using transit time limitation

The microwave bandwidth for device B is not presented since it is identical to Figure 4.20. This is to be expected since $f_t >> B_{VMI}$ in device B hence equation (6-2) simplifies to (2-37). Figure 6.2 not only shows that structure A is limited by transit time, but it also demonstrated as stated in Chapter 4 that device A should be slower than device B. The basis for this statement presented in Chapter 4 was a qualitative one

and was based on the fact that the intrinsic region is significantly larger in structure A than B, hence structure A should be limited by transit time. This is confirmed in Figure 6.2. Despite this confirmation none of these bandwidth calculations have been tested via measurements.

This lack of an accurate bandwidth calculation helps to illustrate an important point. To the author's knowledge no accurate predication of electrical bandwidth has been formulated or simulated and compared against measured results for a TWPD. This point further reinforces the recommendation that the mask needs to be redesigned and the TWPDs structures presented in this thesis repeated.

The second paper comes from Huynen[101] et al. The paper represents the first known attempt at trying to model a p-i-n traveling wave structure as a four port network. By using a 4 port scattering matrix to describe a p-i-n traveling wave device one can describe both the behavior of a traveling wave modulator as well as the behavior of a traveling wave photodiode. Hence this paper may be beneficial to future work involving modulators as well as detectors. If it can be shown rigorously via measurements that a four port scattering matrix can be used to accurately describe the behavior of TWPDs, then an optimized design can be obtained via this method. One can envision re-measuring the devices presented in this thesis with the new mask design and then using those measurements along with the four port scattering matrix formulation presented by Huynen et al to verify if an accurate modeling effort has been obtained. If this can be demonstrated, then an optimized detector can proceed from this point on via simulations alone.

This leads to the last point regarding possible future work in TWPDs. Despite that two structures were designed and measured only one structures was truly optimized: structure A. Regardless of this fact a significant amount of time was spent optimizing structure A to achieve a characteristic impedance of 50 Ω, minimal microwave loss and phase velocity matching. This process should be automated via a computer. A genetic algorithm has been demonstrated to be an excellent optimization algorithm well suited for multivariable problems such as the one presented here. The algorithm has found its uses in the field of antennas and array design, where optimization of multivariable parameters is required. From a mathematical perspective the problems presented in antenna optimization and design are not so different

from those of a TWPD. Both problems are multivariable in nature consisting of parameters and constraints which have a multitude of effects on the overall performance of the device.

Once an accurate model has been demonstrated a genetic algorithm[102] optimization routine could be implemented. The user would input the desired physical parameters as well as constraints such as doping concentrations, contact resistances, physical size constraints, impedance requirements, optical loss, microwave loss, required bias voltage etc. and after several successive generations a optimized design would be presented to the user.

References

1. T.C. Cannon, D. L. Pope, and D. D. Sell, IEEE Transactions, Communication. COM-26, 1045 (1978).

2. J. I. Yamada, S. Machida, and T. Kimura, Electron Letters 15, 106 (1979).

3. T. Miya, Y. Terunuma, T. Hosaka, and T. Miyashita, Electron Letters 15, 106 (1979).

4. S. Fujita, M. Kitamura, T. Torkai, N. Henmi, H. Yamada, T. Suzuki, I. Takano, and M. Shikada, Electron Letters 25, 702 (1989).

5. J. Bowers, K. Giboney, Yih-Guei Wey and Mark Rodwell, "New Concepts in 100 GHz High Efficiency Photodetectors" Invited Paper, University of California, Santa Barbara.

6. M. Alles, U. Auer, F-j. Tegude, and D. Jager, "Distributed Velocity Matched 1.55 μm InP Travelling-Wave Photodetector for Generation of High Millimeterwave Signal Power", Proc. of IEEE Int. Microwave Symp. (MTT-S), June 1998, Baltimore, USA pp. 1233-1236

7. K. S. Giboney, M. J. Rodwell and J. E. Bowers, "Traveling-Wave Photodetector Design and Measurements", IEEE Journal of Selected Topics in Quantum Electronics, Vol. 2, No. 3, September 1996.

8. M. Alles, U. Auer, F. J. Tegude, D. Jager, "Millimeterwave Photodetectors", Proc. of Conference on Microwave and Optoelectronics, April, 22.-24., 1997 Sindelfingen, Germany (invited).

9. M. Alles, U. Auer,F.-J. Tegude. D. Jager, "High-Speed Travelling-Wave Photodetectors for Optical Generation of Millimeterwaves", Proc. of 1997 Asia Pacific Microwave Conference, Hong Kong, 02.10.-05.10.97, Vol.II of III, pp 573-576.

10. A. Umback, W. Passenberg, G. Unterborsch, G. G. Mekkonen, W. Schlaak, C. Schramm, W. Ebert, P. Wolfram, H-G. Bach, S. van Waasen, R. M. Bertenburg, G. Janben, R. Reuter, U. Auer, F. J. Tegude. "27 GHz Bandwidth Integrated Photoreceiver Comprising a Waveguide Fed Photodiode and a GaInAs/AlInAs-HEMT based Travelling Wave Amplifier", Proc. of 54th Device Research Conference (DRC), 24.-26. June 1996, Santa Barabara, USA, pp. 200-201.

11. J. E. Bowers and C. A. Burrus Jr. "Ultrawide-Band Long Wavelength p-i-n Photodetectors" Journal of Lightwave Technology, Volume 5. no. 10, pp1339-1350, October 1987

12. D. L Crawford, R. L. Nagarajan, and J. E. Bowers. "Comparison of Bulk and Quantum wire Photodetectors," Applied Physics Letters, volume 58. no. 15, pp1626-1631.

13. A. Chin and T. Y. Chang, "Enhancement of Quantum Efficiency in Thin Photodiode Through Absorptive Resonance." Journal of Lightwave Technology., volume 9. no. 3 pp321-328. March 1991

14. K. Kishino, M. S Unlu, J. Chiy, J. Reed, L. Arsenault, and H. Morkoc. "Resonant Cavity Enhanced (RCE) Photodetectors "IEEE Journal of Quantum Electrons. volume 27. no. 8 pp. 2025-2034.

15. C. C. Barron, C. J. Mahon, B. J. Thibeault, G. Wang, W. Jiang, L. A. Coldren, and J. E. Bowers, "Resonant-Cavity Enhanced p-i-n Photodetector with 17 GHz Bandwidth-Efficiency Product." Electron Letter., volume 30, no. 21. pp. 1796-1797. October, 1994.

16. K. Litvin, J. Burm, D. Woodard, W. Schaff, and L. F. Eastman, "High Speed Optical Detectors for Monolithic Millimeter Wave Integrated Circuits", in 1993 IEEE MTT-S Microwave Symposium Digest, pp. 1063-1066, June 14-18, 1993.

17. G. P. Agrawal and S. Radic, "Phase Shifted Fiber Bragg Gratings and their Applications for Wavelength Demultiplexing." IEEE Photonic Technology Letter volume 6, no. 8 pp. 995-997. August 1994.

18. A. Alping, "Waveguide pin Photodetectors: Theoretical Analysis and Design Criteria." IEEE Proceeding J. volume 136. no.3, pp. 177-182, June 1989.

19. F. K. Reinhart, "Electroabsorption in $Al_yGa_{1-y}AsAl_xGa_{1-x}As$ Double Heterostructures." Applied Physics Letters., volume 22, no. 8. pp. 372-374. April 1973.

20. J. L. Merz and R. A. Logan, "Integrated GaAs Alx Ga1-xAs Injection Lasers and Detectors with Etched Reflectors." Applied Physics Letters, volume 30. no. 10. pp. 530-533.

21. A. Alping and S. T Eng, "Deteection at Gbit/s Rates with a TJS GaAlAs Laser.", Optical Communications. volume 44, no. 6, pp 381-383. February 1983.

22. J. E. Bowers and C. A. Burras, "High-Speed Zero Bias Waveguide Photodetectors." Electron Letters, volume 22., no. 17, pp. 905-906, August 1986.

23. D. Wake, T. P. Spooner, S.D. Perrin and J. D. Henning, "50 GHz InGaAs Edge-Coupled pin Photodetector.", Electron Letter, vol. 27, no. 12. pp. 1073-1075, June 6, 1991.

24. K. Kato. A Kozen, Y. Muramoto, Y. Itala. T. Nagatsuma and M. Yaita, "110 GHz, 50% Efficiency Mushroom Mesa Waveguide p-i-n Photodiode for a 1.55 μm Wavelength." IEEE Photon Technology Letter., volume 6, no. 6 719-721. June 1994.

25. D. Wake, "Monolithic Integration of Optical Waveguide Circuitry with III-V Photodetectors for Advanced Lightwave Receivers." Journal of Lightwave Technology, vol. 11, no. 8, pp. 1296-1313, August 1993.

26. K. S. Gibboney, M. J.W. Rodwell, and J. E Bowers, "Traveling-Wave Photodetectors", IEEE Photon Technology Letters., vol. 4. no. 12. pp. 1363-1365. December 1992.

27. H. F. Taylor, O. Eknoyan, C. S. Park, K. N. Choi, and K. Change. "Traveling Wave Photodetectors." Proc. SPIE. The International Society for Optical Engineering. vol. 1217. pp.59-63, 1990.

28. K. S. Giboney, M. J. Rodwell, and J. E. Bowers, "Traveling-Wave Photodetector Theory.", IEEE Trans. on Microwave Theory and Techniques, August 1997, pp. 1310.

29. M. Alles, Th. Braasch, and D. Jager, "High-speed Coplanar Schottky Traveling-Wave Photodetector.", Fachgebiet Optoelektronik, Gerhard-Mercator-Universitat Duisburg.

30. D. Jager, R. Kremer, and A. Stohr, "Traveling-Wave Optoelectronic Devices for Microwave Applications.", Fachgebiet Optoelektronik, Gerhard-Mercator-Universitat Duisburg.

31. D. Jager, R. Kremer, and A. Stohr, "High-Speed Travelling Wave Photodetectors, Modulators and Switches.", Fachgebiet Optoelektronik, Gerhard-Mercator-Universitat Duisburg.

32. V. M. Hietala, G. A. Vawter, T. M. Brennan ad B. E. Hammons, "Traveling-Wave Photodetectors for High Power, Large-Bandwidth Applications.", IEEE Transaction on Microwave Theory and Techniques, vol. 43, no. 9, September 1995, pp. 2291.

33. L. Y. Lin, M. C. Wu, T. Itoh, T. A. Vang, r. E. Muller, D. L. Sivco, and A. Y. Cho, "Velocity-matched distributed photodetectors with high-saturation power and large bandwidth" IEEE Photon. Technol. Letter., vol. 8, no. 10, p.1376-1378, 1996.

34. H. Guckel, P. A. Brenna, and I. Palocz, "A parallel-plate waveguide approach to microminiaturized, planar transmission lines for integrated circuits" IEEE Trans. Microwave Theory Tech. vol. MTT-15, pp. 468-476., August 1967.

35. H. Hasegaa, M. Furukawa, and H. Yanai, "Properties of microstrip line on Si-SiO_2 system" IEEE Trans. Microwave Theory Tech., vol. MTT-19, pp. 869-881.

36. D. Jager, "Slow-wave propagation along variable Schottky-contact microstrip line" IEEE Transaction Microwave Theory Tech. vol. MTT-24, pp. 566-573. September 1976.

37. Y. Fukuoka and T. Itoh, "Analysis of slow-wave phenomena in coplanar waveguide on a semiconductor substrate," Electron. Letter. vol. 18, no. 14, pp. 598-590, July 1982.

38. Y. Fukuoka, Y. C Shih, and T. Itoh, "Analysis of slow-wave coplanar waveguide for monolithic integrated circuits," IEEE Trans. Microwave Theory Tech., vol. MTT-31, pp. 567-573, July 1983.

39. R. Sorrentino, G. Leuzzi, and A. Silbermann, "Characteristic of metal-insulator-semiconductor coplanar waveguide for monolithic microwave circuits", IEEE Trans. Microwave Theory and Tech. vol. MTT-32, PP. 410-416. April 1984.

40. C. K. Tzuang and T. Itoh, "Finite-element analysis of slow wave Schottky contact printed lines" IEEE Trans. Microwave Theory and Tech. vol. MTT-34, pp.1483-1489, Dec. 1986.

41. T. G. Livernois and P. B. Katechi, "A generalized method for derving the space-domain Green's function in a shielded, multilayer substrate structure with application to MIS slow wave transmission lines, "IEEE Trans. Microwave Theory Tech. vol. 37, pp. 1761-1767.

42. J. C. Liou and K. M. Lau, "A solution to characteristic of planar transmission lines made of finite thickness metal on multi-layer media".in 1990 IEEE MTT-S Microwave Symp. Digest. May 8-10, 1990, pp. 179-182.

43. K. Wu and R. Vahdieck, "Hybrid-mode analysis of homogeneously and inhomogeneously doped low-loss and slow-wave coplanar transmission lines," IEEE Trans. Microwave Theory Tech. vol. 39, pp. 1348-1360. August 1991.

44. J. P. K. Gilb and C. A. Balanis, "MIS slow-wave structures over a wide range of parameters," IEEE Trans. Microwave Theory Tech. vol. 40. pp. 2148-2154, December 1992.

45. J. C. Liou and K. M. Lau, "Analysis of slow-wave Transmission line on multi-layer semiconductor structures including conductor loss," IEEE Trans. Microwave Theory Tech. vol. 41, pp. 824-829, May 1993.

46. C. Seguinot, P. Kennis, P. Pribetich, and J. F. Legier, "Analytical model of the Schottky contact coplanar line," in Proc. 14th European Microwave Conf. Sept, 1984. pp. 160-165.

47. Y. R. Kwon, V. M. Hietala, and K. S. Champlin, "Quasi-TEM analysis of slow-wave mode propagation on coplanar microstructure MIS transmission line," IEEE Trans. Microwave Theory Tech. vol. MTT-35, pp. 545-551. June 1987.

48. V. M. Hietala, "A study of MIS coplanar slow-wave transmission lines on Silicon," PhD dissertation, Dept. Elect. Eng. Univ. Minnesota, Minneapolis, MN. August. 1988.

49. V. M. Hietala and K. S. Champlin, "Measurement of the microwave properties of micron-size coplanar transmission lines," J. Electromagnetic Waves and Applicat. vol. 5, no. 4/5, pp. 439-452, 1991

50. E. Tuncer and D. P. Neikirk, "High accurate quasistatic modeling of microstrip lines over lossy substrates," IEEE Microwave Guided Wave Lett., vol.2 pp. 409-411, October 1992.

51. D. M. Pozar, "Microwave Engineering", New York Addison-Wesley Publishing Company 1990

52. O. A. Liskovets, "The method of lines", Review, Differential'nye Uravneniya, vol. 1, no. 12 pp. 1662-1678, 1965.

53. B. P. Demidowitsch, et al., "Numerical Methods of Analysis", chp. 5, VEB Wisenschaften, Berlin, 1968.

54. U. Schulz, and R. Pregla, "A New Technique for the Analysis of the Dispersion Characteristics of Planar Waveguides", Archiv Electron, Ubertragungstech. (AEU), 1980, pp. 169-173.

55. R. Pregla and W. Pascher, "The Method of Lines", in T. Itoh (editor), Numerical Techniques for Microwave and Millimeter Wave Passive Structures, pp. 381-446, J. Wiley Publ., New York 1989.

56. S. B. Worm, "Full-wave analysis of discontinuities in planar waveguides by the method of lines using a source approach", IEEE Trans. Microwave Theory and Tech., vol. 38, pp. 1510-1514, 1990.

57. H. Diestel and S. B. Worm, "Analysis of Hybrid Field Problem by the Method of Lines with Nonequidistant Discretization", IEEE Trans. Microwave Theory Tech. vol. 24, no. 6, June 1984, pp. 633-638.

58. F. J. Schmuckle and R. Pregla, "The Method of Lines for the analysis of Planar Waveguides with Finite Metallization Thickness", IEEE Trans. Microwave Theory Tech. vol. 39, Jan. 1991, pp.107-111.

59. F. J. Schmuckle and R. Pregla, "The Method of Lines for the Analysis of Lossy Planar Waveguides", IEEE Trans. Microwave Theory Tech., vol. 38, Oct. 1990, pp. 1473-1479.

60. R. Pregla, M. Koch, and W. Pascher,"Analysis of hybrid waveguide structures consisting of microstrip and dielectric waveguides", Proc. 17th Eur. Microwave Conf., 1987, pp. 927-932.

61. U. Rogge and R. Pregla, "Method of line for the analysis of strip-loaded optical waveguides", J. Opt. Soc. Am. B., vol. 8, no.2, February, 1991, pp. 459-463.

62. U. Rogge and R. Pregla, "Method of lines for the analysis of dielectric waveguides", Journal of Lightwave Technology, vol. 11, no. 12, December 1993, pp. 2015-2020.

63. Pascher, W. and Pregla, R., "Vectorial Analysis of Bends in Optical Strip Waveguides by the Method of Lines", Radio Science, vol. 28, no. 6, 1993, pp. 1229-1233.

64. W. Pascher and R. Pregla, "Analysis of curved optical waveguides by the vectorial method of lines", proc. Int. Conf. Integrated Optics Optical Fibre Commun., pp. 237-240, Paris 1991.

65. R. Pregla, "Analysis of Planar Microwave Structures on Magnetized Ferrite Substrate", Archiv Electron. Ubertragungstech. (AEU), vol. 40, no.5, 1986, pp. 260-274.

66. B. M. Sherril and N. G. Alexopoulos, "The method of lines applied to finline/strip configuration on the anisotropic substrate", IEEE Trans. Microwave Theory Tech., vol. MTT-35, pp. 568-575.

67. R. Pregla, "Method of Lines for the Analysis of Multilayer Gyrotropic Waveguide Structures", IEEE Proc.-H, vol. 140., no.3, June 1993, pp. 183-192

68. R. Pregla and W. Pascher, "Analysis of Rectangular Waveguide Junction by the Method of Lines", Proc. 20th Eur. Microwave Conf., 1990, Budapest, Hungary, pp. 1334-1339.

69. Yangsheng Xu, "Application of the method of lines to solve problems in cylindrical coordinates", Microwave and Optical Technology Letters, vol.1, no. 5, July 1988, pp. 173-175.

70. R. Pregla, "General Formulae for the Method of Lines in Cylindrical Coordinates", IEEE Trans. Microwave Theory Tech., vol. 43, July 1995.

71. R. Pregla, "The Method of Lines for the Analysis of Discontinuities in Cylindrical Waveguides", Proc. of the 6th International IGTE Symposium on Numerical Field Calculation in Electrical Engineering, September 26-28, 1994 Graz, Austria, pp. 174-179.

72. R. Pregla, E. Ahler, "New vector BPM in cylindrical coordinates based on the Method of Liens", Integrated Photonics Research, OSA 1995 Technicl Digest, Febr. 1995, Dana Point, California.

73. R. Pregla and E. Ahler, "Method of Lines for analysis of arbitrarily curved waveguide bends", Electronics letters, vol. 30, no. 18, pp. 1478-1479.

74. E. Ahler and R. Pregla, "Modelling of Y-branches with the MoL-BPM", Conference on Linear and Nonlinear Integrated Optics, Lindau, April 1994, SPIE vol. 2212, pp. 259-267.

75. R. Pregla, J. Gerdes, E. Ahler, S. Helfert, "MoL-BPM Algorithms for Waveguide Bends and Vectorial Fields", Integrated Photonics Research, 1992 Technical Digest, April 13-16, 1992, vol. 10, new Orleans, Louisiana.

76. J. Gerdes, S. Helfert and R. Pregla, "Three Dimensional Vectorial eigenmode Algorithm for Nonparaxial Propagation in reflecting Optical Waveguide Structures", Electronics Letters, vol. 31, no. 1, 1995.

77. R. Pregla and L. Vietzorreck, "Calculation of input impedances of planar antennas with the Method of Lines", Proc. PIERS 1994, July 1994, Noodwijk, The Netherlands.

78. R. Pregla, "New approach for the analysis of cylindrical antennas by the method of lines", Electronics Letters, vol. 30, no. 8, April 1994, pp. 614-615.

79. A. Dreher and R. Pregla. "Analysis of Planar Waveguides with the Method of Lines and Absorbing Boundary Conditions", IEEE Microw. Guid. Wave Lett., vol.1 , pp. 138-140, 1991.

80. A Dreher and R. Pregla. "Analysis of microstrip structures with an inhomogeneous dielectric layer in a unbounded region". Electronics letters, vol. 28, no. 23, pp. 2133-2134, 1992.

81. A. Dreher and R. Pregla. "Full-wave analysis of radiating planar resonators with the method of lines", IEEE Trans. Microwave Theory Tech., vol.41, pp. 1363-1368, 1993.

82. R. Pregla and D. Kremer. "Method of Lines with Special Absorbing Boundary Conditions-Analysis of weakly guiding Optical Structures", IEEE Microwave. Guid. Wave Let. vol. 2(6), pp. 239-241, 1992.

83. P. Berini, K. Wu, "Modeling Lossy Anisotropic Dielectric Waveguides with the Method of Lines", IEEE Trans. Microwave. Theory Tech. vol. 44, no. 5, May 1996 pp. 749-759.

84. P. Berini, "Numerical Methods in Electromagnetic engineering", ELG5379 course notes, University of Ottawa, 1998.

85. P. Berini and K. Wu, "Modeling Dielectric Waveguiding Structures with the Method of Lines", Symp. on Antenna Technology and Applied Electromagnetics – ANTEM, August 9-12, 1998

86. Lusse, P., Stuwe, P., Schule, J., Unger, H.-G. "Analysis of Vectorial Mode Fields in Optical Waveguides by New Finite Difference Method". IEEE/OSA Journ. Lightwave Tech., vol.12, no. 3, pp. 487-494., March 1994

87. Rozzi, T., Cerri, G., Husain, M. N. Zappelli, L. "Variational Analysis of the Dielectric Rib Waveguide Using the Concept of "Transmission Function" and Including Edge Singularities". IEEE Trans. Microwave Theory Tech., vol. 39, no. 2, pp. 247-257, February 1991.

88. U. Rogge and R. Pregla, "Method of lines for the analysis of strip-loaded optical waveguides", Optical Society of America, vol.8, no. 2, February 1991.

89. P. Berini, "P. Berini. "Multi-wavelength Characterization of a Traveling Wave Photodetector Including Electrode Effects.", SPIE ICAP Volum 3491. pp. 860-861.

90. W. H. Press, S. A. Teukolsky, W. T. Vettering, B. P. Flannery, "Numerical Recipes in Fortran Second Edition", Cambridge University Press, New York , 1992.

91. P. B. Bhattacharya, "Semiconductor Optoelectronic Devices", Prentice-Hall, 1997.

92. K. S. Giboney, R. L. Nagarajan, T. E. Reynolds, S. T. Allen, R. P. Mirin, M. J. Rodwell and J. E. Bowers, "Travelling-Wave Photodetectors with 172-GHz Bandwidth and 76 GHz Bandwidth-Efficiency Product", IEEE Photonics Technology Letts, vol. 7, no. 4, April 1995, pp. 412-414.

93. P. Berini, "Some Plasmon-Polariton Modes Supported by a Thin Lossy Metal Film of Finite Width," OSA Optics Letters. Accepted for publication.

94. A. D. Boardman, "Electromagnetic Surface Modes", Wiley, New York, 1982.

95. J. J. Burke, G. I. Stegeman, and T. Tamir, "Surface-polariton-like waves guided by thin, lossy metal films," Physical Review B., vol. 33, no. 8, pp. 5186-5201, April 1986.

96. P. Berini, "Plasmon-polariton waves guided by thin lossy metal films of finite width: Bound modes of symmetric structures.", Physical Review B. vol. 61, no. 15, April 2000.

97. R. Charbonneau, P. Berini, E. Berolo and E. L. Shrzek, "Experimental observation of plasmon-polariton waves supported by a thin metal film of finite width", Optics Letters, vol. 25, no. 11, June 2000.

98. American Institute of Physics Handbook, New-York: McGraw Hill, Section 6g, 3rd Edition, 1972

99. C. Chen, P. Berini, D. Feng, S. Tanev and V. P. Tzolov, "Efficient and Accurate Numerical Analysis of Multilayer Planar Optical Waveguides in Lossy Anisotrpic Media"

100. K. Kato, "Ultrawide-Band/High-Frequency Photodetectors (Invited Paper)", IEEE Trans. on Microwave Theory and Tech, vol. 47, no. 7, pp. 1265- 1281, July 1999.

101. I. Huynen, A. V. Vorst, "A Four-Port scattering Matrix Formalism for p-i-n Traveling-Wave Photodetectors", IEEE Trans. on Microwave Theory and Techniques, vol. 48, no. 6, pp. 1007-1016, June 2000.

102. A. J. Johnson and Y. R. Samii, "Genetic Algorithms in Engineering Electromagnetics", IEEE Antennas and Propagation Magazine, vol. 39, no. 4, pp. 7- 25, August 1997.